DESIGN FOR ADDITIVE MANUFACTURING OF HIGH PERFORMANCE HEAT EXCHANGERS

DESIGN FOR ADDITIVE MANUFACTURING OF HIGH PERFORMANCE HEAT EXCHANGERS

BY

SHEKHAR RAMMOHAN SINGH TANDEL, B.Tech.

A THESIS

SUBMITTED TO THE DEPARTMENT OF MECHANICAL ENGINEERING

AND THE SCHOOL OF GRADUATE STUDIES

OF MCMASTER UNIVERSITY

IN PARTIAL FULFILMENT OF THE REQUIREMENTS

FOR THE DEGREE OF

MASTER OF APPLIED SCIENCE

Master of Applied Science (2022) McMaster University

(Mechanical Engineering) Hamilton, Ontario, Canada

TITLE:	Design for Additive Manufacturing of High Performance Heat Exchangers
AUTHOR:	Shekhar Rammohan Singh Tandel B.Tech. (Mechanical Engineering), PDPM IIITDM, Jabalpur, India
SUPERVISOR:	Dr. M. A. Elbestawi
NUMBER OF PAGES:	xx, 104

Abstract

Heat exchangers are integral parts for thermal management and find countless applications in automotive, aerospace, energy, nuclear power plants, HVAC, etc. Due to intensive research & development and technological advancements in manufacturing technologies, there is an increasing rise in demand for high-performance heat exchangers. In the automotive and aerospace industries, heat exchangers are expected to deliver better thermal efficiency and improve the system's overall functionality in which they are installed by saving space and being lightweight. Additive Manufacturing (AM) is a ground-breaking and promising technology that offers avenues of opportunities to manufacture parts that were almost impossible to be produced with conventional manufacturing and can improve part performance with lightweight and compact designs. Laser-Based Powder Bed Fusion (LPBF), one of the well-known AM techniques, provides freedom to design complex geometries and fabricate them in a layer-by-layer fashion by exposing a high-density laser on a vertically moving powder bed.

The study focuses on the application of AM in re-designing heat exchangers under given design requirements using LPBF. It includes exploring Triply Periodic Minimal Surfaces (TPMS) based structures such as gyroid and realizing them as heat exchanger core. Computational gyroid-based heat exchanger core models were designed and

analyzed for thermal and fluid dynamics characteristics. A parametric study and analysis based on gyroid TPMS network type, periodic length, thickness, aspect ratio, and functional grading were carried out to optimize heat exchanger performance as per design conditions and validate their manufacturability using LPBF. Successful printable designs were further used to develop and manufacture prototypes.

The study concludes with a comparison between additively manufactured gyroid-based design and conventional shell-and-tube design based on the thermal performance from CFD analysis and the weight of prototypes. It was found that the thermal performance from CFD analysis showed an 18.96% improvement, whereas weight was reduced by 14.8% for the gyroid-based design as compared to conventional shell-and-tube design.

To my sister and my parents

I owe you everything

Acknowledgements

First, I would like to thank my supervisor Dr. M. A. Elbestawi who gave me an opportunity to conduct research, provide necessary resources, and supported me in this journey. I am grateful to work under his guidance and mentorship. I would like to thank Dr. Dalia Mahmoud and Dr. Mostafa Yakout who directed and helped me by all possible means. I would like to thank the FCA group in Italy and USA for collaborating and guiding this project.

I would like to show my appreciation to my colleagues (more like friends) in the Additive Manufacturing Group at McMaster University for presentation rehearsals, discussions, and group meetings. Finally, I would like to thank my sister Shikha, my parents, and everyone who supported me throughout my master's program.

Contents

List of Figures

List of Tables

Abbreviations, Definitions, and Notations

Abbreviations

AM	Additive Manufacturing
CAD	Computer-Aided Design
ASTM	American Society for Testing and Materials
DfAM	Design for Additive Manufacturing
HVAC	Heating Ventilation Air-Conditioning
WCAC	Water-Cooled Charge Air Cooler
CAE	Computer-Aided Engineering
CAC	Charge Air Coolers
ACM	Air Conditioning Machines
FCA	Fiat Chrysler Automobile

STL	Stereo-lithography/Standard Tessellation Language/ Standard Triangle Language
LPBF	Laser-Based Powder Bed Fusion
ME	Material Extrusion
MJ	Material Jetting
BJ	Binder Jetting
VP	VAT Photopolymerisation
FFF	Fused Filament Fabrication
FDM	Fused Deposition Modeling
MJM	Multi-Jet Modeling
SCP	Polyjet Smooth Curvatures Printing
DOD	Drop On Demand
3DP	3D Printing
DLP	Digital Light Processing
CLIP	Continuous Liquid Interface Production
3SP	Scan, Spin, and Selectively Photocure
SLA	Stereolithographic Apparatus
SHL	Sheet Lamination

LOM	Laminated Object Manufacturing
UAM	Ultrasonic Additive Manufacturing
DED	Direct Energy Deposition
LENS	Laser Engineered Net Shaping
DMD	Direct Metal Deposition
PBF	Powder Bed Fusion
SLM	Selective Laser Melting
SLS	Selective Laser Sintering
EBM	Electron Beam Melting
LMTD	Log-Mean Temperature Difference
NTU	Number of Transfer Units
TPMS	Triply Periodic Minimal Surfaces
B-Reps	Boundary Representation
CFD	Computational Fluid Dynamics
TEMA	Tubular Exchangers Manufacturers Association
nTop	nTopology
FEA	Finite Elements Analysis
OBJ	Object Files

CHT	Conjugate Heat Transfer
RVE	Representative Volume Element
VED	Volumetric Energy Density

Notations and Definitions

q	Total heat transfer rate (kW)
$\dot{m}_h$	mass flow rate of hot fluid (kg/s)
$\dot{m}_c$	mass flow rate of cold fluid (kg/s)
$I_{h,i}$	Enthalpy of hot fluid at inlet (kJ)
$I_{h,o}$	Enthalpy of hot fluid at outlet (kJ)
$I_{c,i}$	Enthalpy of cold fluid at inlet (kJ)
$I_{c,o}$	Enthalpy of cold fluid at outlet (kJ)
$c_{p,h}$	Specific heat at constant pressure for hot fluid (kJ/(kg.K))
$c_{p,c}$	Specific heat at constant pressure for cold fluid (kJ/(kg.K))
T_h	Temperature of hot fluid (K or °C)
T_c	Temperature of cold fluid (K or °C)
$T_{h,i}$	Temperature of hot fluid at inlet (K or °C)
$T_{h,o}$	Temperature of hot fluid at outlet (K or °C)

$T_{c,i}$	Temperature of cold fluid at inlet (K or °C)
$T_{c,o}$	Temperature of cold fluid at outlet (K or °C)
ΔT	Temperature difference (K or °C)
U	Overall Heat Transfer Coefficient (W/m^2.K or W/m^2 .°C)
A	Surface area of heat exchanger (m^2)
R_t	Total thermal resistance (K/W or °C/W)
$R_{h,conv.}$	Thermal resistance of hot fluid due to convection (K/W or °C/W)
$R_{cond.}$	Thermal resistance of solid wall due to conduction (K/W or °C/W)
$R_{c,conv.}$	Thermal resistance of cold fluid due to convection (K/W or °C/W)
UA	Overall conductance (W/K or W/°C)
h_h	Convective heat transfer coefficient of hot fluid (W/m^2.K)
h_c	Convective heat transfer coefficient of cold fluid (W/m^2.K)
A_h	Surface area of hot fluid (m^2)
A_s	Surface area of the heat exchanger wall (m^2)
A_c	Surface area of cold fluid (m^2)
λ	Wall thickness of heat exchanger (mm)
k	Thermal conductivity of heat exchanger material (W/(m.K))
ΔT_{lm}	Log Mean Temperature Difference (K or °C)

C_h	Specific heat capacity of hot fluid (kJ/(s.K))
C_c	Specific heat capacity of cold fluid (kJ/(s.K))
C_{min}	Specific heat capacity of fluid with minimum value (kJ/(s.K))
C_{max}	Specific heat capacity of fluid with maximum value (kJ/(s.K))
q_{max}	Maximum heat transfer rate (kW)
ϵ	Effectiveness of the heat exchanger
L	periodic length of TPMS structure (mm)
K	Offset parameter of TPMS structure (mm)
ΔP	Pressure difference (kPa)
P	Laser Power (W)
v	Scanning speed (mm/s)
h	Hatching spacing (mm)
t	Layer thickness (mm)
E	Energy Density (J/mm^3)
w	Stripe width (mm)
δ	Stripe overlap
(a, b, c)	Gyroid perioidic length in (X, Y, Z) directions

Chapter 1

Introduction

Additive manufacturing (AM) is a smart manufacturing process to produce a three-dimensional object directly from its CAD model [1]. In traditional or conventional manufacturing processes, a part is generated by removing material, whereas, in AM, a component is built by adding material layer by layer [2]. AM is also referred to by terms such as 3D printing, desktop manufacturing, free-form manufacturing [3]. The first of its kind was introduced in 1987, which prints photo-sensitive liquid polymers by lasers using a Stereolithography [4] unless a patent for the technology was available after 2006 [5]. In addition, AM is majorly used for rapid prototyping, rapid tools, and rapid manufacturing [6]. There are seven different categories in AM Technologies as per ASTM, namely, material jetting, sheet lamination, binder jetting, vat polymerization, material extrusion, direct energy deposition, and powder bed fusion [1]. AM has vastly developed over a while and found its applications in biomedical [7], aerospace [8], automotive [9], etc. With the advent of recent technological advancements in AM, it has become a necessity in manufacturing and product development [10] and thus, there is a need to generate a new set of design rules,

principles, and workflows, which is Design for Additive Manufacturing (DfAM).

Heat Exchangers play an important role in thermal management. They are extensively used in automobiles, aerospace, chemical processing, food industry, solar energy, nuclear plants, electronic devices, waste-heat recovery systems, HVAC, etc. Therefore, innovative efforts in research and development are directed for designing compact and efficient heat exchangers, which require less volume of material and are lightweight [11]. AM offers freedom in creating such compact and lightweight designs with complex geometries. However, computational design and analysis will be complicated and time-consuming as compared to designs manufactured from conventional (subtractive and formative) manufacturing techniques [3]. Therefore, an established workflow, namely, Design for Additive Manufacturing (DfAM), is required to design, analyze and manufacture a high-performance heat exchanger.

This research aims to introduce an approach of studying present DfAM design principles and research, designing geometries for AM, performing computational analysis, and validating designs by their manufacturability with AM to conclude with the most feasible and optimized design. It is done with a case study of designing a Water-Cooled Charge Air Cooler (WCAC) for AM with given design conditions.

1.1 Scope of research

Design for Additive Manufacturing (DfAM) is derived from Design for Manufacturing (DFM), which is defined as designing a part that can be easily manufactured [12]. DfAM includes principles of Additive Manufacturing (AM), Computer-Aided Design (CAD), and Computer-Aided Engineering (CAE) [3]. Due to a range of materials, with their mechanical properties that can now be manufactured with a high level of

precision, AM has the potential to integrate engineering designs and/or prototypes into a final fully functional product [13]. However, it is important to consider manufacturability constraints in AM processes, such as overhangs, features such as thin walls, small holes and slots, and enclosed void spaces preventing removal of support structures and unmelted powder [14]. In addition, limitations in AM processes such as anisotropy in material properties, thermal distortion, and cost and time are also to be considered. Moreover, different AM processes have different types of manufacturing constraints [14]. Therefore, realizing the capabilities and limitations of AM before designing parts feasible for AM manufacturing, a workflow for integration of AM, CAD, and CAE can be created, enabling manufacturability and cost-effectiveness for DfAM.

In this research study, the focus is only on the design and validation and does not include,

- Structural and surface roughness analysis
- Manufacturing final part

Highlights of this research will include

- Exploring lattice structure designs such as cellular lattices
- Studying triply periodic minimal surfaces such as gyroid
- Evaluating the thermal performance of heat exchanger design through Computational Fluid Dynamics (CFD) analysis using Conjugate Heat Transfer (CHT) method
- Evaluating feasibility for AM manufacturability

1.2 Water-cooled charge air cooler

Heat exchangers used for thermal management in automotive are generally [15]

- Radiators
- Air Conditioning Machines (ACM)
- Heat Cores
- Oil Coolers
- Charge Air Coolers (CAC)/ Intercoolers

For improving the internal combustion and power output of the engine, a turbocharger is installed consisting of two main components, i.e., turbine and compressor [15]. The turbine drives compressor for intake of air from ambient. The compressor compresses air to increase its density and pressure, which also increases its temperature. This hot air needs to be cooled down to avoid knocking in the engine. Therefore charge air coolers or intercoolers are used to decrease the temperature of charge air while minimizing drop in density and pressure and maximizing the power output of the engine [15].

Intercoolers are divided into three types: air-to-air, liquid-to-air, and one-shot intercooler [16]. The water-to-air intercooler or water-cooled charge air cooler forms the liquid-to-air intercooler with water as a coolant, which exchanges heat and lowers the temperature of charge air. Due to short piping length, the charge air volume and the air pressure loss are reduced, giving an advantage over other charge air coolers. Moreover, condensation in the charge air cooler is prevented by controlling the temperature of the coolant, which will also maintain the temperature of charge air [17]. Thus, a space-saving and lightweight water-cooled charger air cooler can be

designed with high cooling performance, reliability, and a high-temperature working environment.

As mentioned above, this research aims to design a high-performance heat exchanger using metal additive manufacturing, and to do so, a case study of designing a water-cooled charge air cooler will be done. Therefore, the data below in the Table 1.1 and the Table 1.2 are the boundary conditions and target performance required respectively for designing a water-cooled charger air cooler with design space of 170 mm x 100 mm x 90 mm provided by Fiat Chrysler Automobile (FCA).

Table 1.1: Data for design (provided by FCA)

Boundary conditions	
Charge air inlet temperature	160 °C
Charge air inlet pressure	275 kPa
Charge air mass flow rate	235 g/s
Coolant inlet temperature	40 °C
Coolant inlet pressure	60 kPa
Coolant volumetric flow rate	25 L/min
Ambient air temperature	25 °C

Table 1.2: Data for target performance (provided by FCA)

Target performance required	
Charge air pressure drop	3 kPa
Coolant pressure drop	15 kPa
Charge air outlet temperature	42 °C
Maximum heat rejection	$\geq$28 kW

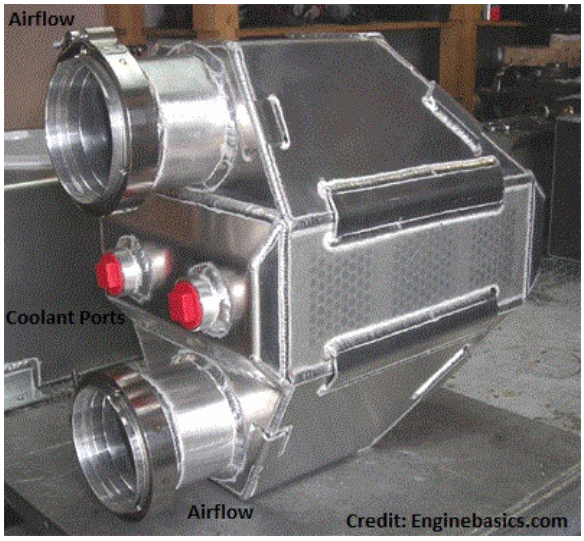

(a) Typical liquid-to-air intercooler (image courtsey: enginebasics.com) [18]

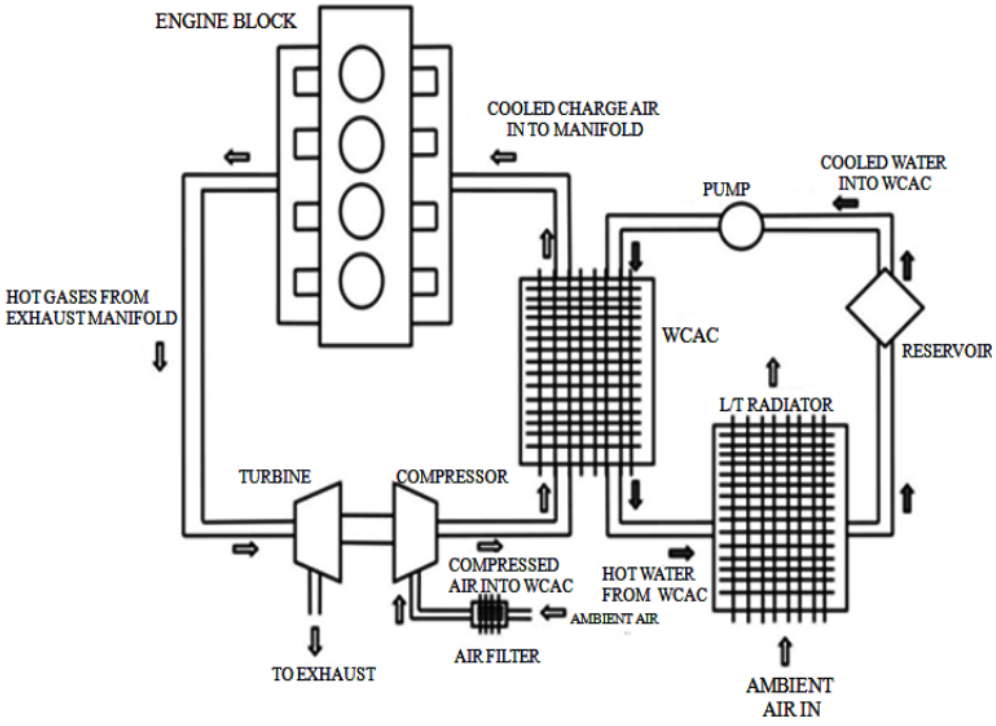

(b) water-to-air intercooler circuit [15]

Figure 1.1: Typical liquid-to-air intercooler and water-to-air intercooler circuit

1.3 Structure of thesis

The structure of this thesis is divided into five chapters. Chapter 1 briefly introduces the scope of research regarding the water-cooled charger air cooler, design conditions, and required target performance provided by FCA. Literature review on Additive Manufacturing (metal-based AM processes), Design for AM, lattice structures and triply periodic minimal surfaces, heat exchangers designs and computational analysis methods, and existing studies on additive manufacturing of heat exchangers is discussed in chapter 2. The approach used in the study is explained in chapter 3. Chapter 4 includes thermal performance results and AM manufacturability of potential heat exchanger designs. Finally, the conclusion and future work of the research are discussed in chapter 5.

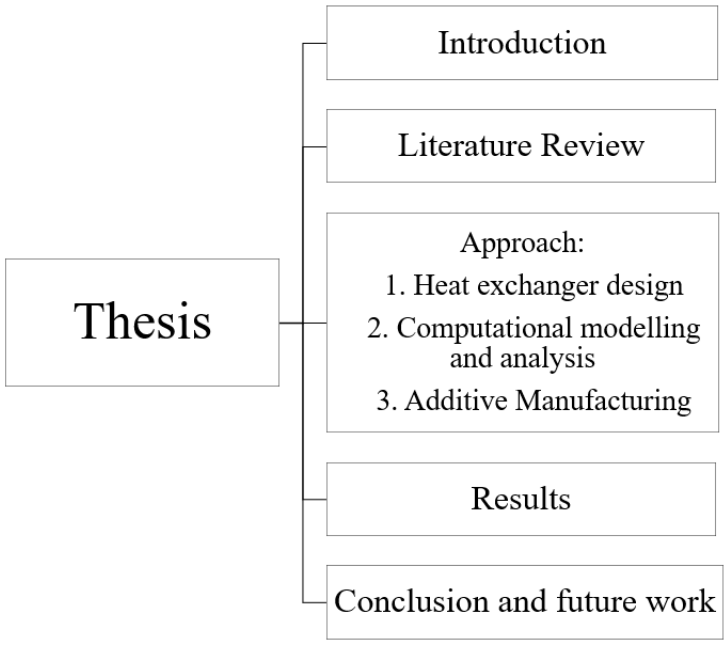

Figure 1.2: Structure of thesis

Chapter 2

Literature Review

2.1 Additive Manufacturing

As per the ASTM F2792 10e1, the standard terminology of AM in the additive manufacturing technologies document is given as [19]

"The process of joining materials to make objects from 3D model data, usually layer upon layer, as opposed to subtractive manufacturing methodologies, such as traditional machining."

The most usual way of manufacturing a part using AM is to design an enclosed watertight geometry in CAD software, convert it in STL (Stereo-lithography, standard triangle language, or standard tessellation language) file format, slice in machine supported software, and finally export it in a machine for building [20]. Although AM is an expensive process, there are many advantages such as complexity in part, setting up assemblies instantly, consolidating parts, customizing for mass production, freedom in design, light-weighting, and manufacturing on-demand, can add value to the part as well as make a business profitable by life cycle cost reduction and higher pricing [19]. Different AM technologies are used depending on the starting state of the

material, type of material, application, etc. Metal AM systems are further categorized based on the source of energy, feedstock material, the volume of build, etc. They are classified into three broader categories, i.e., powder feed, powder bed, and wire feed systems [21]. Laser-Based Powder Bed Fusion (LPBF) is one of the most commonly used powder bed systems for industrial utilization in different applications.

2.1.1 Additive Manufacturing Processes and Technologies

A brief but overall understanding of the main AM processes and technologies used today are described as below [19]:

1. **Material Extrusion (ME)**

   In the ME process, filament made of thermoplastic material is pushed through the hot nozzle, gets melted, and deposits over build platform [22]. Fused filament fabrication (FFF) and fused deposition modeling (FDM) are the two standard AM technologies based on material extrusion [23]. Although ME is one of the cheapest AM processes with a wide range of materials available, parts manufactured from it have high surface roughness, low geometrical accuracy, anisotropy, and generally require support [24].

2. **Material Jetting (MJ)**

   Ultraviolet light cures thermoset resins of photopolymer in tiny droplets in the MJ process [22]. Printing technologies commonly using MJ principles are Multi-Jet Modeling (MJM), Polyjet Smooth Curvatures Printing (SCP), and Drop On Demand (DOD) [23]. Accuracy and multi parts printing are the characteristics

of the MJ technique, and materials commonly printed are composites, thermoplastic polymers, and photopolymers [20].

3. **Binder Jetting (BJ)**

   A part is formed layer after layer on a powder bed by depositing binding agents in the BJ process [22]. Well-known 3D Printing (3DP) comes under the category of BJ [19]. Materials such as metals, glass, ceramics, and plastics are printed using the BJ process. In the BJ process, powders used can be harmful as well as have requirements of post-processing, but it can be highly productive and has a wide range of materials for printing [23] [25].

4. **VAT Photopolymerisation (VP)**

   Resins made from polymer are cured by a light source (typically laser) in the VP AM technique [22]. Commonly used AM technologies working on the principle of VP are Digital Light Processing (DLP), Continuous Liquid Interface Production (CLIP), Scan, Spin, and Selectively Photocure (3SP), and Stereolithographic Apparatus (SLA) [19]. The advantages of this process are high complexity, good accuracy, and a smooth surface finish. In contrast, the process is used only for resins, needs expensive equipment, and creeping is observed after the curing process [23].

5. **Sheet Lamination (SHL)**

   Cut shapes in the form of slices of the 3D model are bonded together in the SHL technique [19]. Two processes, namely, Laminated Object Manufacturing (LOM) and Ultrasonic Additive Manufacturing (UAM), use SHL technology. In LOM, either paper or polymer films are bonded together using adhesives,

whereas ultrasonic welding is used to bound sheets of metal together in UAM. Different materials, including metals such as copper, titanium, aluminum, and stainless steel with relatively little energy input, can be bonded using SHL, but post-processing can be tedious and expensive [19].

6. **Direct Energy Deposition (DED)**

   In the DED process, material in the form of either powder or wire gets deposited through a nozzle on a given surface, melts, and solidifies due to a high energy beam [19]. Technologies such as Laser Engineered Net Shaping (LENS), Direct Metal Deposition (DMD), and Laser Cladding use the DED process. Fast processing and movement of the nozzle in multiple directions are the characteristics of DED. Disadvantages of DED include low accuracy, poor surface finish, and requirement of machining in post-processing [19].

7. **Powder Bed Fusion (PBF)**

   A layer of building material, in the form of powder, is spread across a build platform, and either a laser or an electron beam melts powder by scanning slices of component, is done in the PBF process [19]. Selective Laser Melting, Laser Sintering (SLM/LS), and Electron Beam Melting (EBM) are examples of technologies using the PBF process. A highly dense part is produced with relatively isotropic behavior in all directions. It can print a wide range of polymers as well as metals. Components from metals such as titanium, maraging steel, cobalt chrome, stainless steel, aluminum, and its alloys, and more with good surface finish and high strength are manufactured. It is one of the cheapest production

technologies considering the material point of view. Addition of support structures for heat transfer and removal of them during post-processing account for drawbacks in PBF [19].

2.1.2 Laser-Based Powder Bed Fusion (LPBF

The LPBF technology provides a high degree of freedom in creating unique and complex geometries and internal structures with the ability of topology optimization [26]. Moreover, user-specified gradient structures in the form of design and spatially varying material composition are done with LPBF. Due to such advantages, there has been steep growth in this technology as well as it has opened doors for application in various industries in recent times [27]. Figure 2.1 shows a schematic diagram of the PBF-LB machine, the laser-material interaction, and a flow chart describing the workflow from the CAD model to the final part.

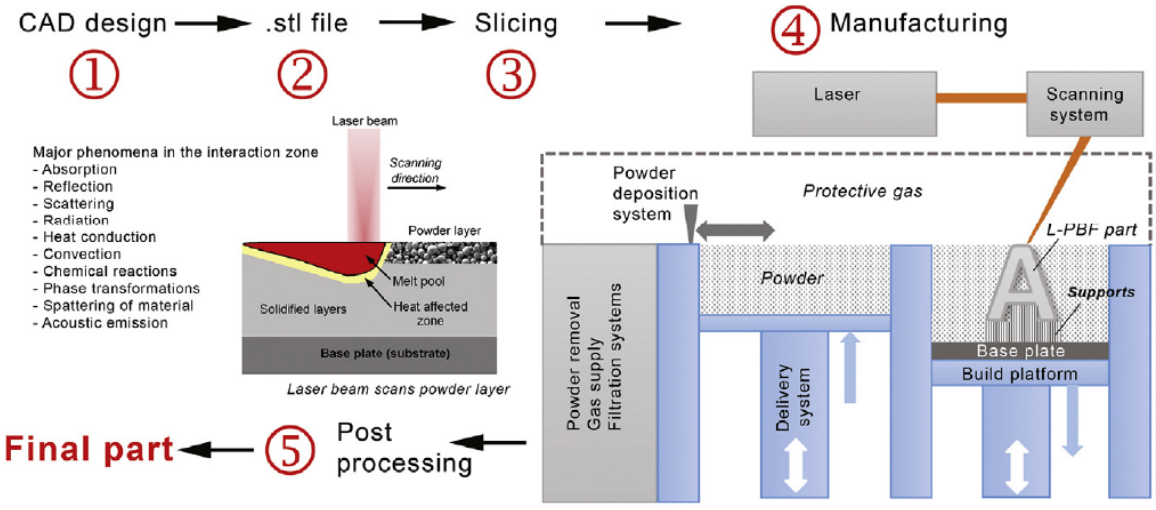

Figure 2.1: A workflow from building part from CAD model, schematic diagram of LPBF machine and laser-material interaction in the LPBF process [26]

There are more than 130 input parameters affecting the LPBF process [28]. Apart from predefined parameters, the ones that have the most impact on the component and its quality are divided into four groups: machine-based, material-based, process-parameters, and post-treatment parameter [26]. Laser power, scanning speed, layer thickness, focal spot diameter, inert gas flow rate, the oxygen level in the surrounding atmosphere, etc., are variable system parameters that can be controlled [29]. It is important to know that the LPBF process is not linear, i.e., changing an input parameter does not linearly change an output value. Also, changing one parameter can lead to changes in several different parameters. Therefore, with the development of some general guidelines, the most optimal process parameters are identified for some materials and systems to enable high-quality output [26].

A single track is formed from the melting and solidification of metal powder, deposited layer-wise on the substrate or the base plate, occurring due to the scanning of a high-energy laser beam [26]. This single track is the basic structural unit of the 3D LPBF object. A group of single tracks forms one layer, and a group of such layers forms the 3D part. To ensure the quality and performance of LPBF parts, it is crucial to choose the correct laser beam scanning direction, scanning path, scanning sequence, etc. Different areas of the component are given different scanning strategies and process parameters. During the LPBF process, the part needs to be fixed on the base plate either directly or with the help of support structures. Support structures are helpful for the prevention of structural deformation and dissipating heat. Part design, orientation on the build plate, support placements, scanning strategy. etc. are vital factors to ensure accuracy, surface quality, and density of the manufactured component [26].

2.2 Heat Exchanger analysis

Heat exchangers are devices that enable heat transfer between fluids at different temperatures. Heat exchangers are classified based on various criteria such as flow arrangement, construction type, etc. [30]. Based on flow arrangement, heat exchangers are divided into parallel-flow, counter-flow, and cross-flow, whereas based on construction, there are two types: recuperators and regenerators [30] [31]. Heat transfer is direct between the fluids in recuperators, but in the case of regenerators, there is no immediate heat transfer because of an additional step involving thermal storage. Recuperators are further distinguished as direct and indirect contact. There is a physical separation in the indirect contact type in the form of a wall between the fluids [31]. For the design and analysis of heat exchangers, it is essential to determine the overall heat transfer coefficient and identify the appropriate heat exchanger design method based on the known conditions.

For a compact heat exchanger with high efficiency, heat transfer should be maximized with minimization of material volume in confined space [32]. Generally, pressure drop increases when heat transfer is enhanced in a single phase [32], and so, higher pumping power is required [33]. Thus, the design objective of heat exchangers is to minimize the ratio of pressure drop to heat transfer [34].

2.2.1 Governing equations

Inlet and outlet temperatures of fluids involved in the heat exchanger, the total surface area required for heat transfer, and the overall heat transfer coefficient are necessary to design and determine the performance of a heat exchanger [30]. Energy balances can be applied to the hot and cold fluid streams to calculate these quantities. The

steady-state flow energy equation, considering q as the heat transfer rate, no heat transfer between the heat exchanger and the surroundings, and no changes in kinetic and potential energies of fluids, equations 2.2.1a and 2.2.1b of energy balances are [30]

$$q = \dot{m}_h(I_{h,i} - I_{h,o}) \tag{2.2.1a}$$

$$q = \dot{m}_c(I_{c,o} - I_{c,i}) \tag{2.2.1b}$$

where I is the fluid enthalpy & $\dot{m}_h$ and $\dot{m}_c$ are mass flow rates of hot and cold fluids respectively. Subscripts *h, c, i*, and *o* represent hot fluid, cold fluid, inlet, and outlet respectively. If specific heats of fluids are assumed constant and there is no phase change, then equations 2.2.1a and 2.2.1b can be written as [30]

$$q = \dot{m}_h c_{p,h}(T_{h,i} - T_{h,o}) \tag{2.2.2a}$$

$$q = \dot{m}_c c_{p,c}(T_{c,o} - T_{c,i}) \tag{2.2.2b}$$

where temperatures $T_{h,i}, T_{h,o}, T_{c,o}$ and $T_{c,i}$ are average temperatures of fluid at designated locations & $c_{p,h}$ and $c_{p,c}$ are specific heats at constant pressure of hot and cold fluids respectively. Above equations are independent of type or flow arrangement in a heat exchanger. Another important expression related to total heat transfer rate q and the temperature difference ΔT between hot and cold fluids is [30]

$$\Delta T = T_h - T_c \tag{2.2.3a}$$

$$q = UA\Delta T_m \tag{2.2.3b}$$

where U and A overall heat transfer coefficient and surface area of the heat exchanger. In a heat exchanger, heat is transferred from hot fluid to the solid wall by convection, through the solid wall by conduction, and finally, from the solid wall to the cold fluid again by convection [31]. There are thermal resistances associated with each mode of heat transfer. These resistances are useful for the determination of overall heat transfer coefficient U. If R_t is the overall thermal resistance, then

$$R_t = \frac{1}{UA} = R_{h,conv.} + R_{cond.} + R_{c,conv.} \tag{2.2.4a}$$

$$UA = \frac{1}{\frac{1}{h_h A_h} + \frac{\lambda}{kA_s} + \frac{1}{h_c A_c}} \tag{2.2.4b}$$

where,

$R_{h,conv.}$ = Thermal resistance of hot fluid due to convection

$R_{cond.}$ = Thermal resistance of solid wall due to conduction

$R_{c,conv.}$ = Thermal resistance of cold fluid due to convection

UA = Overall conductance of the heat exchanger

h_h = Convective heat transfer coefficient of hot fluid

A_h = Surface area of hot fluid

λ = Wall thickness of heat exchanger

k = Thermal conductivity of heat exchanger material

A_s = Surface area of the heat exchanger wall

h_c = Convective heat transfer coefficient of cold fluid

A_c = Surface area of cold fluid

2.2.2 Basic design methods

There are two commonly used methods for heat exchanger analysis based on known conditions and output required and are as below,

1. **The log-mean temperature difference (LMTD) method**

   For heat exchanger design problems where inlet and outlet temperatures and capacities of the hot and cold fluids are known, and the output is the size of the heat exchanger, the LMTD method is used. The heat transfer rate for the heat exchanger is

   $$q = UA\Delta T_{lm} \tag{2.2.5}$$

   where ΔT_{lm} is the log mean temperature difference and is given by

   $$\Delta T_{lm} = \frac{\Delta T_1 - \Delta T_2}{\ln\left(\frac{\Delta T_1}{\Delta T_2}\right)} \tag{2.2.6}$$

   where the endpoint temperatures, ΔT_1 and ΔT_2, for the parallel flow heat exchanger are

   $$\Delta T_1 = T_{h,i} - T_{c,i} \tag{2.2.7a}$$

   $$\Delta T_2 = T_{h,o} - T_{c,o} \tag{2.2.7b}$$

   and for the counter-flow heat exchanger are

   $$\Delta T_1 = T_{h,i} - T_{c,o} \tag{2.2.8a}$$

   $$\Delta T_2 = T_{h,o} - T_{c,i} \tag{2.2.8b}$$

2. **The ϵ-NTU method**

For heat exchanger design problems where size and type are known, and the output is the fluids' outlet temperatures of the heat exchanger, the ϵ-NTU method is used. The capacity rate ratio is

$$C^* = \frac{C_{min}}{C_{max}} \tag{2.2.9}$$

If C_h and C_c are the heat capacity rates of hot and cold fluids respectively, then C_{min} and C_{max} are the minimum and maximum values as per the magnitudes between the two respectively.

Effectiveness of the heat exchanger 'ϵ'

$$\epsilon = \frac{q}{q_{max}} = \frac{\text{Heat transfer rate in actual}}{\text{Maximum heat transfer rate}} \tag{2.2.10}$$

where

$$q_{max} = (\dot{m}c_p)_c(T_{h1} - T_{c1}) \quad \text{if} \quad C_c < C_h \quad \text{or} \tag{2.2.11a}$$

$$q_{max} = (\dot{m}c_p)_h(T_{h1} - T_{c1}) \quad \text{if} \quad C_c < C_h \tag{2.2.11b}$$

where the heat capacity rates for the hot and the cold fluids are $C_c = \dot{m}_c c_{pc}$ and $C_h = \dot{m}_h c_{ph}$ respectively, c_p is specific heat at constant pressure, and $\dot{m}$ is the mass flow rate of the fluids.

Finally, the effectiveness of the heat exchanger can be written as

$$\epsilon = \frac{C_h(T_{h1} - T_{h2})}{C_{min}(T_{h1} - T_{c1})} = \frac{C_c(T_{c2} - T_{c1})}{C_{min}(T_{h1} - T_{c1})} \tag{2.2.12}$$

The ratio of overall thermal conductance to the minimum heat capacity rate is defined as the number of transfer units (NTU). NTU relates to the non-dimensional thermal size or the heat transfer size of the exchanger.

$$\text{NTU} = \frac{UA}{C_{min}} = \frac{1}{C_{min}} \int U \, dA \tag{2.2.13}$$

2.3 Design for Additive Manufacturing

There is a significant knowledge gap between design for conventional manufacturing and design for AM [3]. Thus, considering new design principles and standards for AM, DfAM is important for designers to know a way to alleviate limitations of the technology and improve performance functionality of the final manufactured part [35]. DfAM helps to prepare guidelines, tools, and methodologies that a designer can use, taking unique features of AM into account [13]. AM workflow based on DfAM principles is shown in the figure 2.2. Topology optimization is an integral part of the design phase of DfAM [36]. It is a mathematical approach to finding material requirements in design space for achieving optimized structural performance [37]. A consequence of topology optimization is light-weighting, which can significantly benefit the automotive industry [38] if the goal is to reduce energy consumption. Saving material volumes or replacement with better material, preserving or improving strength, cost-effectiveness, and improving internal cooling are a few of the advantages of light-weighting [39]. When a part is designed, if there is a compromise between strength to weight and stiffness, lightweight structures can be very beneficial [40]. Lattice structures, cellular foams, honeycomb structures, etc., are examples of lightweight

structures that are too complex to manufacture with traditional manufacturing technologies [41]. Hence, the concept of light-weighting and complex structures supports the basic DfAM principle of maximizing functional performance while designing a part within constraints of manufacturing capabilities [42].

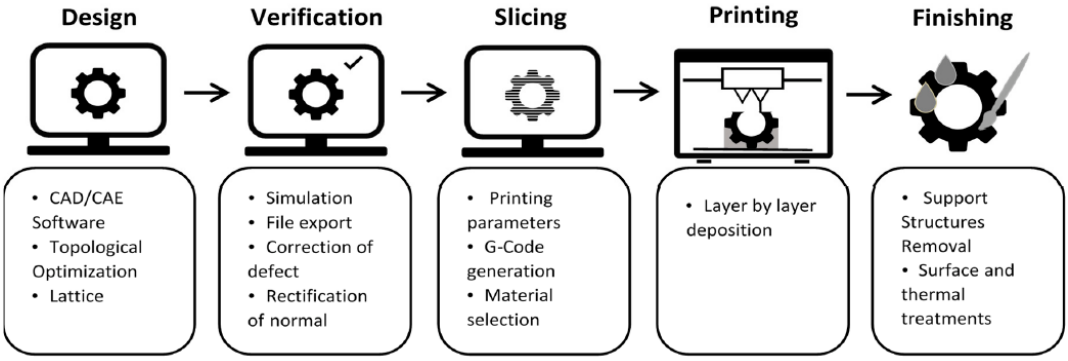

Figure 2.2: AM workflow [35]

2.3.1 Lattice structures

An interconnected network of solids struts, plates, or periodic/random arrangement of small unit cells is cellular solids [43]. A cellular structure consisting of repeated unit cells forming a larger volume is a lattice [19]. Lattice structures have better strength, lightweight, lower relative density, and elasticity as compared to other solid structures [44]. Variation in size of the unit cells in lattice structures can form graded lattice structures which enable designing a component with gradually varying stiffness and custom-made density needed for a particular application [45]. There are three types of lattice structures, strut-based lattice, triply periodic minimal surfaces (TPMS), and shell lattice structures [46]. In a strut-based lattice structure, a series of struts/beams and nodes are confined in a given volume [47]. TPMS is defined

mathematically as surfaces minimizing their area within specified boundaries and of zero mean curvature [48]. Shell lattices are TPMS-like, but the surface does not necessarily have zero mean curvature [3].

2.3.2 Triply Periodic Minimal surfaces (TPMS)

TPMS is a continuous and smooth surface that divides a volume into two congruent regions [49]. Unit cells of minimal surfaces such as Schoen gyroid, Schwartz P, Schwartz diamond, etc., fall under the category of TPMS [3]. These are created from level-set equations and contain implicit trigonometric functions defining an isosurface [50]. Implicit functions of Schwartz, Gyroid, and Diamond surfaces are as follows: [51]

$$\textbf{Schwartz} : \cos\left(\frac{2\pi}{L}x\right) + \cos\left(\frac{2\pi}{L}y\right) + \cos\left(\frac{2\pi}{L}z\right) = K$$

$$\textbf{Gyroid} : \cos\left(\frac{2\pi}{L}x\right)\sin\left(\frac{2\pi}{L}y\right) + \cos\left(\frac{2\pi}{L}y\right)\sin\left(\frac{2\pi}{L}z\right) + \cos\left(\frac{2\pi}{L}z\right)\sin\left(\frac{2\pi}{L}x\right) = K$$

$$\begin{aligned}\textbf{Diamond} : &\sin\left(\frac{2\pi}{L}x\right)\sin\left(\frac{2\pi}{L}y\right)\sin\left(\frac{2\pi}{L}z\right) + \sin\left(\frac{2\pi}{L}x\right)\cos\left(\frac{2\pi}{L}y\right)\cos\left(\frac{2\pi}{L}z\right) \\ &+ \cos\left(\frac{2\pi}{L}x\right)\sin\left(\frac{2\pi}{L}y\right)\cos\left(\frac{2\pi}{L}z\right) + \cos\left(\frac{2\pi}{L}x\right)\cos\left(\frac{2\pi}{L}y\right)\sin\left(\frac{2\pi}{L}z\right) = K\end{aligned}$$

where K = offset parameter and L = periodic length. These three types of TPMSs with unit cell size and zero offsets are shown in Figure 2.3.

2.4 Computational design and analysis

A full 3D representation of a part designed in a computer system is shown in the form of Computer-Aided Design (CAD) [52]. Major CAD systems like SolidWorks,

Siemens NX, Catia, Creo, and others, use boundary representation (B-Reps), which is a group of faces representing boundary [53]. B-Reps store data in the form of vertices, edges, and faces. Operations such as blending, drafting, shelling, extrusion, and others can be done using B-Rep [54], but it is not easy to model very complex designs showing natural or organic designs. Also, there is a substantial computational cost associated while visualizing, animating, or rendering using B-rep [55]. Furthermore, when a model has many features, file size and computational time also increase exponentionally [56]. Thus, a better modeling and analysis method is necessary to represent a complex geometry such as TPMS and perform Computational Fluid Dynamics (CFD) analysis for heat exchangers with TPMS geometry.

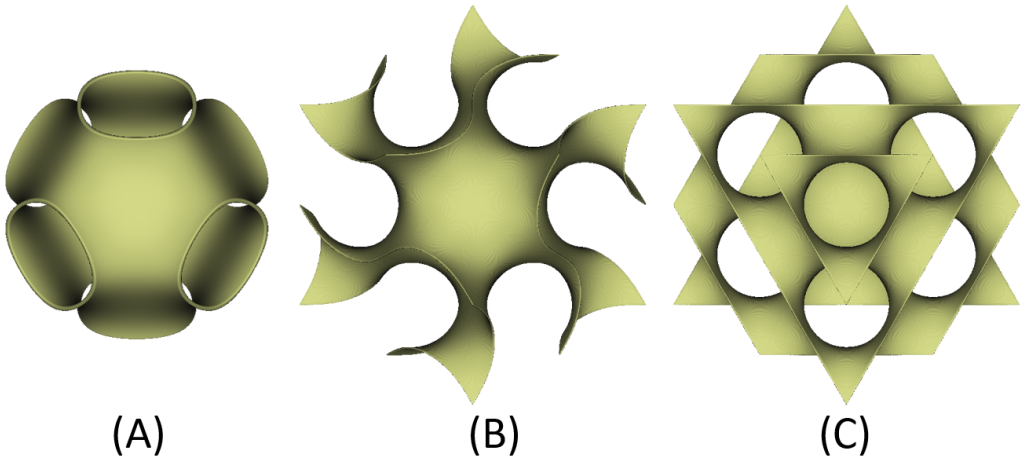

Figure 2.3: TPMS unit cells: (A) Schwartz, (B) Gyroid, and (C)Diamond

2.4.1 Implicit modeling

Implicit modeling uses equations rather than groups of edges, nodes, and faces [57]. As per implicit functions, the return to the function will be a positive value if any point lies outside of it in the 3D space, will return a negative if a point is inside it,

and a zero value if a point is on it [56] as shown in Figure 2.4. Models from implicit functions have exact shapes, continuous, smooth curvatures, and are easy to compute, unlike discretized representations, such as B-reps and mesh [57]. A difference in mesh and implicit representation of a sphere is shown in the figure 2.5.

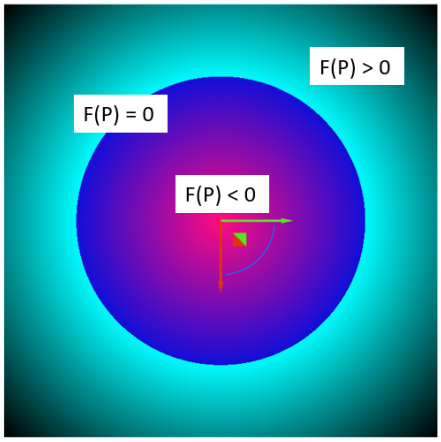

Figure 2.4: Visualization of an implicit function

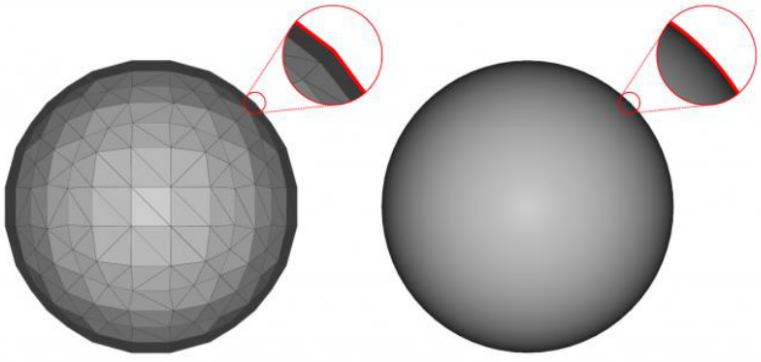

Figure 2.5: Representation of a sphere as mesh and implicit function [57]

A solid is an enclosed volume in explicit 3D modeling, whereas it is represented as a field in implicit modeling. Due to AM technology, designers have the freedom to generate unrealistic designs such as a void space in a solid body. A component's

interior is assumed to be homogeneous in a B-Rep model, whereas its boundary is sufficient to characterize it completely [58]. Lattice structures with functionally graded density can be easily modeled and stored using implicit modeling as compared to explicit modeling because it is simple to describe them using equations. Therefore, implicit models are far more efficient to work with AM technology as a next-gen manufacturing process.

2.4.2 Conjugate Heat Transfer (CHT) analysis

Conjugate Heat Transfer (CHT) can be defined as the combination of heat transfer between the fluids and solids [59]. The difference between conjugate and convective heat transfer is shown in Figure 2.6. For any conjugate heat transfer problem, governing equations are [60]:

For steady or unsteady flows in the fluids

1. Law of mass conservation (The continuity equation)
2. Law of momentum conservation (Navier-Stokes equation)
3. Law of energy conservation (energy equation as per flow dimensionality)

For steady or unsteady conduction in the solid

1. Unsteady energy equation
2. Steady Laplace/Poisson's equations
3. 1D steady or unsteady conduction considering negligible conduction in other dimensions for heat conduction through thin plates

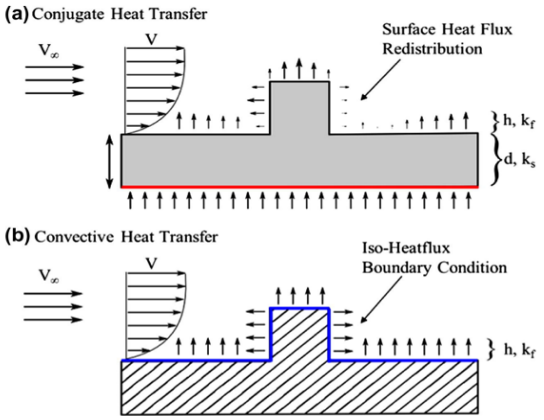

Figure 2.6: Difference between (A) Conjugate and (B) Convective heat transfer [61]

2.5 Traditional fabrication of Heat Exchangers

The most commonly used heat exchanger is the shell-and-tube type, where tubes are attached to tube sheets mechanically, and sheets are inside a shell containing inlet and outlet ports [62]. Tube sheets are either fixed or expanded/contract as per thermal stresses. For expansion/contraction, either expansion bellows are used, or one of the tube sheets floats inside the shell. This arrangement enables pulling the bundle assembly from the shell to clean the shell circuit. As per the Tubular Exchangers Manufacturers Association (TEMA), the size of shell diameter is around 10"-100". Also, tube sizes range from 0.625"-1.5" are generally made from copper, stainless steel, and other materials. Tubes are either welded or drawn and seamless. Tubes are welded with high-quality electro-resistance weld. The effective heat transfer rate of the heat exchanger is improved by either increasing the surface area of the available metal surface or allowing fluid turbulence using surface enhancements [62].

A flat, round metal piece is used to prepare tube sheets [62]. There are holes drilled at precise locations at the tube ends in a pattern with respect to one another.

Tube sheets are fabricated for the same range of material available for tubes. Tubes are joined to the tube sheets either using pneumatic/hydraulic pressure or roller expansion. One or more grooves are machined in tube holes, or holes are drilled and reamed as per requirement because it improves the strength of the tube joint. A layer of a high-quality metal alloy is bonded with tube sheets to enhance corrosion resistance. Distance, as well as the angle between the tubes and with respect to the flow direction, varies to control flow velocities and pressure drop for achieving maximum contact surface and turbulence for better heat transfer. The joint strength between tube and tube sheet is further enhanced by applying a strength weld or a seal weld. There is a fusion of materials rather than metal addition in these welds. A double tube sheet is introduced where it is necessary to avoid intermixing of fluids. The outer tube sheet is on the outside to eradicate any chances of intermixing, whereas the inner tube sheet is open to ambient so that that fluid leakage can be detected easily [62].

A pipe up to 24" diameter or a rolled and welded metal plate can be used for the construction of shell [62]. A 24" diameter shell pipe is commonly used because it is cheaper and can be easily manufactured as well as its roundness is near to perfect as compared to rolled and welded shells. The primary reason attributed to the roundness and consistency of shells is limiting space between baffle on the outer edge and the shell because more space will allow fluid to bypass and decrease heat exchanger performance. Roundness is a crucial factor, and it can be enhanced by either double rolling when longitudinal seam welding is done or by shell expansion around a mandrel. In rare cases, casting and boring of the shell are done to bring it to the correct inner diameter. For preventing issues of cavitation, erosion by fluids,

and vibrations, impingement plates are added for the even distribution of fluid going into the tubes where fluid velocity coming out from the nozzle is high [62].

Bonnets or end channels are generally cast or fabricated to manipulate flow in the tube-side of the tube circuit [62]. A gasket is placed between metal surfaces, and then the bonnet/end channel is bolted with the gasket and joined with tube sheets. A better way of sealing is to install an O-ring. There are ribs present in the head to create one or more passes of tube fluid through the bundle of tubes. Both front and back portions of the head pass ribs and gaskets should be matched to allow fluid flow through different tubes simultaneously. Pass ribs are cast with cast heads, and then, they are flat machined whereas, for separately manufactured heads, it is welded [62].

There are baffles installed for two major reasons [62]. Firstly, they provide support to tubes in the assembly, and while operating, they reduce vibrations caused by turbulence. Secondly, they control the direction of fluid on the shell-side for effective distribution of flow velocity, and consequently, heat transfer becomes more efficient. Baffles are either punched or machined from usual materials used to manufacture heat exchangers as well as suitable for fluid flowing on the shell-side [62].

The second-most used heat exchanger is the plate-type and is manufactured in many forms [63]. One of the simplest forms is to keep corrugated and flat sheets at right angles to each other alternatively. Moreover, fins can be added to these corrugated sheets and can also be stamped to enhance turbulence with the help of waves, slits, steps, and joggles. Passages for fluid in the sheets are formed by pressing or stamping operations, and then the sheets are either brazed or seam-welded. Stampings are generally in the form of single and long serpentine flow passages or any arrangement as per the application requirement. Flat-plate type heat exchangers

are cheaper due to the per unit surface area available in a sheet stock compared to tubing, which makes them ideal for compact heat exchanger applications. Also, passages fabricated for plate type can be aerodynamically clean, ensuring minimized pressure losses, but seam-welded joints can generate cracks due to stress concentration if the pressure difference is large [63].

For automotive applications, the most widely used heat exchanger is the plate fin-and-tube type in which fins from aluminum and copper are stamped and stacked in a jig, and then tubes are pressed in places [63]. To lower air-side flow resistance, tubes are generally flattened and coated with a layer of brazing or solder alloy so that it can be later brazed or soldered in a salt bath or furnace. In the case of automotive radiators, the entire heat exchanger unit is either soldered or brazed in a single operation [63].

2.6 Additive Manufacturing of Heat Exchangers

To date, traditional manufacturing involving casting, milling, drilling, and forming is used to manufacture heat exchangers [11]. It is a 'subtractive' technique that removes excess material to get final geometry. Moreover, parts are joined using brazing or welding, which may not ensure water-tight geometry. AM can overcome these shortcomings where a CAD design can be fabricated directly as a single part, and there is more control over designing very complex structures at small length scales. However, there are challenges associated with AM, such as control over surface-roughness, optimization of process parameters, raw material compatibility, competitiveness in cost, etc., but AM technologies are used successfully to manufacture heat exchangers from metals, ceramics, and polymers [11]. This review explores design opportunities in

metal AM and studies on TPMS based heat exchanger designs, being a growing interest lately.

New heat exchanger designs based on topology optimization, tree-based distribution, internally finned tubes, finless tubes, web-based tubes, novel shapes, innovative microchannels in the manifold, and bio-inspired waves-like microchannels are explored [64]. Massive weight and volume reduction of nearly 66% and 50% respectively with equivalent performance to a conventional design was observed with fuel-cooled oil cooler heat exchanger, fabricated from SLM technology [65]. Similarly, a compact twisted shell and tube heat exchanger was redesigned and manufactured using SLM, producing 40% improvement in heat transfer coefficient numerically [66]. It is due to reduction in the boundary layer as a consequence of secondary flow generated within axial flow because of swirl design [64]. From the fluid dynamics [67], it is known that there is a significant decrease in pressure drop in a gradually enlarging or contracting flow as compared to sudden expansion or contraction. TPMS topologies, with their inherent architecture, allow smooth flows which can minimize pressure theoretically, have intertwining channels running over one another partitioning space into two disjoint areas, and are continuous simultaneously [68]. These interpenetrating structures can improve turbulence in fluid flow, thus, improving heat and mass transfer[69]. Also, these structures have advantages of better mechanical [70] and anti-fouling [71] properties, making them a great candidate for heat exchanger design.

The application of TPMS in heat and mass transfer devices was first introduced by Slaughter [72]. Benefits of high thermal performance and lightweight enabled it to use them for heat exchangers [73]. Peng at el. [48] investigated a co-axial heat exchanger and showed that TPMS could be used for enhancing thermal effectiveness

in a heat exchanger. TPMS such as Schwartz, Gyroid, and Diamond were further investigated [74]. Thermal conductivity of Schwartz P was higher than gyroid for different porosity values and cell sizes as per Smith at el. [75], which concluded that thermal conductivity strongly depends on porosity. A comparison between the two most studied TPMSs, Schwarz D and Gyroid, based on flow and thermal transport properties concerning baseline design of printed circuit heat exchanger by Li at el. [68]. The turbulence model used was k-omega SST for CFD analysis. It was found that there is a considerable improvement of about 16-120% in heat transfer coefficient for TPMS compared to printed circuit heat exchangers at a given pumping power. TPMS topologies can also be represented as a network of sheets, and these have a very high surface-area-to-volume ratio [76]. A numerical comparison of thermal-hydraulic characteristics of sheet and solid networks of diamond and gyroid TPMSs, along with graded structures, was performed by Al-Ketan at el. [77] and observed that sheet gyroid has the highest overall heat transfer coefficient.

Hence, there was a motivation to further investigate sheet-based gyroid for a compact heat exchanger by varying parameters such as cell size and wall thickness to meet the required target performance of a WCAC and ensure its manufacturability by LPBF as a part of this thesis.

Chapter 3

Methodology

3.1 Design calculations

Designing a heat exchanger is a process involving iterations (trials and errors) [78]. A set of steps that are implemented is:

1. Calculate required 'UA' from heat transfer rate and basic heat exchanger design methods (LMTD, ϵ-NTU)
2. Select liquid flow and airflow cross-sections/channels for keeping low velocities (important for air-side to decrease ΔP)
3. Estimate thermal performance using either established correlations or computational analysis tools
4. Determine weight based on geometry selected
5. Iterate the above steps to try to meet or reduce targets

A heat exchanger specification sheet is a fact sheet that helps to choose design methodology and heat exchanger type for a particular application. It consists of input information needed and design calculations. This sheet is available on Microsoft Excel, and for our application, it is shown in the figure 3.1. When the heat transfer coefficient on the gas side is low and the overall conductance 'UA' gets dominated by it, the obvious choice is to select a cross-flow arrangement [78]. A WCAC is inherently a cross-flow heat exchanger, where hot air flows across the heat exchanger and gets cooled by water pumped perpendicular to the airflow direction plane. For our study, too, we shall consider the heat exchanger type to be cross-flow, and from the heat exchanger specification sheet, the 'UA' required for given heat exchanger design conditions is 1085.978 kW/°C.

	A	B	C	D	E	F	G	H	I	J	K	L
1	**Preliminary Heat Exchanger design (S.I. Units)**											
2	**Estimation of overall conductance (UA)**											
3												
4	**Inputs**						**Calculations**					
5												
6	$Fluid_1$ mass flow rate (m_1) =			0.235	kg/s		Heat Transfer rate (Q) =				28.007	kW
7												
8	$Fluid_1$ inlet temperature ($T_{1,in}$) =			160	^{0}C		Log mean temperature difference (ΔT_m) =				25.790	^{0}C
9												
10	$Fluid_1$ outlet temperature ($T_{1,out}$) =			42	^{0}C		Overall conductance (UA) =				1085.978	kW/^{0}C
11												
12	$Fluid_1$ specific heat (C_{P1}) =			1.010	kJ/kg.K		$Fluid_2$ outlet temperature ($T_{2,out}$) =				56.130	^{0}C
13												
14	$Fluid_2$ mass flow rate (m_2) =			0.413	kg/s							
15												
16	$Fluid_2$ inlet temperature ($T_{2,in}$) =			40	^{0}C							
17												
18	$Fluid_2$ specific heat (C_{P2}) =			4.200	kJ/kg.K							
19												
20	**Equations used for calculations:**											
21												
22		$Q = \pm (m_1)(C_{P1})(T_{1,in}-T_{1,out})$										
23												
24		$Q = \pm (m_2)(C_{P2})(T_{2,in}-T_{2,out})$										
25												
26		$\Delta T_m = [(T_{1,in}-T_{2,out})-(T_{1,out}-T_{2,in})]/\ln[(T_{1,in}-T_{2,out})/(T_{1,out}-T_{2,in})]$										
27												
28		$Q = UA\Delta T_m$										

Figure 3.1: Heat exchanger specification sheet [78]

3.2 Potential heat exchanger designs

Along with manufacturing methods, conventional heat exchanger designs have some drawbacks considering heat exchanger design requirements. Although shell-and-tube heat exchangers possess the highest numbers in maximum temperature and pressure, they are mainly heavy and bulky & provide very low surface area per unit volume [48]. On the other hand, Plate-fin and plate-and-frame heat exchangers have a high surface-area-to-volume ratio. However, they are limited to moderate to low pressure and temperature applications. Moreover, these two types exhibit a significant pressure drop due to fouling in small channels. Finally, printed circuit heat exchangers achieve the best thermal performance amongst all. However, again, large pressure drops are associated with them, as well as they are fabricated from an expensive chemical etching process. A comparison table based on surface-area-to-volume ratio, maximum possible operating temperature (T_{max}), and pressure (P_{max}) is shown in Table 3.1 [48].

Table 3.1: Comparison table of different heat exchangers [48]

Heat exchanger type	**Surface area/Volume (m^2/m^3)**	**T_{max} (°C)**	**P_{max} (bar)**
Shell-and-tube	50 - 100	1100	1000
Plate-and-frame	120 - 660	815	200
Plate-fin	800 - 1500	800	200
Printed circuit	200 - 2500	980	900

As compared to all these designs, the surface-area-to-volume ratio for TPMS based gyroid is as high as 3000 m^2/m^3 [48], which makes TPMS structures perfect for compact heat exchanger applications. Moreover, TPMS is a topologically optimized lightweight design, which will help reduce weight. Figure 3.2 shows the variation of surface-area-to-volume ratio with the periodic length for a gyroid TPMS.

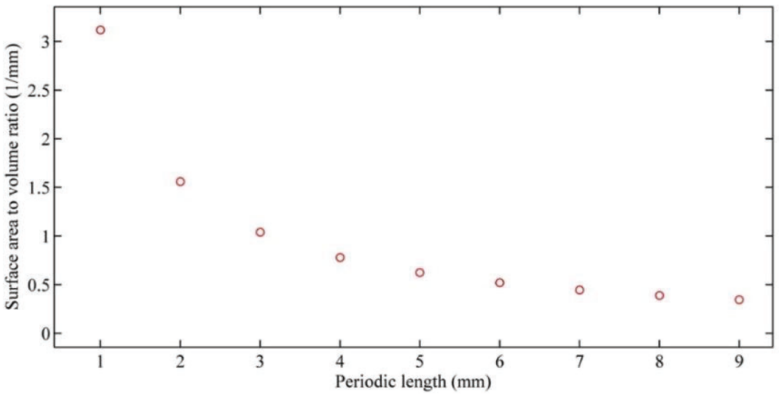

Figure 3.2: Variation of surface-area-to-volume ratio with periodic length for gyroid TPMS [48]

For achieving optimal heat exchanger design performance, design factors of TPMS such as TPMS type, wall thickness, periodic length, and offset parameter need to be understood before starting with design [48].

- **TPMS type:**

  TPMSs primarily explored in the research are Schwartz, Gyroid, and Diamond. For each TPMS, there are unique flow characteristics, pressure drop, and heat transfer [48]. For example, Schwartz may have a low-pressure drop due to its straight channels, whereas heat transfer in the gyroid is better due to its helical flow pattern. TPMSs can be further divided in the form of solid-network and sheet-network. A sheet network is thickened minimal surface, whereas a solid network is solidified volume surrounded by the minimal surface [79]. Manufacturability is also different for different TPMSs and depends on scaling the periodic length to be self-supporting as well as maximum operating pressure and temperature [48]. Mass per unit volume ratio is also essential while considering topology optimization and lightweight, especially for compact heat exchanger

applications.

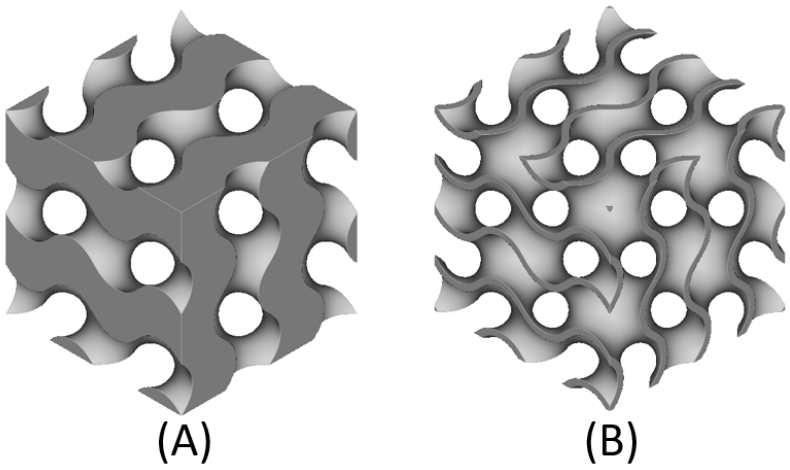

Figure 3.3: (A) Solid-network and (B) Sheet-network of gyroid TPMS

- **Wall thickness:**

  Wall thickness is a principal factor for any heat exchanger design. Lowering wall thickness will enhance heat transfer between flowing fluids because the wall thermal resistance will decrease. However, as per the machine capabilities, it is necessary to determine the lowest wall thickness that is printed without failure [48].

- **Periodic length:**

  As shown in the figure 3.2, with increasing periodic length, the surface-area-to-volume ratio decreases but large pressure drops will get induced for lower values of periodic length [48]. Hence, a trade-off is necessary to consider between surface-area-to-volume ratio and pressure drop for design. Periodic length also determines the unit cell size. The unit cell size of Diamond TPMS beyond

a considerable size is not self-supporting, whereas Gyroid TPMS can be self-supporting at any unit cell size.

- **Offset parameter:**

  The offset parameter is used to shrink or expand one channel relative to another [48]. When the offset parameter is zero, the interpenetrating channels of TPMS are equally divided in 3D volume. If TPMS has a non-zero offset, one fluid channel will expand, and the other will shrink. The offset parameter becomes useful when heat transfer efficiency and hydrodynamic resistance of flowing fluids are considered and thus, can be adjusted for design optimization [48]. Figure 3.4 shows a gyroid TPMS with a unit cell size of 5 mm. Two fluids are separated by a gyroid TPMS wall of 0.5 mm thickness. By increasing offset to positive, one fluid occupies more region than another. In contrast, if the offset is decreased to a negative value, another fluid will occupy more space than the first one.

After considering all factors, gyroid TPMS is most suitable for our heat exchanger design application because of the following reasons:

1. It is self-supporting for all unit cell sizes
2. It has the lowest mass per unit volume ratio
3. It has a moderate surface-area-to-volume ratio

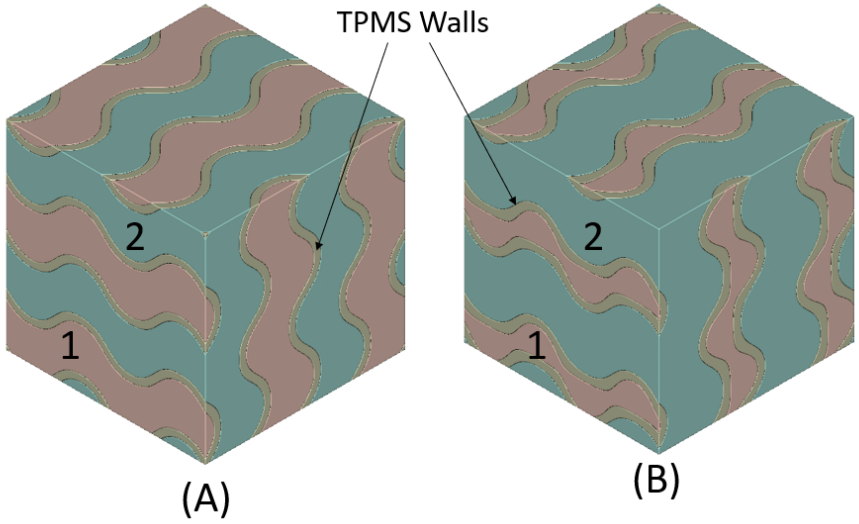

Figure 3.4: Fluid 1 and Fluid 2 are flowing in Gyroid TPMS with unit cell size 5 mm. (A) shows zero offset and (B) shows +0.5 offset where Fluid 1 region gets shrunk and Fluid 2 region gets expanded

3.3 Computational modeling

3.3.1 Design

nTopology is one of the standout packages, which implements implicit modeling to design computational models of complex geometries such as TPMS. It is powerful and relatively easy to use with respect to other modeling packages and therefore, it is used for this research study. Some of the practical benefits which it offers are as follows [80]:

- Unbreakable geometry
  - High geometric complexity
  - Fast and robust
  - Compatible with the engineering process

- Field-driven design
  - Pre-validated results
  - Multiphysics application
  - Benefit from existing engineering concepts
- Repeatable workflows
  - Completely configurable
  - Reusable and repeatable

A workflow in nTopology contains nTop Blocks and a catalog of these blocks is in nTop Notebooks. nTop Blocks are fundamental building entities that represent simple as well as advanced design functions such as [80]:

- **Conventional analysis:** engineering simulations, topology optimization, etc.
- **Advanced features:** surface textures, lattice structures, gyroids, etc.
- **Modeling operations:** variable shelling, boolean operations, rounding, etc.
- **Knowledge in engineering:** analytical formulae, engineering data, etc.
- **Pre-processing in AM:** hatching, slicing, support generation, etc.

TPMS models in nTopology can be easily created by first creating primitive shapes such as cubes, cuboids, cylinders, etc., over which TPMS can be mapped. Then TPMS nTop block in the implicit category under the Lattices feature is used. After inserting **cell size** (periodic length over X, Y & Z), **approximate bias length** (offset parameter) and **fill type** (Gyroid, Schwarz, Diamond, etc.), and dragging and dropping primitive shape in **body**, one can finally get a TPMS model. Figure 3.6 shows a Gyroid TPMS of cell size 5 mm and 0 mm bias length mapped over a cubic box of length 10 mm.

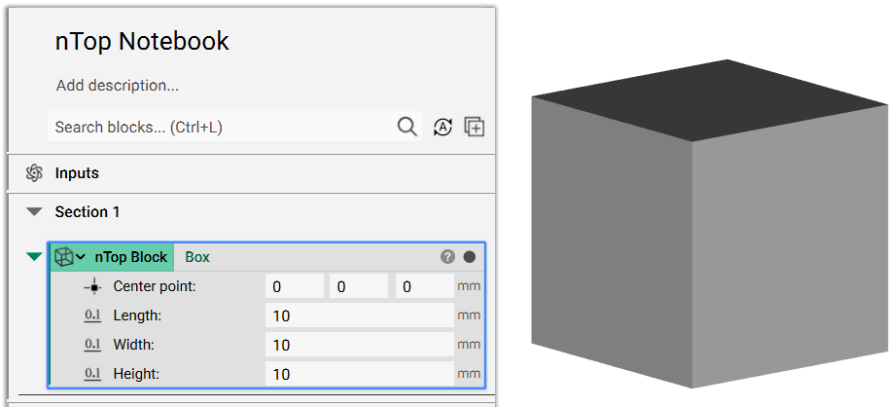

Figure 3.5: A typical nTopology workflow containing a nTop Block within nTop Notebook

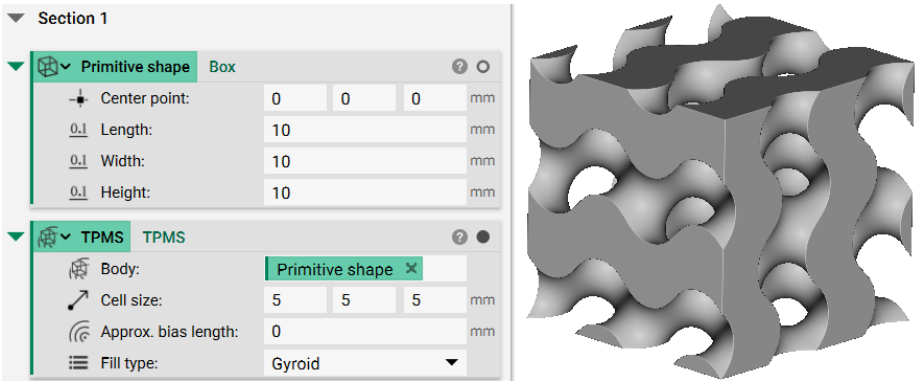

Figure 3.6: An implicit model of Gyroid TPMS in nTopology

One of the ways to design a heat exchanger with Gyroid TPMS would be to understand the performance as a representative volume element that comprises the core of the heat exchanger. Modeling a full-scale heat exchanger is computationally expensive. So, it is wise to break down a full-scale heat exchanger in representative volume elements and utilize boundary conditions in CFD to investigate thermal performance. As described in the equation 2.2.4b, to calculate the overall heat transfer coefficient, we need to calculate convection heat transfer coefficients of both hot and cold fluids. If the periodicity of the TPMS is constant, a section of the domain can

be assumed as a representative volume element for CFD analysis.

For designing a representative volume element of a Gyroid TPMS based heat exchanger, three domains are required, i.e., hot domain for hot fluid flow, cold domain for cold fluid flow, and gyroid heat exchanger wall as a solid domain. Considering a primitive shape of the unit cell to be a cube of side length 20 mm, a 'walled TPMS' with cell size 10 mm, a wall thickness of 0.5 mm, 0 mm bias length, and fill type gyroid, can be mapped on the cubic unit cell. A separate 'TPMS' for either hot or cold domain with the same parameter values can be created and subtracted from walled TPMS using boolean subtraction operation. The second fluid domain can be obtained again using boolean subtract by subtracting walled TPMS and first fluid domain TPMS from cubic unit cell. Figure 3.7 shows a representative volume element of the gyroid core of a heat exchanger created in nTopology.

There are several more options within nTopology to further enhance the model for downstream workflow. One of the options is smoothing the implicit body by using Smoothen Body nTop Block. This block rounds some of the edges and produces cleaner geometry for meshing.

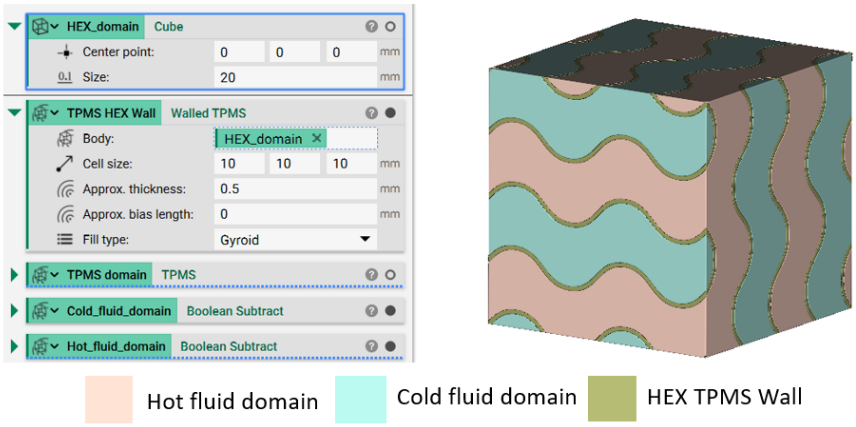

Figure 3.7: Representative volume element of Gyroid core modeled in nTopology

3.3.2 Meshing

nTopology supports the meshing of designed implicit bodies and exports it in the form of STL/OBJ format. It provides a range of options within meshing to create high-quality surface and volume meshes of implicit bodies. These meshes can be further either converted to be compatible with Finite Elements Analysis (FEA) by inserting boundary conditions on particular faces within nTopology or can be exported to FEA specific packages in STL/OBJ formats such as ANSYS, Star-CCM+, etc. and then, convert in FE model for analysis in that particular package. The latter option is robust with an established workflow and will be used for this study.

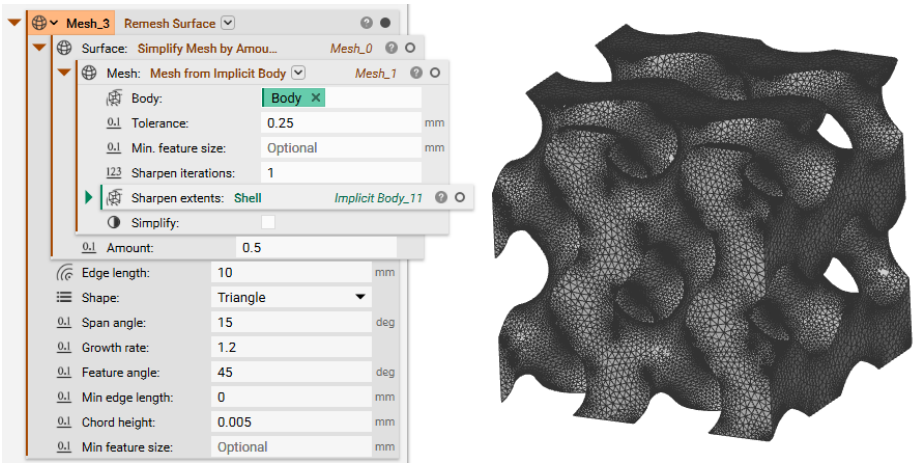

Figure 3.8: The meshing of gyroid unit cell in nTopology

Implicit bodies first mesh under 'Mesh from Implicit Body' with a tolerance value of 0.25 and 1 sharpening iteration. Under this mesh block, the mesh is very fine, and the mesh elements count is very high. So, the mesh is reduced using 'Simplify Mesh by Amount' to 50% of the original mesh size count. A final mesh is obtained under 'Remesh Surface', which further reduces mesh elements count but preserves sharp ends and high-quality mesh for further analysis. Figure 3.8 shows the meshing of a

unit cell of gyroid TPMS in nTopology.

After exporting the mesh from nTopology, boundary conditions to particular faces are assigned in ANSYS-SpaceClaim. Since the gyroid has a periodically repeating unit cell, periodic boundary conditions can be set to a pair of faces, apart from fluid domains' inlet and outlet flow conditions. Facet regions of the STL of fluid domains and solid domains are selected and assigned as a group in SpaceClaim, and then it is further exported to ANSYS Fluent-Meshing. Fault-tolerant meshing workflow in Fluent meshing is robust to handle complex meshes such as TPMS and FE mesh for CFD analysis in ANSYS Fluent can be obtained. Figure 3.9 shows polyhedral volume mesh obtained in Fluent meshing.

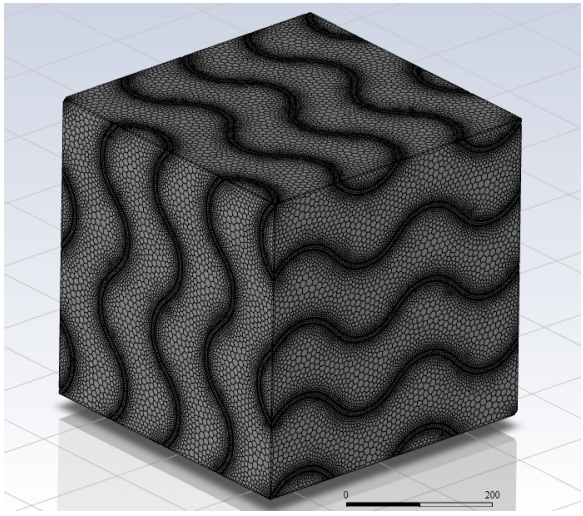

Figure 3.9: Volume mesh of gyroid unit cell with polyhedral elements in ANSYS Fluent Meshing

3.3.3 CFD setup

A Computational Fluid Dynamics (CFD) model was set up to predict the gyroid-based heat exchanger's fluid flow and thermal performance. As both heat transfer

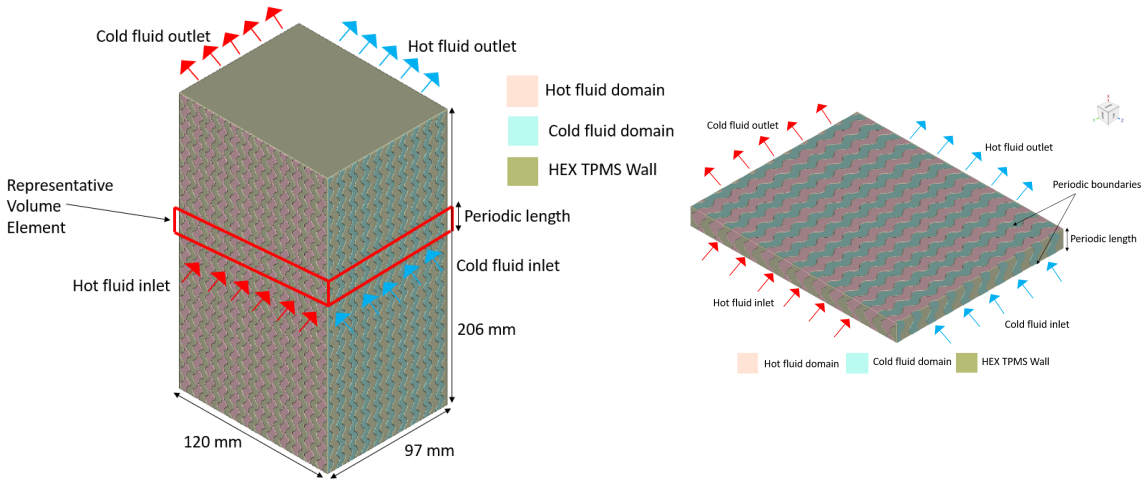

Figure 3.10: Geometry, computational model, and boundary conditions of gyroid heat exchanger core

and fluid flow are to be modeled, a multiphysics CFD simulation needs to be done, and so, the simulation package used was ANSYS-Fluent. After obtaining volume mesh under Fault Tolerant Meshing workflow from Fluent Meshing, the mesh was exported to Fluent solver. Conjugate Heat Transfer (CHT) method is used to couple flows to solid gyroid walls and model heat transfer physics. Both fluid flows are assumed to be incompressible, steady-state, and turbulent, and the turbulent model used is realizable k-ϵ. For saving computational time and taking advantage of gyroid being periodic, periodic boundary conditions can be applied to a pair of opposite faces apart from the faces where both fluids enter and exit. It gave a representative volume element (RVE) of the heat exchanger, and the height of the RVE model is the periodic length of the gyroid unit cell. Figure 3.10 shows the geometry of a full-scale gyroid infill heat exchanger core with a unit cell size of 7 mm and its RVE model with boundary conditions applied.

3.4 Parametric study

As mentioned previously, parameters of TPMS design such as periodic length, offset, and wall thickness can be analyzed in detail to study their effects on heat exchanger design performance. Furthermore, the impact of the aspect ratio of a gyroid unit cell is also studied. nTopology is very handy, fast, and robust to generate implicit models with variations and conduct a parametric or sensitivity analysis to optimize heat exchanger design. One of the exciting blocks in nTopology is Ramp, where a value can be changed gradually based on the object's distance field. It gives more flexibility in tweaking the design parameters of gyroid TPMS for further design optimization and improving heat exchanger performance.

3.4.1 Periodic Length

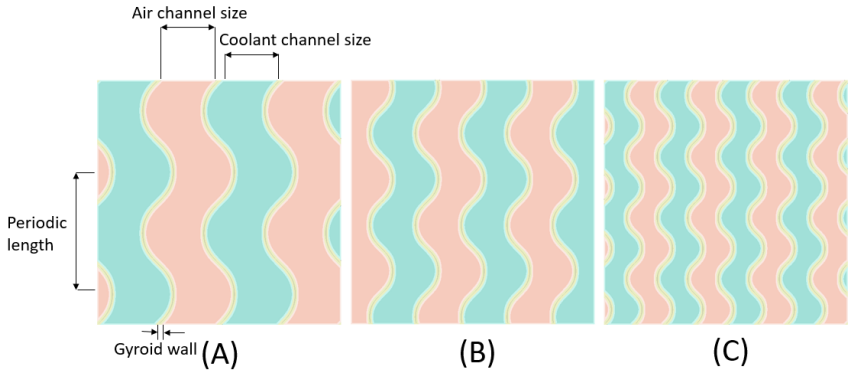

Figure 3.11: Gyroid unit cell with periodic length (A) 10 mm (B) 7.5 mm (C) 5 mm

The periodic length of a gyroid unit cell determines the size of the unit cell. As in the figure 3.2, the heat transfer rate is improved by decreasing periodic length because the surface-area-to-volume ratio increases, but there will be a compromise as fluid channels become narrower. So, the pressure drop may also increase. For analysis,

three gyroid unit cells with a cell size of 20 mm and periodic lengths of 10 mm, 7.5 mm, and 5 mm are considered and are shown in the figure 3.11.

3.4.2 Sheet gyroid thickness

In the case of sheet gyroid, the offset parameter 'K' is the level set that determines surface thickness equidistant from the actual minimal surface. 'K' represents the amount of material inside the lattice and controls volume fraction in a unit cell. For heat exchanger design, the air-side, which is the hot fluid domain, pressure drop has a stricter limit than the water-side, i.e., cold fluid domain. Therefore, it is favorable to expand the air-side against the water-side to maintain a low-pressure drop. In nTopology, sheet gyroid is Walled TPMS with gyroid infill. Figure 3.12 depicts sheet gyroid unit cells of cell size 20 mm with periodic lengths of 10 mm and thicknesses 1 mm and 3 mm.

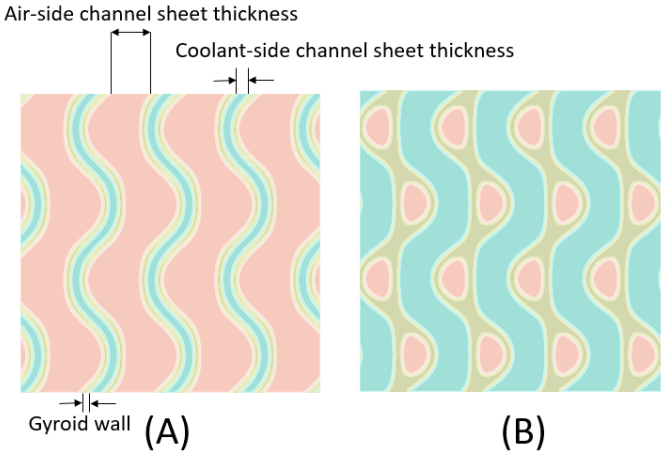

Figure 3.12: Gyroid unit cell with coolant-side sheet thickness (A) 1 mm (B) 3 mm

3.4.3 Wall thickness

Wall thickness has a significant role in the determination of heat exchanger performance. With AM technology, thin walls without voids or porosities are printed with high accuracy. Depending on AM process parameters, wall thicknesses as low as 0.5 mm are also printed. For example, the figure 3.13 shows a gyroid unit cell with wall thicknesses of 1 mm and 0.5 mm.

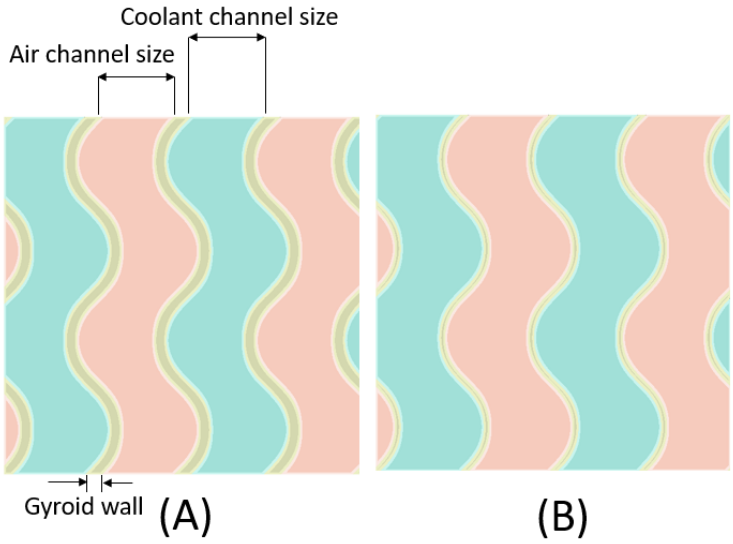

Figure 3.13: Gyroid unit cell with wall thickness of (A) 1 mm (B) 0.5 mm

3.4.4 Aspect ratio

Aspect ratio refers to the ratio of the size of an object in different directions. The fluid pressure drop is controlled by stretching the flow channel in the flow direction. Hence, the pressure drop along the air-side is lowered if the flow channel in the airflow direction is pulled. It is done by increasing the cell size of the gyroid unit cell in either one of the X, Y, or Z axes, where the fluid, whose pressure drop is to be controlled,

is flowing.

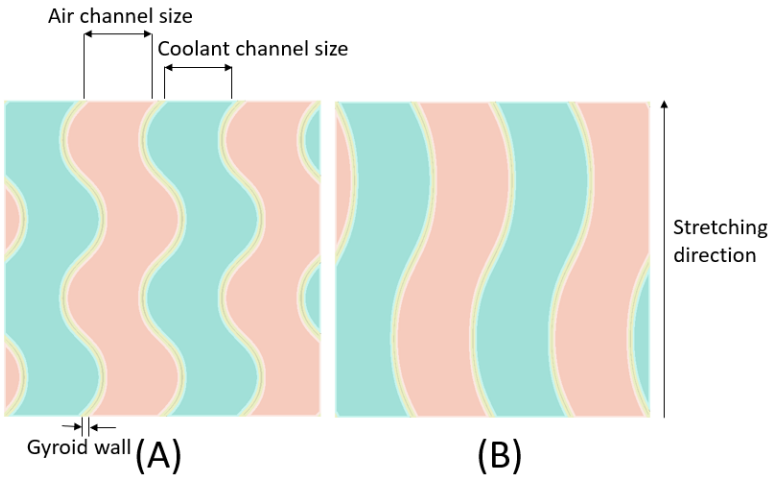

Figure 3.14: Gyroid unit cell with Z direction cell size (A) equal to length and breadth (B) twice of length or breadth

As mentioned before, in our heat exchanger, air-side pressure drop has to be maintained below 3 kPa. Therefore, airflow channels can be stretched in that direction. Figure 3.14 shows a gyroid unit cell stretched twice in height compared to its length and breadth.

3.4.5 Functional grading

It is observed that most of the heat transfer and heat exchange between hot and cold fluids occurs around the intersection space when fluids enter the heat exchanger. This concept can be exploited for the functional grading of gyroid unit cells. The fluid channels can be densely packed during entrance of fluids in the heat exchanger and then gradually expand for further length. Thus, this will enhance heat transfer between fluids in the initial phase of fluids entering the heat exchanger and, later, allow better fluid outflow to reduce pressure drop.

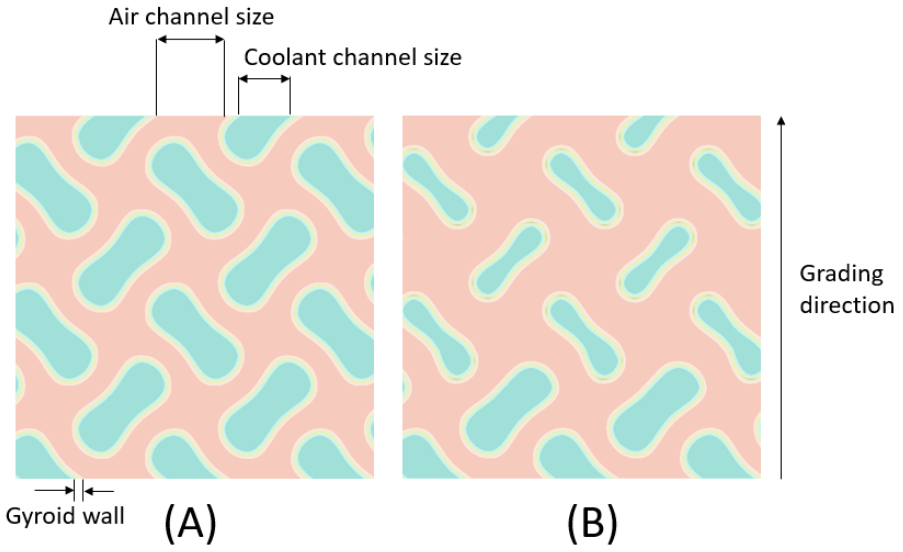

Figure 3.15: (A) Uniform gyroid unit cell with cell size of 8 mm (B) Functional grading of air-side gyroid unit cell thickness from 2 mm to 3 mm in Z direction

It again becomes crucial for the air-side flow, where we want a significant temperature drop and a low-pressure drop. As mentioned before, the Ramp block in nTopology can perform such uniform variation. Figure 3.15 shows the functional grading of air-side gyroid unit cell thickness from 2 mm to 3 mm in the unit cell of size 8 mm along the airflow direction.

3.5 Additive Manufacturing

Although computational modeling and CFD analysis helped determine design considerations and thermal performance for the fabrication of heat exchangers, it is necessary to check whether optimized designs can be manufactured using AM. AM enables fabricating complex geometries consisting delicate features with accuracy and efficiency but also depends on powder material, AM technique, process parameters,

etc. Therefore, material selection and AM technique are essential to ensure the manufacturability of designs optimized by computational analysis to develop an optimized heat exchanger design.

3.5.1 Material selection

From the heat exchanger point of view, as per equation 2.2.4b, a material with high thermal conductivity provides an ideal candidate for manufacturing. Considering automotive applications, it is necessary to evaluate materials used for general engineering parts manufacturing and can bear high loads but have lightweight designs, which is vital for reducing fuel/energy consumption. Moreover, materials compatible with AM and produce components with enhanced properties also need to be considered. Taking account of all mentioned considerations, AlSi10Mg is a convenient option for AM heat exchanger. A few of the key characteristics of the material includes

- Good hardness, strength & dynamic propoerties
- Good thermal conductivity
- High corrosion resistance
- Modification in properties using heat treatment

3.5.2 LPBF of design samples

Using computational modeling and CFD analysis, a parametric study optimized sheet network based gyroid heat exchanger core design. Before building a prototype out of it, it is critical to scrutinize the manufacturability of design using Additive Manufacturing. The AM technique used for manufacturing is LPBF. The LPBF can fabricate fine features due to its thin layer-wise manufacturing method. EOS M280 with 400 W

maximum laser power and Yb fiber laser & diameter of focus of 100 μm was used as the LPBF machine [81]. 13 samples were created based on the studied design parameters variations such as gyroid network type, unit cell size, changed aspect ratio, and wall thickness. Dimensions were cuboid-shaped with a length and breadth of 20 mm x 20 mm and support of 3 mm at the bottom, over which gyroid design were printed. These were printed under the environment of argon gas, filled in the build chamber, to reduce oxygen content below 0.1% and minimize oxidation [81]. 13 samples were replicated from the previous set but rotated by 90° to examine manufacturability in all possible directions. Table 3.2 shows details of the samples to be printed, and figure 3.16 shows the dimensions of one of the samples.

Table 3.2: Details of samples printed (A2 represents sample rotated by 90°w.r.t. A1)

Sample name	**Gyroid type**	**Unit cell size (mm)**	**Cell height (if changed) (mm)**	**Thickness (mm)**
A1, A2	Sheet	7	14	0.2
B1, B2	Sheet	7	14	0.5
C1, C2	Sheet	7	14	0.6
D1, D2	Solid	5	-	0.5
E1, E2	Solid	7.5	-	0.5
F1, F2	Sheet	10	-	0.5
G1, G2	Sheet	12	14	0.5
H1, H2	Sheet	10	14	0.5
I1, I2	Sheet	8	14	0.5
J1, J2	Sheet	6	14	0.5
K1, K2	Sheet	7	8	0.5
L1, L2	Sheet	7	10	0.5
M1, M2	Sheet	7	12	0.5

Table 3.3 shows a summary of process parameters with different laser powers, scanning speeds, and hatch spacings, keeping downward displacement of the platform to be fixed and equal to 30μm (recommendation from machine manufacturer

for AlSi10Mg). The scanning strategy used was stripe scanning because it provided a more uniform distribution of residual stress and higher building rates as compared to other scanning strategies [82] and the alternating angle was 67° [83]. The different process parameters were tested at different levels based on increasing volumetric energy density (VED) from minimum (40.48 J/mm^3) to maximum (102.77 J/mm^3) value.

$$VED = \frac{P}{v.h.t}\left(\frac{J}{mm^3}\right)$$

The optimized set of process parameters for LPBF of AlSi10Mg was referred from Balbaa, M.A., et al. [81] to obtain best build as given in the Table 3.4.

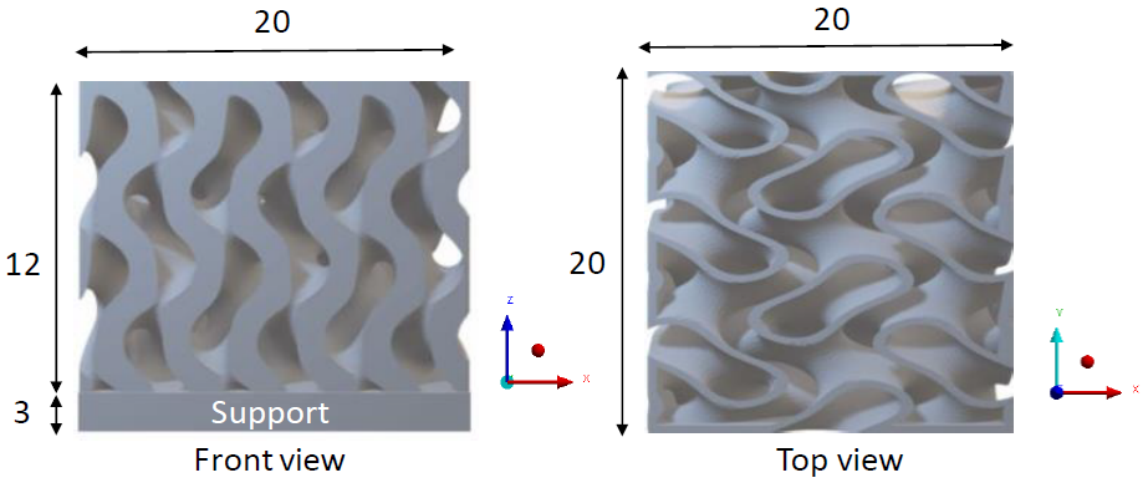

Figure 3.16: Different sectional views of a sample to be printed (all measurements are in mm)

Table 3.3: Process parameters for LPBF [81]

Laser Power P(W)	**Scanning Speed v (mm/s)**	**Hatch Spacing h (mm)**	**Layer thickness t (mm)**
300, 335, 370	800, 1050, 1030	0.15, 0.19	0.03

Table 3.4: Optimized process parameters for LPBF of AlSi10Mg [81]

Process parameter	**Value**
Laser Power (P)	335 W
Scanning speed (v)	1050 mm/s
Hatch spacing (h)	0.15 mm
Layer thickness (t)	0.03 mm
Energy Density (E)	70.89 J/mm^3
Stripe width (w)	50 mm
Stripe overlap (δ)	0.02 mm
Alternating angle	67°

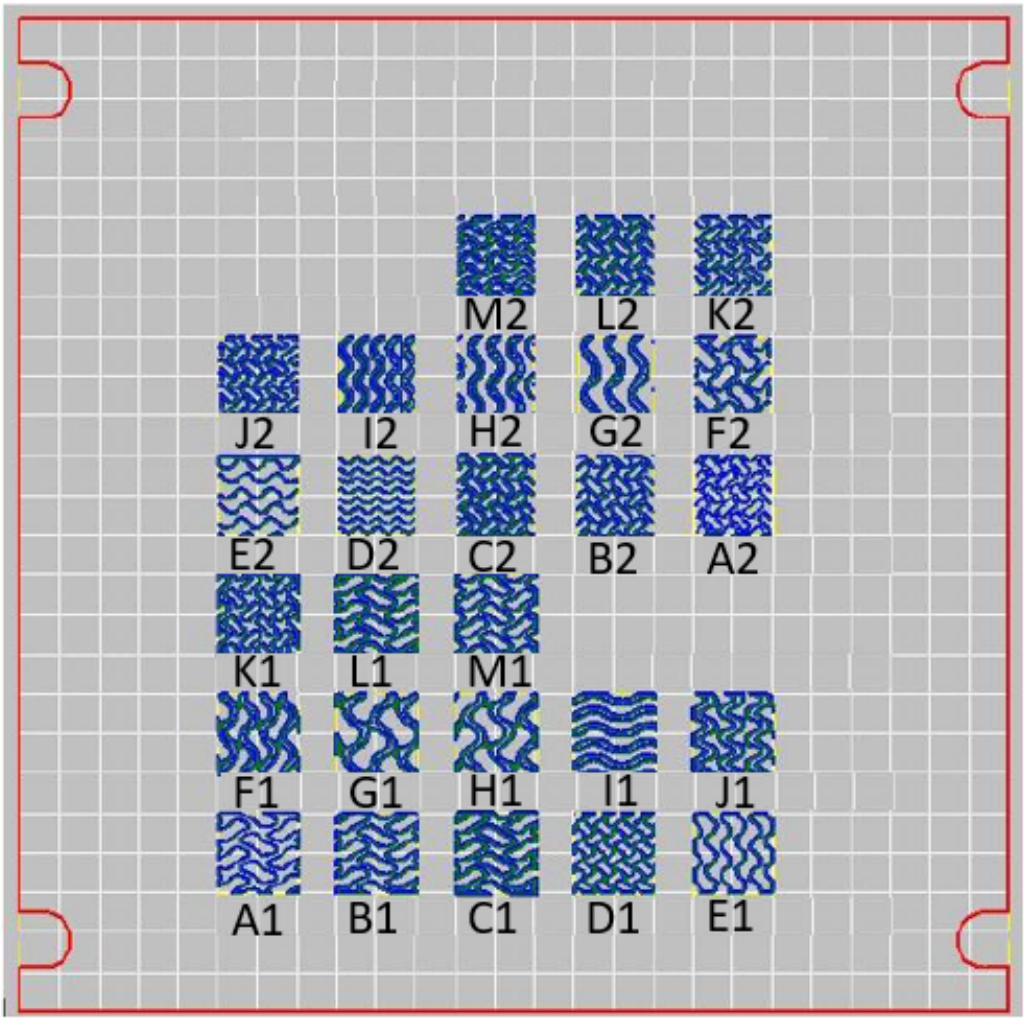

Figure 3.17: Samples arranged on build plate for LPBF

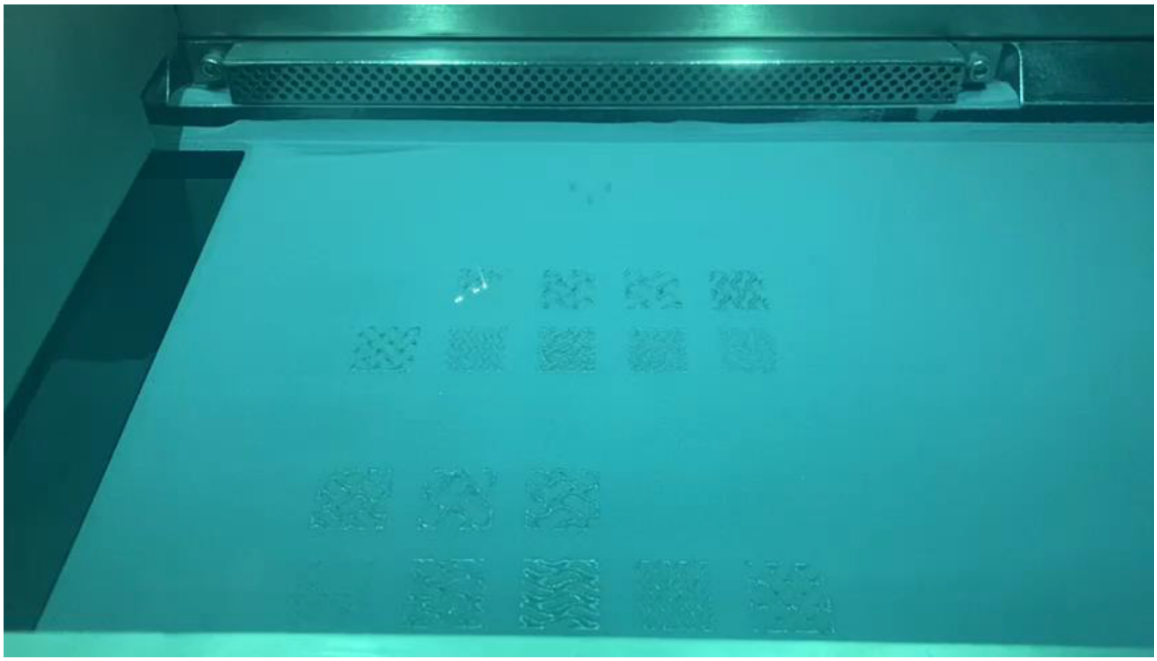

Figure 3.18: Samples getting printed using LPBF in EOS M280

3.6 Design & LPBF setup of prototypes

Based on the manufacturability of printed samples from parametric analysis, prototypes replicating actual WCAC were designed. Three gyroid unit cell sizes of (7, 7, 10), (7, 7, 14), and (12, 12, 14) were selected for designing prototypes amongst successfully printed samples and based on trends from the parametric study. Two prototypes with gyroid unit cell size (7, 7, 14) were designed, one with the coolant inlet and outlet were on the same side as well as the other with inlet and outlet on the opposite side, to compare the thermal performance based on the placement of inlet and outlet of coolant. Figure 3.19 shows the dimensions of the full-scale and the prototype model. The prototype model is geometrically scaled half to the full-scale model. Prototypes were designed using SolidWorks and nTopology. A vacant gap of

6 mm was kept between the heat exchanger core and the outer walls in the prototype to ensure smooth flowability of coolant into the gyroids, and the core filled. As per AM design constraints, support of 1 mm was added below the design to print gyroids, and thin cylindrical supports were added to support overhanging regions in the design. The final prototype model with a gyroid heat exchanger core with unit cell size (7, 7, 14) is shown in the figure 3.20. Considering space constraints in EOS M280, prototypes were printed in EOS M290. The set of optimized process parameters for LPBF of AlSi10Mg mentioned in the Table 3.4 was used for printing prototypes.

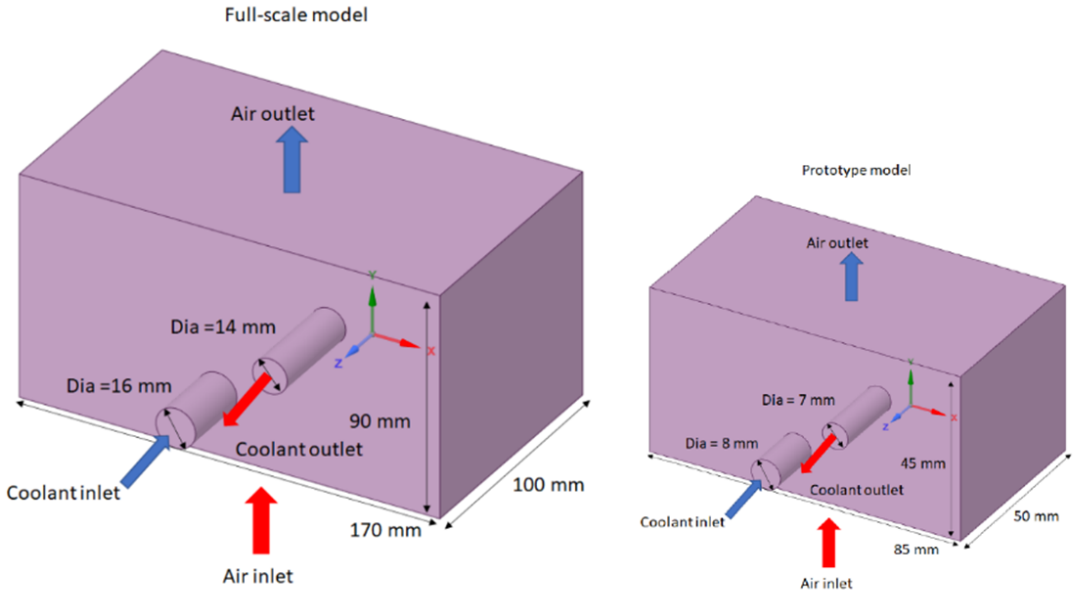

Figure 3.19: Dimensions of full-scale and prototype models of the heat exchanger

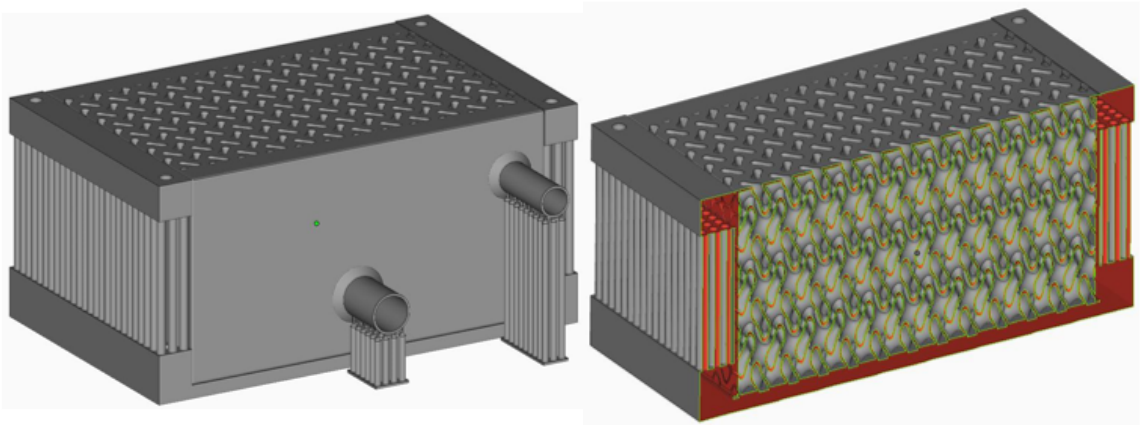

Figure 3.20: Gyroid based prototype model with cross section for printing

Chapter 4

Results

CFD results from the parametric analysis provided optimized gyroid unit cell design. A systematic workflow was employed to reduce the pressure drop of the fluid flows and increase temperature drop and total heat transfer rate of the fluids with the parametric analysis. After the parametric study, it was essential to examine the manufacturability of designs using optimized process parameters for LPBF of AlSi10Mg. It was done by doing a section cut in the gyroid unit cells coupons and using Keyence Optical Microscopy to investigate for any internal crack, void, or failure. Characterization using Optical Microscopy filtered out failed design variations and enabled to proceed with the successful designs for prototype design and manufacturing. Prototypes of WCAC were scaled half of the full-scale dimension, and the core of the heat exchanger was filled with gyroid infill and printed with previously used optimized process parameters for AlSi10Mg. A detailed discussion on the CFD results, including pressure drop, temperature drop, and heat rejection rate & manufacturability of gyroid-based heat exchanger designs, is done in this section.

4.1 Parametric analysis of gyroid using CFD

As previously discussed, TPMS can be represented as a solid network and sheet network. For gyroids, CFD analysis is performed for both solid and sheet networks. Considering possible TPMS design parameters such as periodic length, aspect ratio, functional grading, etc., design optimization of heat exchanger core using gyroid as TPMS was planned. This plan enabled to come up with the best possible design satisfying thermal and fluid flow requirements and can be eventually manufactured with LPBF using AlSi10Mg as a material with LPBF process parameters.

4.1.1 Solid network - Periodic length

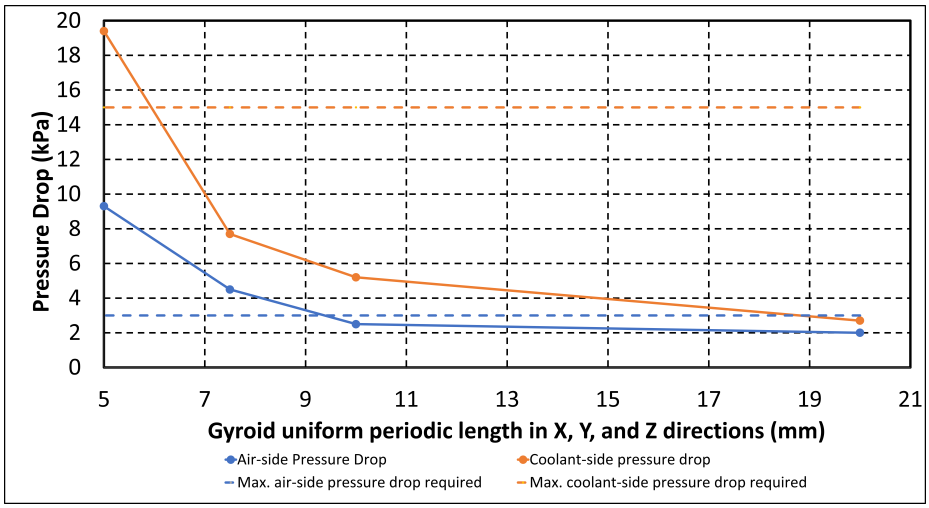

Figure 4.1: Area averaged pressure drop for air-side and coolant-side channels varying with solid network gyroid periodic length

Periodic length of gyroid serves as a good starting point to estimate appropriate unit cell size. Also, the figure 3.2 suggests decreasing surface-area-to-volume ratio with increasing periodic length. So, the choice of periodic length for a particular

application came from a trade-off between ideal heat transfer and required pressure drop. Figure 4.1 shows pressure drop of both air-side and coolant-side flows for different periodic lengths of gyroid unit cell ranging from 5 mm to 20 mm. As per the design, pressure drop of air-side and coolant-side flows is limited to 3 kPa and 15 kPa, respectively, shown as a dashed line in the graph. Therefore, it can be seen that a heat exchanger core with a gyroid unit cell size of nearly 9.5 mm and above can be designed & which can keep pressure drops of both fluids flowing within required limits. If a parametric analysis is considered, periodic length from 7.5 mm and above can also be considered as the difference between actual pressure drop and required pressure drop for air-side flow is close to only 1 kPa.

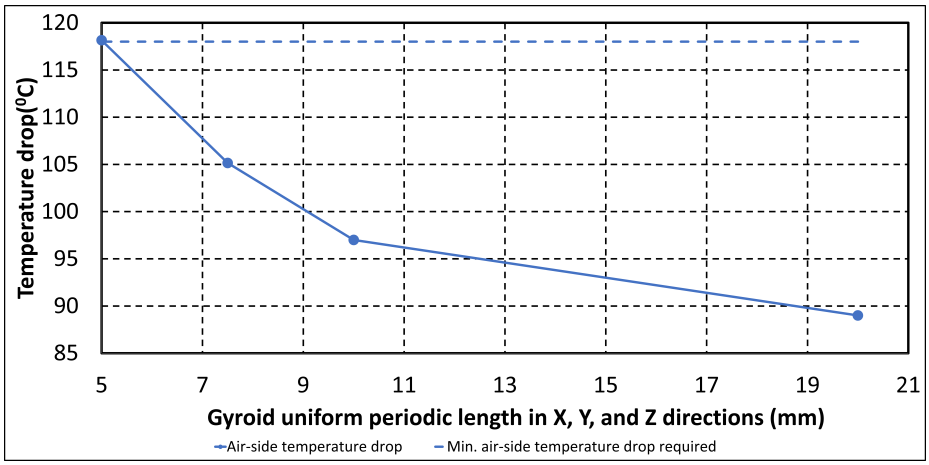

Figure 4.2: Area averaged temperature drop for air-side channel varying with solid network gyroid periodic length

The figure 4.2 and figure 4.3 show that the temperature drop and the heat rejection rate decreases with increasing gyroid unit cell size. This is evident from the figure 3.2 because the temperature drop and heat rejection rate in a compact heat exchanger strongly depends on the surface-area-to-volume ratio. The difference becomes as large as 20°C for gyroid unit cell size of 9.5 mm and starts decreasing continuously

with increasing cell size. Although pressure drop limitations are necessary for design considerations, a compromise with a temperature drop and total heat transfer rate with such large deviations from the required temperature drop and the heat transfer rate is unacceptable. Hence, parametric analysis using design variations becomes prominent to optimize the design of the heat exchanger core.

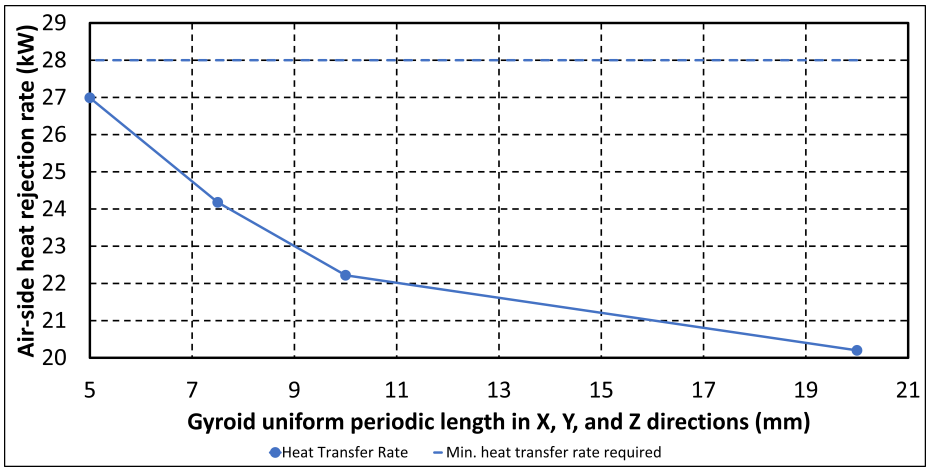

Figure 4.3: Heat rejection rate for air-side channel varying with solid network gyroid periodic length

4.1.2 Sheet network - Periodic length & thickness

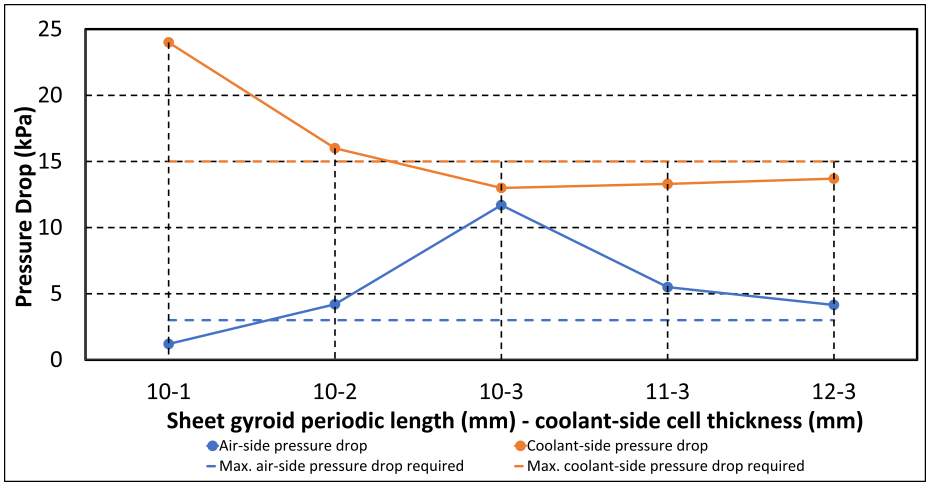

Figure 4.4: Area averaged pressure drop for air-side and coolant-side channels varying with sheet network gyroid periodic length and sheet thickness

Another design parameter is sheet thickness in a sheet network, along with periodic length. Figure 4.4 shows the effect of variation of gyroid periodic length and coolant-side thickness in a sheet network. As the coolant-side sheet thickness increases, air-side pressure drop increases because of shrinkage in the air-side channel. However, if the periodic length of the gyroid is increased, the air-side pressure drop decreases because the air-side channel is now more significant, providing lower resistance to airflow. Figure 4.5 shows the temperature drop for the same variations. It can be seen that temperature drop increases with increasing coolant-side sheet thickness. It almost reaches the minimum required temperature drop for the air-side but eventually decreases with increasing periodic length. The same can be seen for the heat rejection rate, as shown in the figure 4.6. Therefore, the sheet network of gyroid seemed to be a good design and was considered for further design optimization.

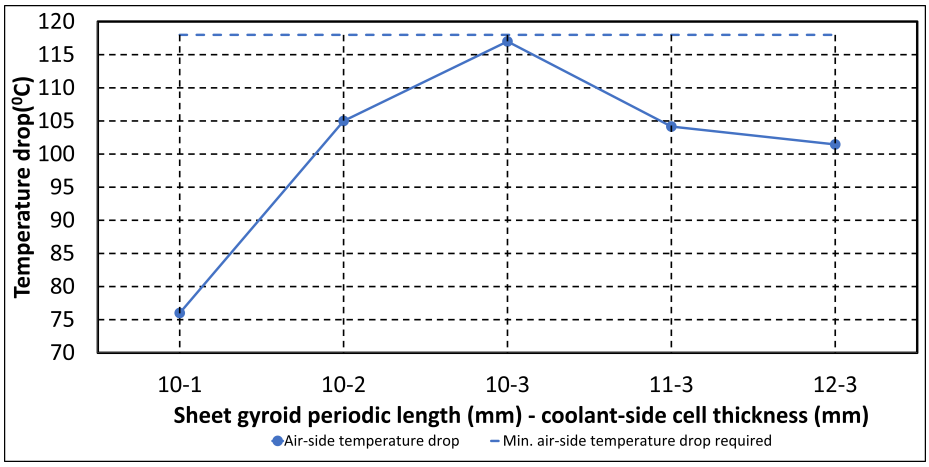

Figure 4.5: Area averaged temperature drop for air-side channel varying with sheet network gyroid periodic length and sheet thickness

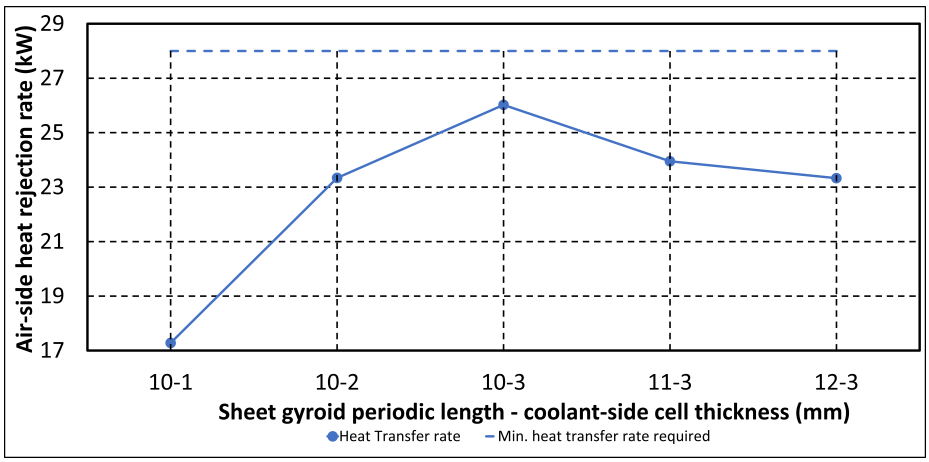

Figure 4.6: Heat rejection rate for air-side channel varying with sheet network gyroid periodic length and sheet thickness

4.1.3 Aspect ratio

Increasing sheet gyroid thickness resulted in required temperature drop on the air-side but beyond maximum permissible air-side pressure drop. Therefore, stretching airflow channels by increasing length along the airflow direction was considered viable.

Furthermore, the sheet gyroid with a unit cell size of 10 mm and a sheet thickness of 3 mm was studied by changing the aspect ratio of the unit cell along the airflow direction. The length of the unit cell in the airflow direction was doubled compared to the measurements along other two directions.

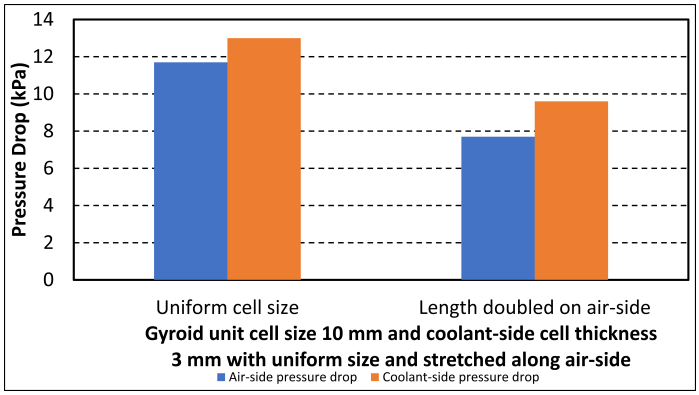

Figure 4.7: Area averaged pressure drop for air-side and coolant-side channels varying with gyroid unit cell length doubled along air-side

The column chart in the figure 4.7 shows the effect on pressure drop of air-side and coolant-side flows due to stretching of air-side flow channels' length doubled to its length in perpendicular directions. Stretching has helped reduce pressure drop values of both fluids' flows because channels are straighter and less intertwining with respect to channels originating from uniform gyroid unit cells. Hence, changing aspect ratio is a workable parameter for pressure drop limitations.

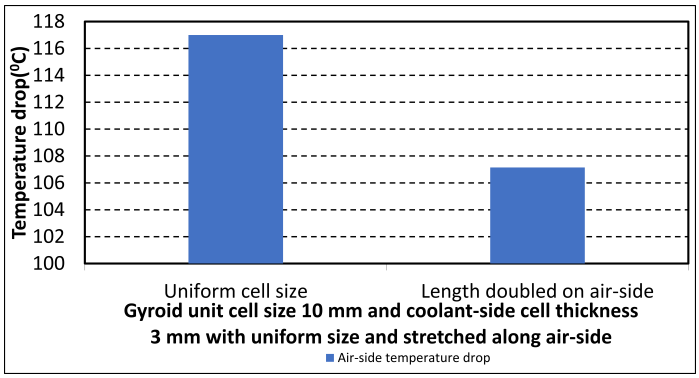

Figure 4.8: Area averaged temperature drop for air-side channel varying with gyroid unit cell length doubled along air-side

The drawback of introducing stretching inflow channels is a substantial reduction in temperature drop. The temperature drop of the air-side flow is below 108°C. Such low-temperature drop is attributed to lower surface-area-to-volume available in stretched flow channels. Figure 4.8 shows the comparison of temperature drop for both cases. A similar trend in the heat rejection rate in the figure 4.9 can be observed.

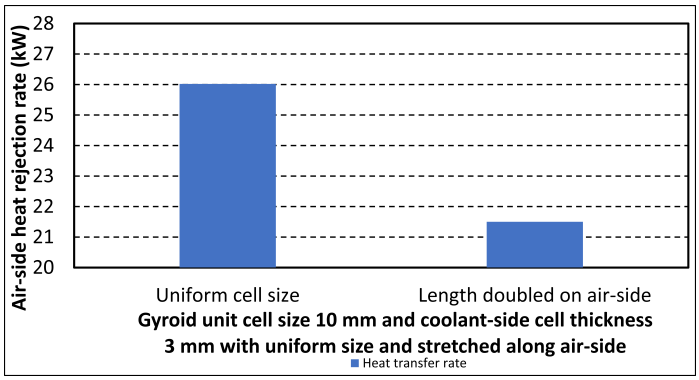

Figure 4.9: Heat rejection rate for air-side channel varying with gyroid unit cell length doubled along air-side

4.1.4 Functional grading

The concept of functional grading is used to create a contrast of cell sizes with variation along the channel's length to utilize efficient heat transfer between both fluids. Figure 4.10 represents pressure drop for both fluid flows with functional grading of air-side channel size from 2 mm to 3 mm in a gyroid unit cell of size 8 mm. There is a gentle increase in pressure drop on the air-side as the air-side channel size is 2 mm for 25% to 75% of total length. Both fluids' pressure drops are well within maximum permissible limits. Figure 4.11 depicts temperature drop on the air-side flow with functional grading of air-side channel size. There is a steep increase in temperature drop due to channel size ratio within air-side channel length. Moreover, the wall thickness, in this case, is 0.2 mm; else, the coolant channel will be blocked. Similarly, there is a rise in the heat rejection rate by implementing functional grading, which is shown in the figure 4.12.

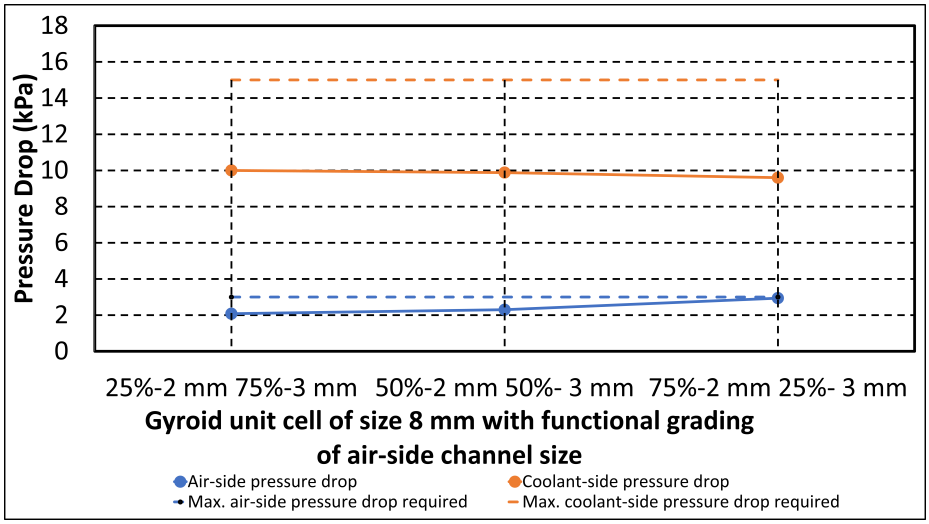

Figure 4.10: Area averaged pressure drop for air-side and coolant-side channels varying with functional grading in gyroid unit cell length along air-side

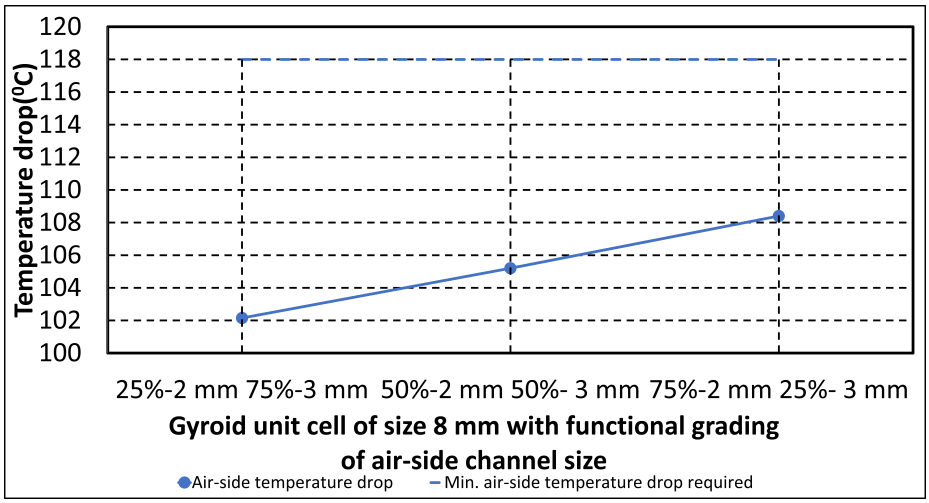

Figure 4.11: Area averaged temperature drop for air-side channel varying with functional grading in gyroid unit cell length along air-side

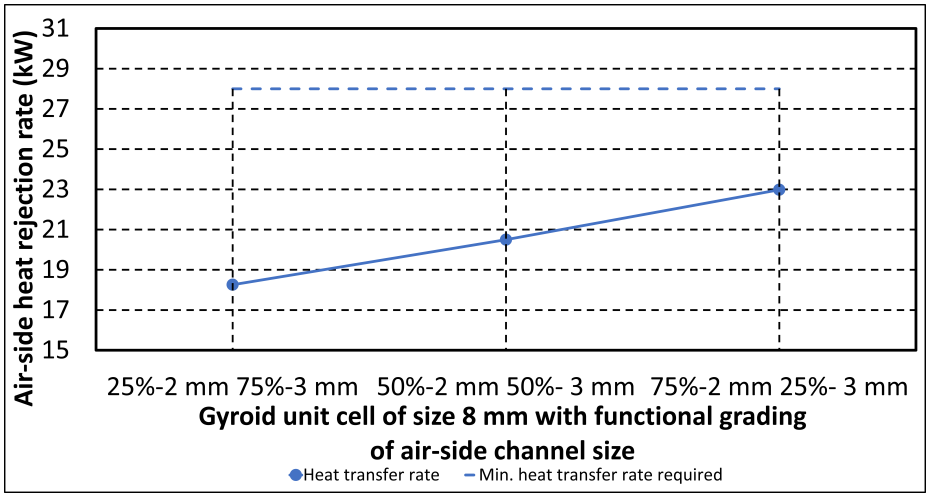

Figure 4.12: Heat rejection rate for air-side channel varying with functional grading in gyroid unit cell length along air-side

4.1.5 Cumulative effect

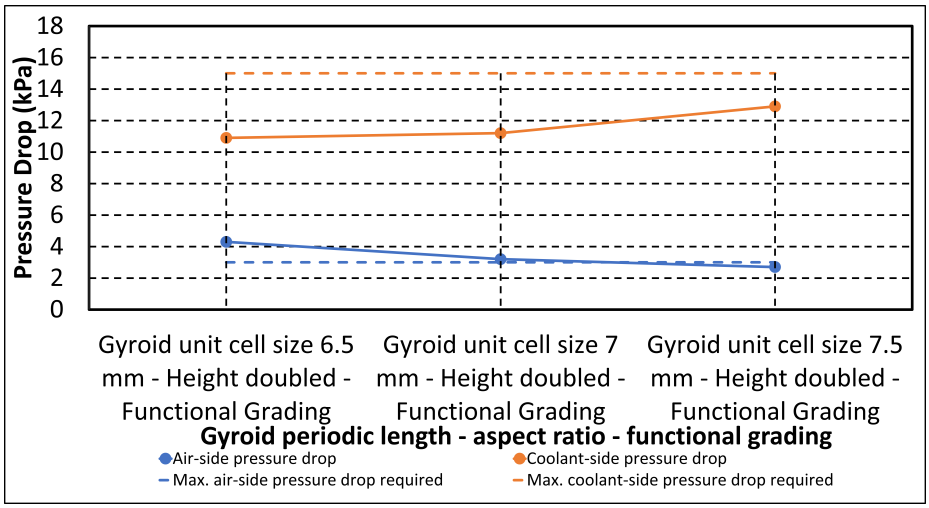

Figure 4.13: Area averaged pressure drop for air-side and coolant-side channels varying with both functional grading and doubling gyroid unit cell length along air-side

Every parameter analyzed previously affected both pressure drop and temperature drop in a certain way. Therefore, a combined effect of all previously studied parameters can help to optimize heat exchanger design. Figure 4.13 shows pressure drop variation on the air-side and coolant-side flow considering all parametric analysis summed in one model. It is observed that coolant-side pressure drop is well within limits for all cases whereas air-side pressure drop is within the limit with increasing unit cell size. Also, the calculated temperature drop and heat rejection rate on the air-side are close but lower than requirements, as shown in the figure 4.14 and the figure 4.15. This concludes that both pressure drop and temperature drop will have little deviation from required values. Therefore, targets are required to be reduced for the heat exchanger design. Furthermore, it is necessary to verify whether these design variations can be manufactured without any cracks, void, internal or external

failures.

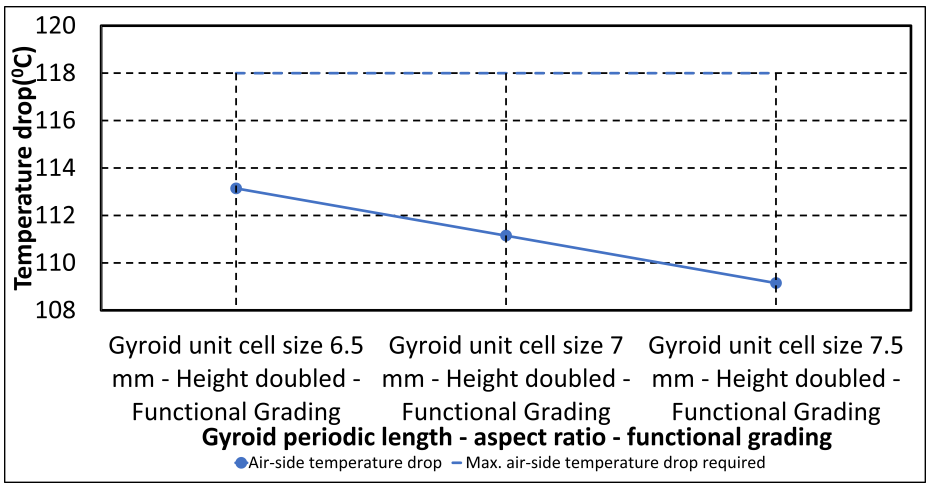

Figure 4.14: Area averaged temperature drop for air-side channel varying with both functional grading and doubling gyroid unit cell length along air-side

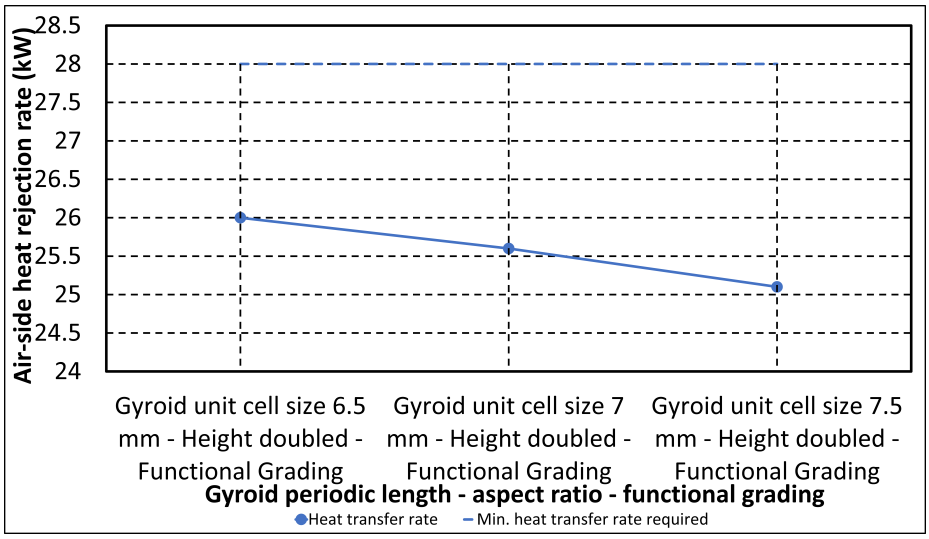

Figure 4.15: Heat rejection rate for air-side channel varying with both functional grading and doubling gyroid unit cell length along air-side

4.2 Manufacturability

Although parametric analysis using CFD resulted in heat exchanger core design with gyroid TPMS infill having output closest to design requirements, it was crucial to determine whether they could be printed. To probe its print-ability, 26 samples were prepared and printed using an optimized set of process parameters for LPBF of AlSi10Mg. These samples were studied externally and internally (using optical microscopy). Three gyroid-based prototypes were designed and fabricated among successfully printed samples & considering trends from CFD results. Details of this manufacturability study are explained in this section.

4.2.1 Printed samples based on parametric study

Figure 4.16 shows printed samples based on the parametric analysis. Samples were printed successfully and ensured the ability to print design variations in two orientations unaccompanied by internal support. It also encouraged printing prototypes and a full-scale heat exchanger design with gyroid core in different orientations, as per demand, in the absence of internal support. Moreover, it verified process parameters used for LPBF of AlSi10Mg capable of printing without any external failures from visual observation. Gyroid samples with orientation rotated 90° with respect to the original set of samples did not cause any visible defects, but it is expected to affect surface roughness and dimensional accuracy. Therefore, before printing prototypes or full-scale designs, it is crucial to investigate internal build quality, which can't be observed from visual inspection.

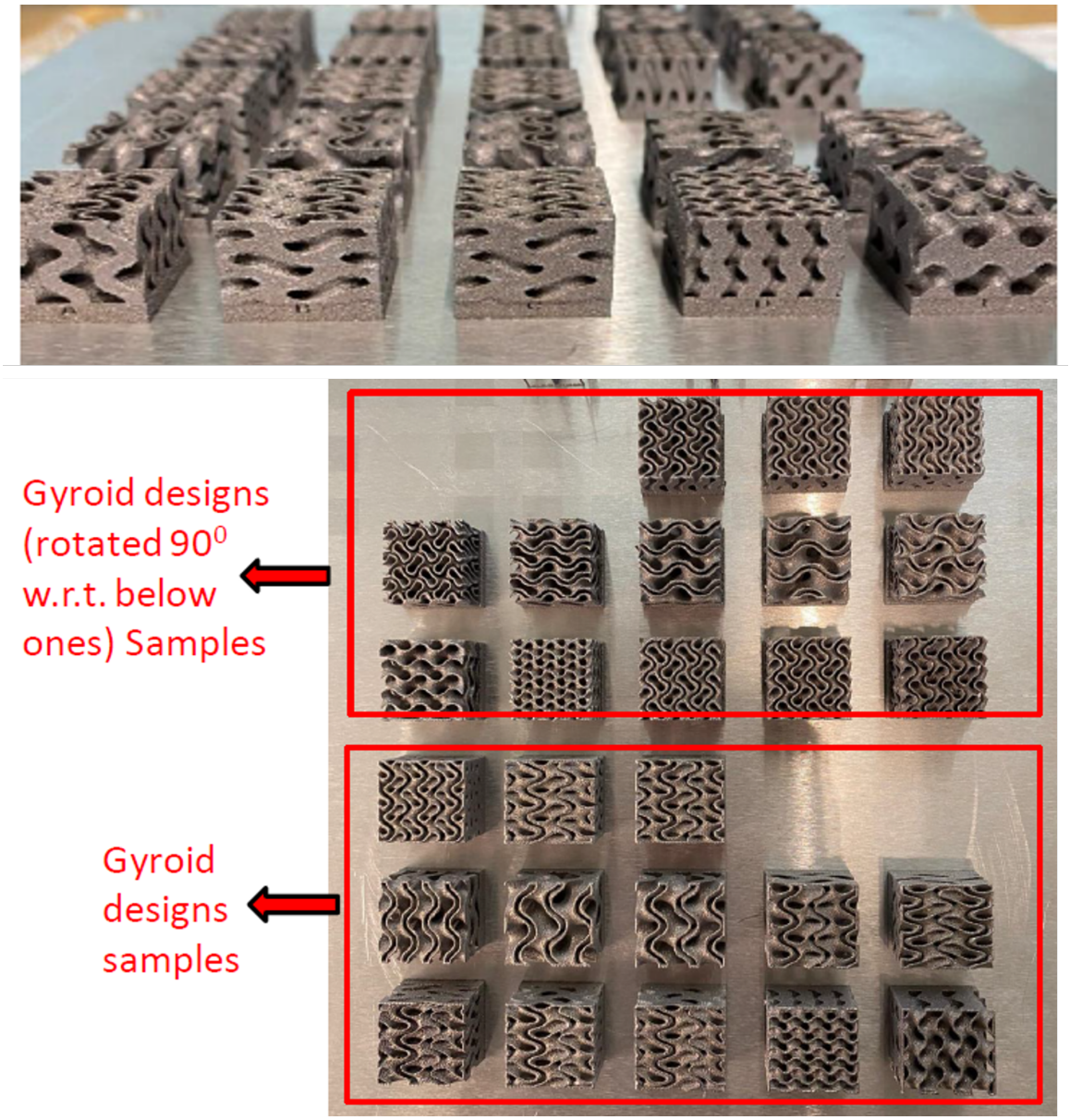

Figure 4.16: Printed samples on build plate from EOS M280

4.2.2 Optical Microscopy

Gyroid samples obtained after printing did not exhibit any failure or defect from outside. It was necessary to check the internal build of samples because the gyroid walls separating fluids in the heat exchanger core should be non-porous (to avoid mixing of both flowing fluids) and exhibit enough strength to sustain under fluid pressures. Thus, cut-sections of the samples were observed under an optical microscope. Samples were cut using a precision cutter, and smaller parts of the samples were dipped in an epoxy solution to get coupons. Coupons were ground and polished, which enabled them to observe under optical microscopy. Figures 4.17, 4.18, 4.19 & 4.20 show optical microscopy images of samples A, B, D & G. Table 4.1 summarizes observations from microscopy images of the samples. It can be observed that there is an inconsistent build layer and broken struts due to the minimal strut size of 0.2 mm in sample A. Therefore, wall thickness is recommended to be not less than 0.5 mm. This analysis concludes that gyroid samples with functional grading are not feasible for building prototypes because the wall thickness should be at least 0.2 mm to realize the coolant-side channel. Hence, considering trends in CFD results from the parametric analysis, three prototypes with unit cell sizes of (7, 7, 10), (7, 7, 14), and (12, 12, 14) were selected for manufacturing.

Table 4.1: Summary on build information of samples

Sample	Discontinuous melt track	Complete melting
A	✓	✗
B	✗	✓
D	✗	✓
G	✗	✓

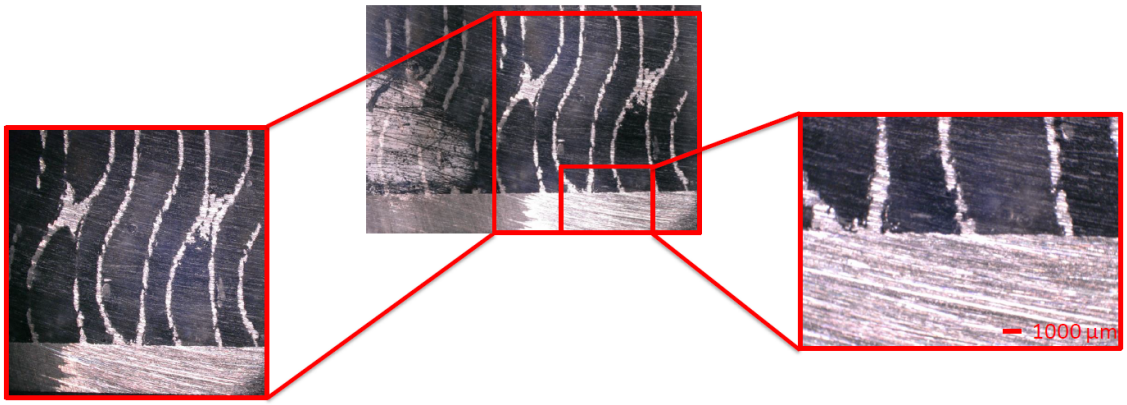

Figure 4.17: Images from optical microscopy of sample A

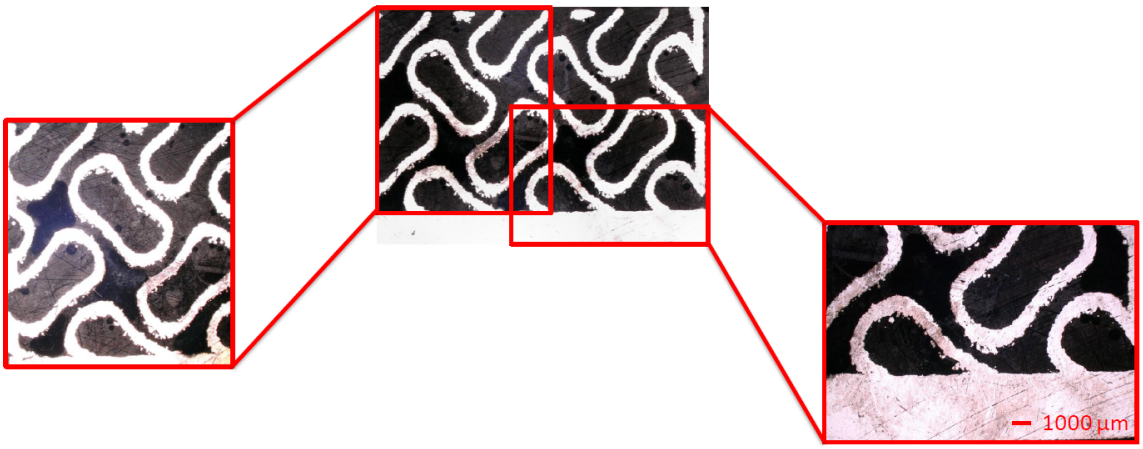

Figure 4.18: Images from optical microscopy of sample B

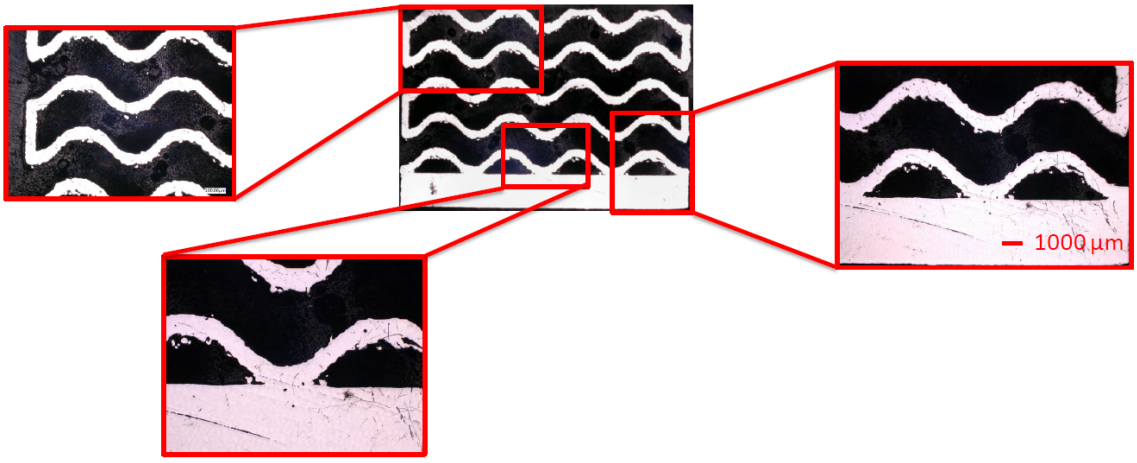

Figure 4.19: Images from optical microscopy of sample D

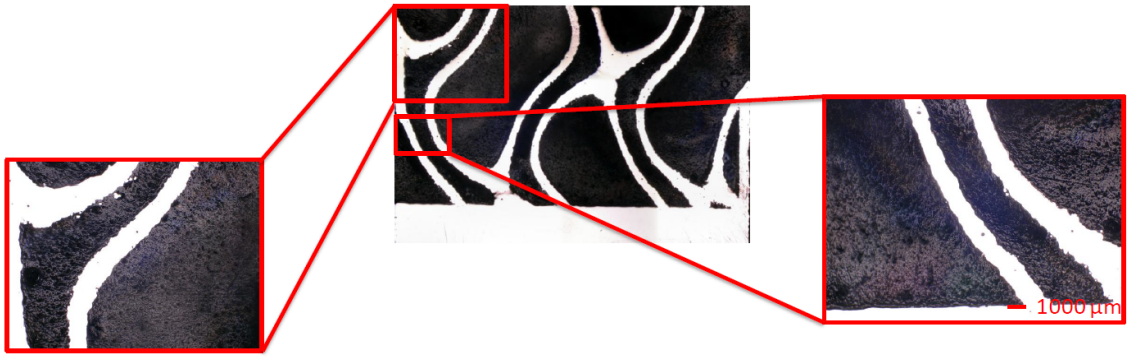

Figure 4.20: Images from optical microscopy of sample G

4.2.3 Printed prototypes

Figure 4.21, 4.22, 4.23, 4.24 & 4.26 shows prototypes printed with gyroid infill as heat exchanger core. Gyroid designs were filtered based on thermal performance from CFD analysis and AM build integrity of the samples. As mentioned previously, all prototypes could not fit in the space available in EOS M280. Therefore the prototypes were manufactured in EOS M290 with the same set of optimized process parameters as given in Table 3.4. To check build integrity and impermeability, running water

was passed from inlet to outlet on the coolant-side and the air-side of the prototypes. There were no signs of leakage, void, or crack in all prototypes.

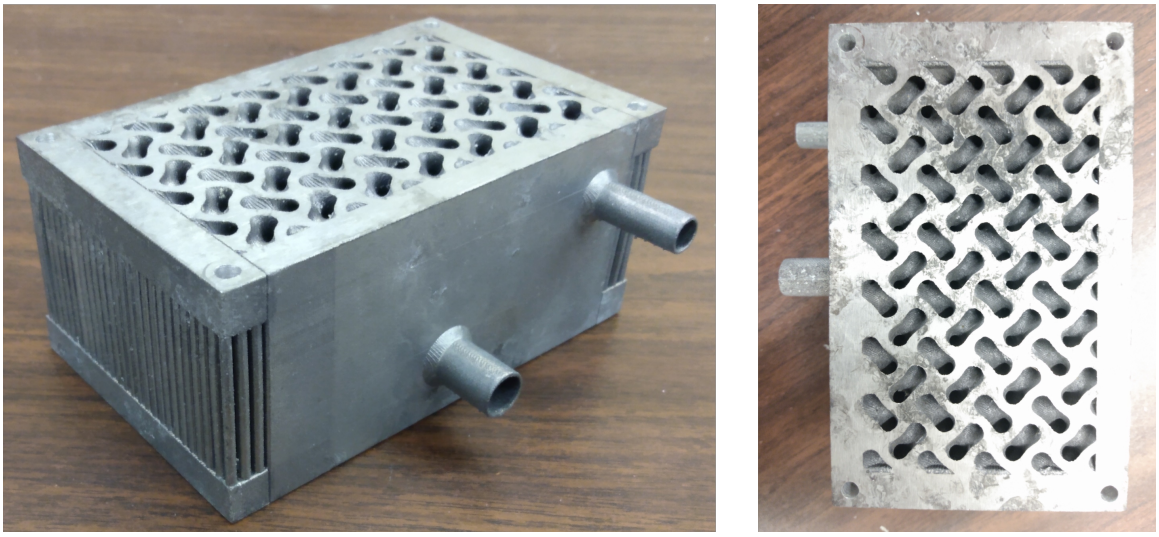

Figure 4.21: Printed prototype with gyroid core of unit cell size (12, 12, 14)

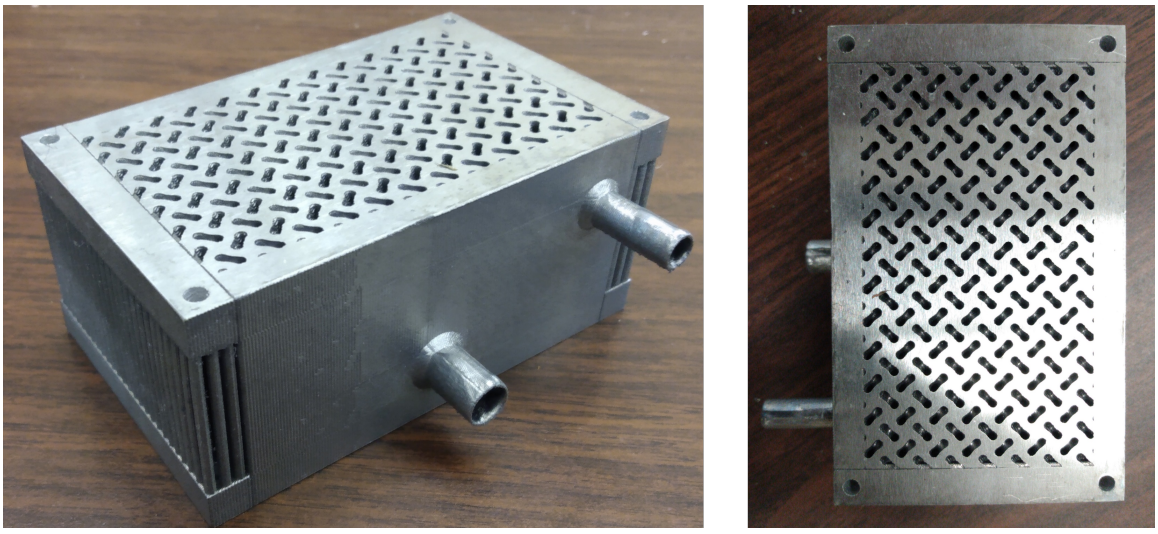

Figure 4.22: Printed prototype with gyroid core of unit cell size (7, 7, 14) with inlet and outlet on same side

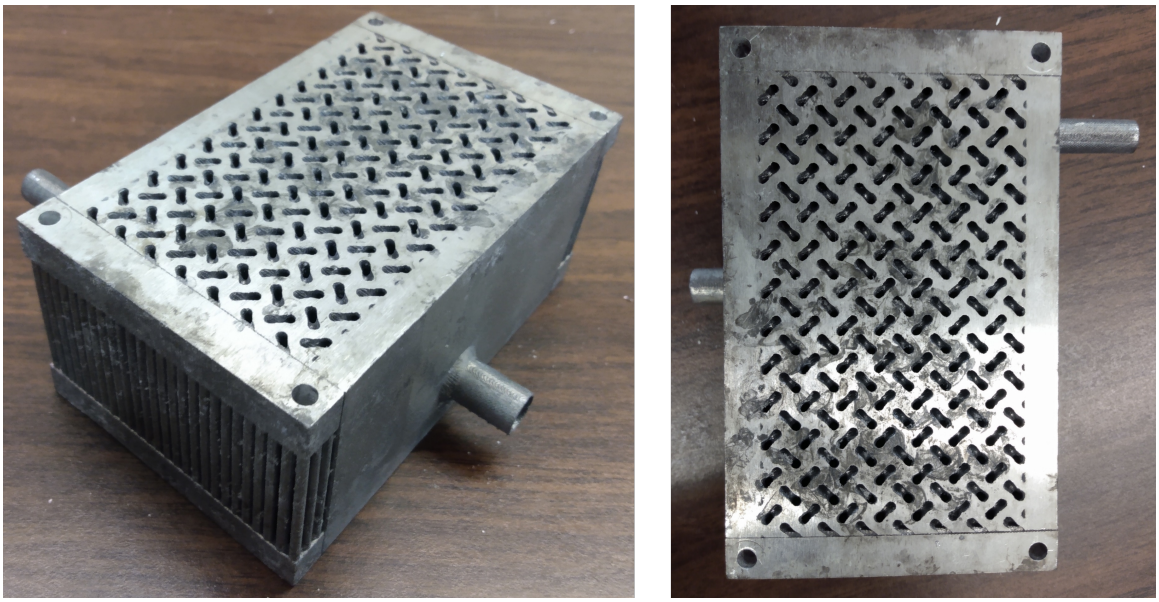

Figure 4.23: Printed prototype with gyroid core of unit cell size (7, 7, 14) with inlet and outlet on opposite sides

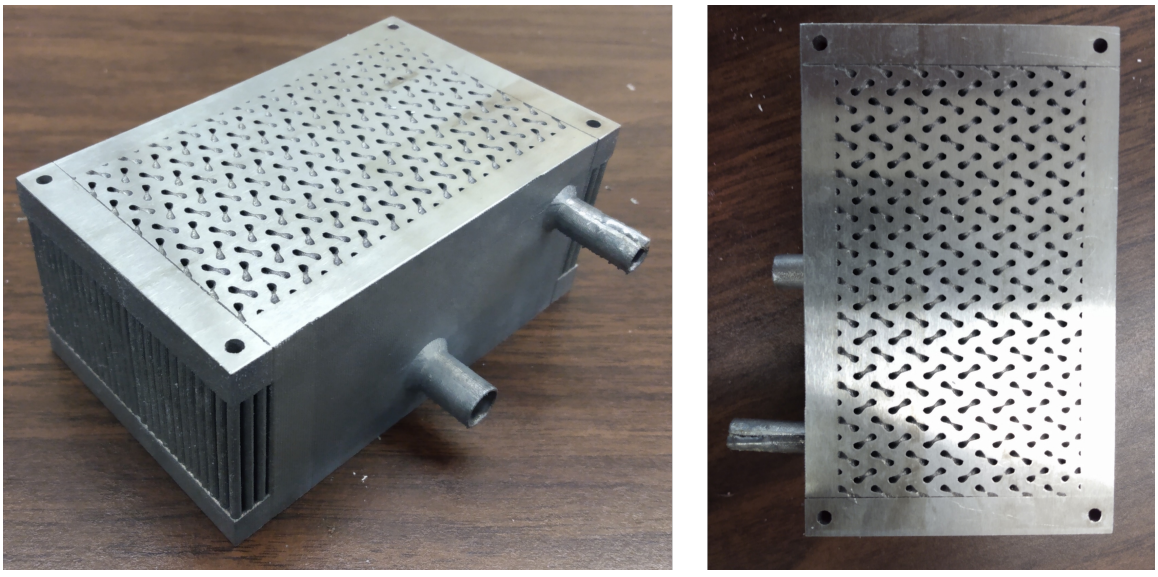

Figure 4.24: Printed prototype with gyroid core of unit cell size (7, 7, 10)

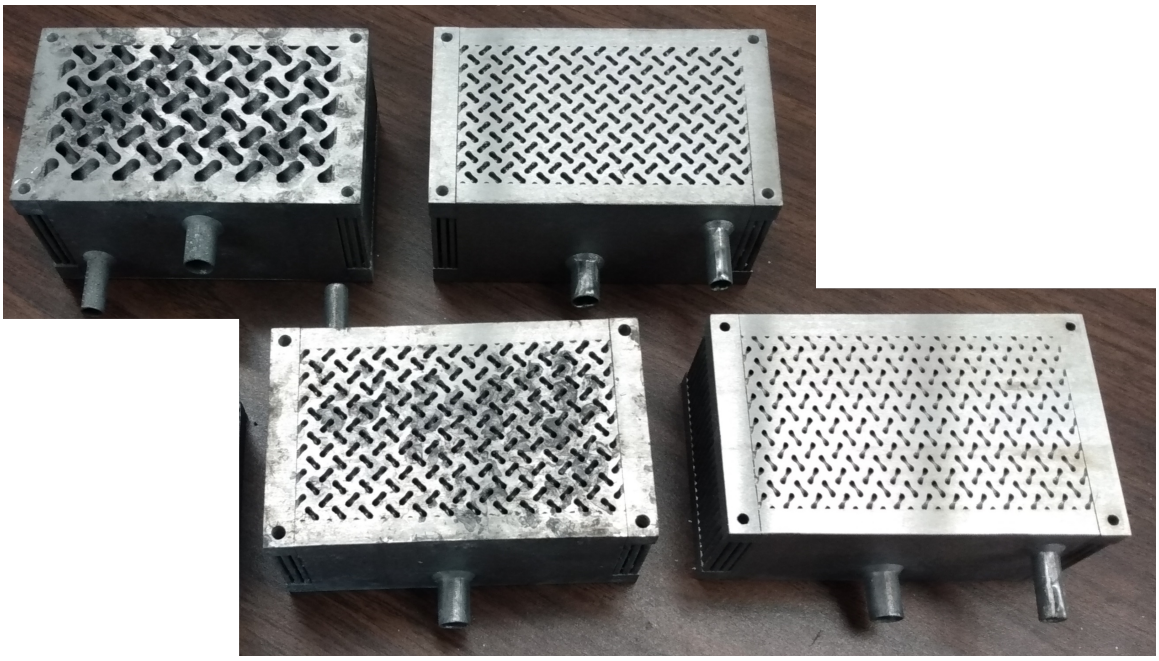

Figure 4.25: All printed prototypes

4.3 Comparison with conventional design

Comparison based on thermal performance and weight of the printed prototypes was studied between a conventional shell-and-tube heat exchanger design & gyroid-based heat exchanger design with the same material and set of process parameters as mentioned in Table 3.4. First, the tubes were initiated with a circular shape. Then, with several design iterations to optimize as per given boundary conditions, they were modified to ellipsoidal shape with a semi-major axis length of 3.5 mm and semi-minor axis length of 1.5 mm. Tube wall thickness was assumed to be 0.5 mm. The thermal performance comparison is based on CFD analysis, whereas a digital weighing machine was used to weight printed prototypes. Figure 4.27 shows a comparison of heat rejection rate on the air-side between optimal results obtained

from gyroid-based heat exchanger core and shell-and-tube design heat exchanger core. The comparison clearly states that the shell-and-tube design has 18.96% less heat rejection than the optimized gyroid-based design for same mass-flow rate and within pressure drop limits. The AM build for the shell-and-tube design had no defects or failures. Figure 4.27 also compares the weight of different prototypes, and it is observed that prototypes with gyroid unit cell size (7, 7, 10), (7, 7, 14), and (12, 12, 14) have a weight reduction of 11.19%, 14.8%, and 20.21% respectively as compared to conventional shell-and-tube design.

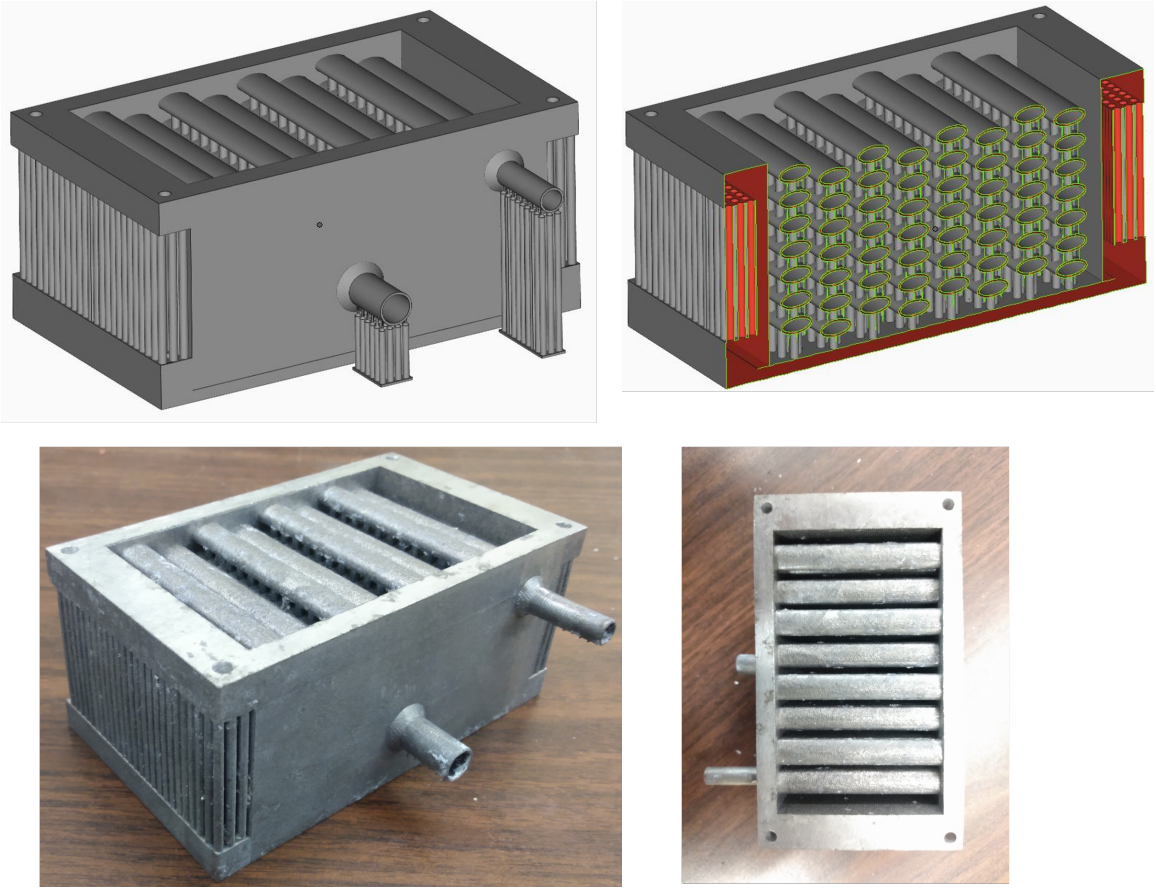

Figure 4.26: Model and printed prototype of shell-and-tube design

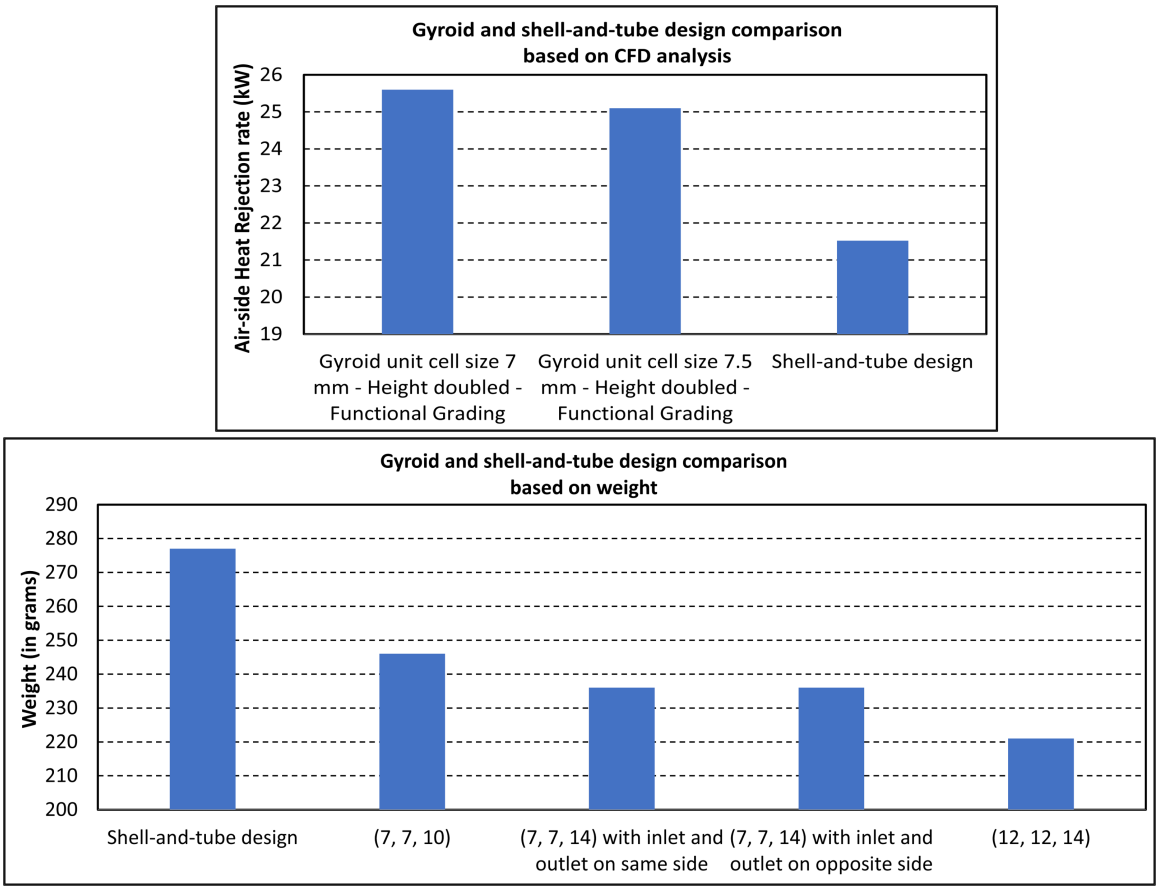

Figure 4.27: Comparison of thermal performance and weight between gyroid design and shell-and-tube design

4.4 Discussion

Results obtained from CFD analysis validate different gyroid unit cell variations approaches to meet heat exchanger design requirements. More design variations approaches can be explored, and field-driven optimization can be used to enhance thermal performance. To further improve the thermal performance of the heat exchanger, the thermal conductivity of heat exchanger material plays an important role. Thus,

either the thermal conductivity of existing material can be increased, or more materials with higher thermal conductivity can be explored. Thermal conductivity of AlSi10Mg is 119 $\pm$ 5 $\frac{W}{mK}$ in the build direction & 103 $\pm$ 5 $\frac{W}{mK}$ in the transverse direction and can be increased up to 173 $\pm$ 10 $\frac{W}{mK}$ after heat treatment [84], whereas thermal conductivity of printed pure copper using LPBF is recorded to be 360 $\frac{W}{mK}$ [85]. Pure copper can be printed with a bulk density of nearly 99% [85]. Walls of the heat exchanger core with thickness as low as 0.2 mm can be printed with advanced knowledge in LPBF machine settings. Lower wall thickness implies lower resistance to heat transfer and thus, there will be an increment in thermal performance.

Chapter 5

Conclusion

The research attempted to design for additive manufacturing of an automotive heat exchanger, i.e., WCAC, within design constraints to achieve specific target performance requirements. In the pursuit of DfAM of an advanced heat exchanger, the following objectives were achieved:

1. Complex structures such as TPMS can be quickly and precisely represented as implicit models & can be designed for heat exchangers applications. In addition, implicit models were converted into computational models for analysis to obtain thermo-fluid dynamic characteristics.
2. A parametric study and analysis considering gyroid TPMS as heat exchanger core design enabled design optimization to meet the thermal performance requirements. Parametric study and analysis were based on gyroid network type (solid and sheet), periodic length, sheet thickness, wall thickness, aspect ratio, and functional grading. Each parameter affected thermo-fluid dynamic characteristics in specific ways, and the goal was to develop an optimal design meeting

required performance.

3. Characterization of AM allowed to assess internal AM build to attain high-density & build integrity and avoid porosity, defect, or failure. It also helped validate LPBF process parameters that were used for AlSi10Mg.
4. Designing and printing prototypes of heat exchangers based on the microscopic assessment of AM build and CFD analysis.
5. Comparison between additively manufactured gyroid-based design and conventional & optimized shell-and-tube type design showed an increase of 18.96% in thermal performance from CFD analysis and a weight reduction of 14.8% for the gyroid-based design as compared to the shell-and-tube design.

There is further scope of improvements under this study such as:

1. Improving meshing capabilities for modeling & analysis and getting sharp geometry for AM and print parts with greater dimensional accuracy.
2. Including structural analysis, surface roughness, etc. to realize and improve design requirements, which were out-of-scope in this study
3. Integration of air-side inlet and outlet manifolds with the core design and analyzing effects of the manifold on thermal and flow field characteristics

Chapter 6

Future Work

Designing heat exchangers with TPMS lattice structures has opened new avenues in design, material, and additive manufacturing & can be studied individually in detail. As a part of this research, printed prototypes can be further tested for thermal performance with an experimental setup. Figure 6.1 shows a schematic of the experimental design for heat exchanger prototypes testing.

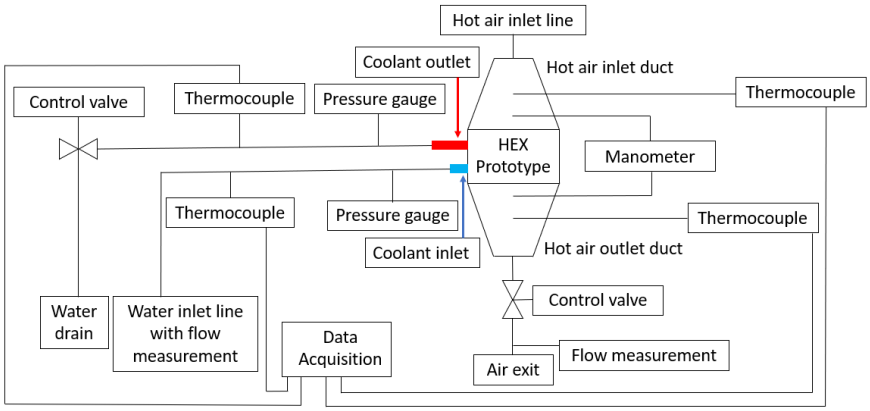

Figure 6.1: Schematic of the experimental setup

The schematic shows that hot air will enter the heat exchanger prototype from a gradually increasing duct. The length of ducts should be ten times the hydraulic diameter of the air-side entrance to establish a developed flow. Thermocouples and pressure measuring devices will be installed at the inlet and outlet of both the hot and cold sides to record temperature difference and pressure drop. The temperature difference and pressure drop readings recorded from experiments will be then validated with the CFD results of the prototype model. This process will infer with the final design for the full-scale model. A possible build orientation for LPBF needs to be planned to avoid failure considering available build volume. The same experimental setup used for the prototype will be extended for a full-scale model and, finally, can be tested for running it in an existing automotive system.

Appendix A

Design to CFD analysis workflow & Mesh/Grid independence study

Design to CFD analysis workflow

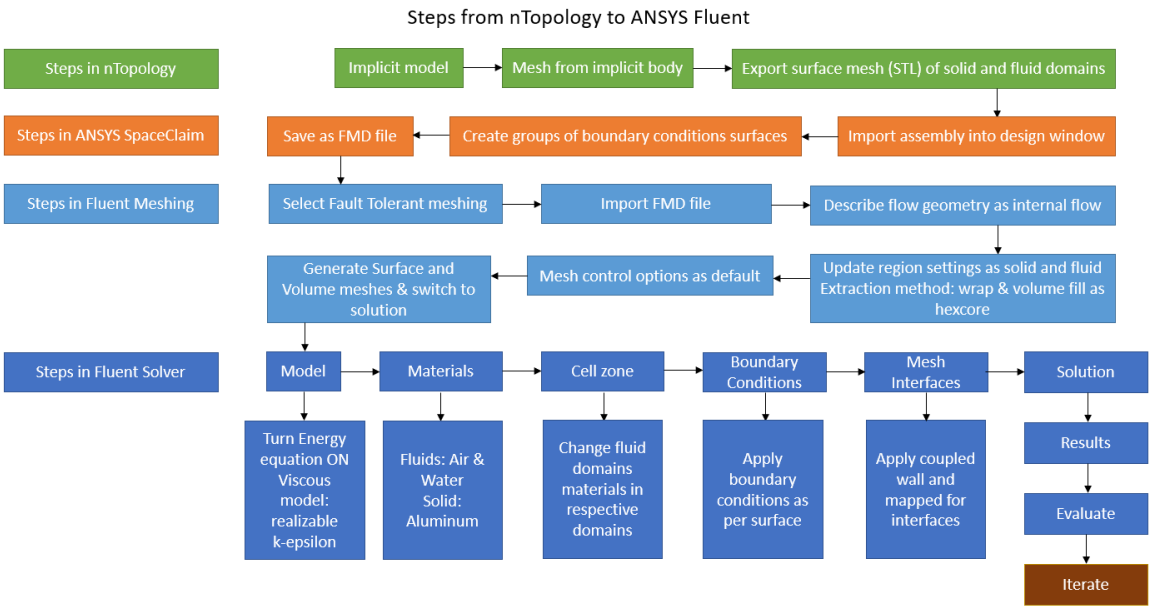

Figure A.1: Workflow from nTopology to ANSYS Fluent for analysis

Mesh/Grid independence study

A mesh/grid independence study was done to observe changes in area-averaged outlet temperature with respect to decreasing element size in the mesh by refining mesh. This was done in Fault Tolerant Meshing (FTM) module of Fluent Meshing (previously known as ANSYS T-Grid) by decreasing maximum element size from 3 mm to 1 mm in the period 0.5 mm in five steps while keeping minimum cell size constant to be 0.5 mm. Results showed independence of element size with area-averaged outlet temperature as plotted on the graph in the figure A.2.

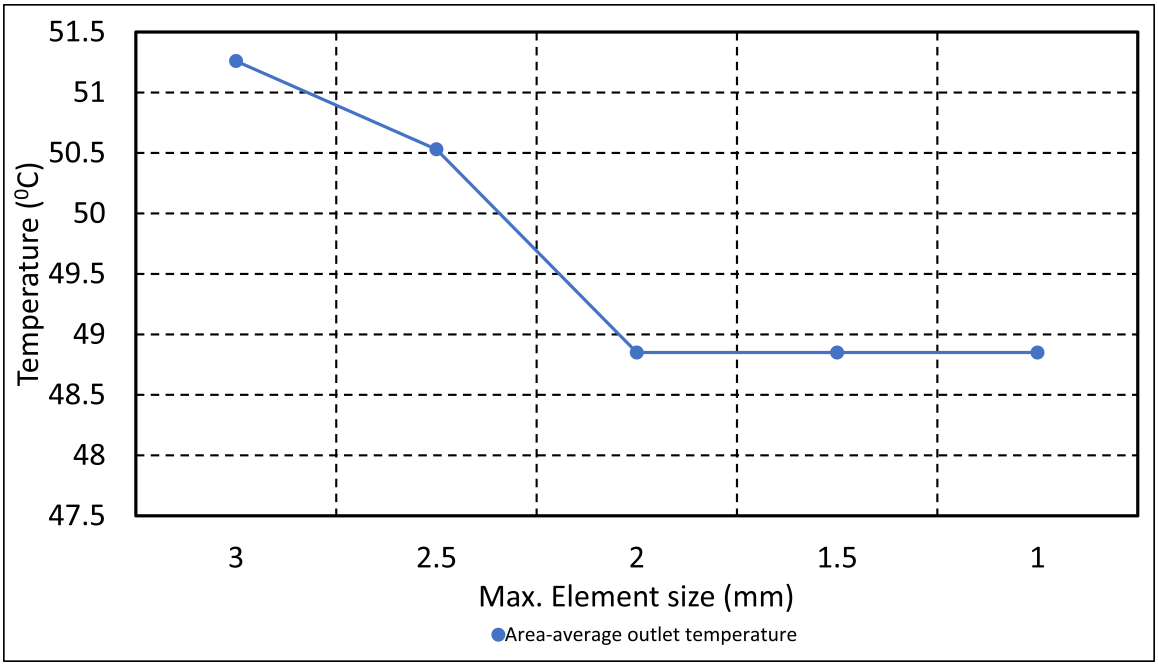

Figure A.2: Mesh sensitivity analysis using area-averaged outlet temperature variation

Appendix B

File preparation and printing process

File preparation

Figure B.1: Process to create file for printing

Materialize Magics

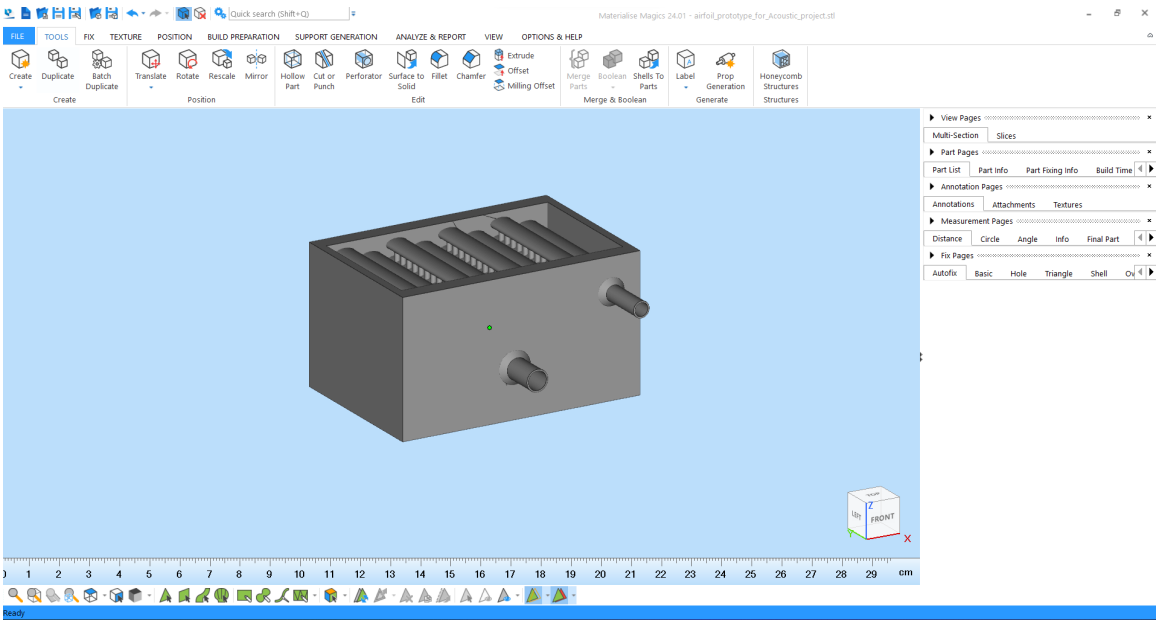

Figure B.2: Interface of Materialise Magics

- Import STL file of the part
- Set the printer
- Place parts as required on the build plate
- Generate supports (if required)
- Set layer thickness
- Save parts as STL files format and supports as CLI files format

RP Tools

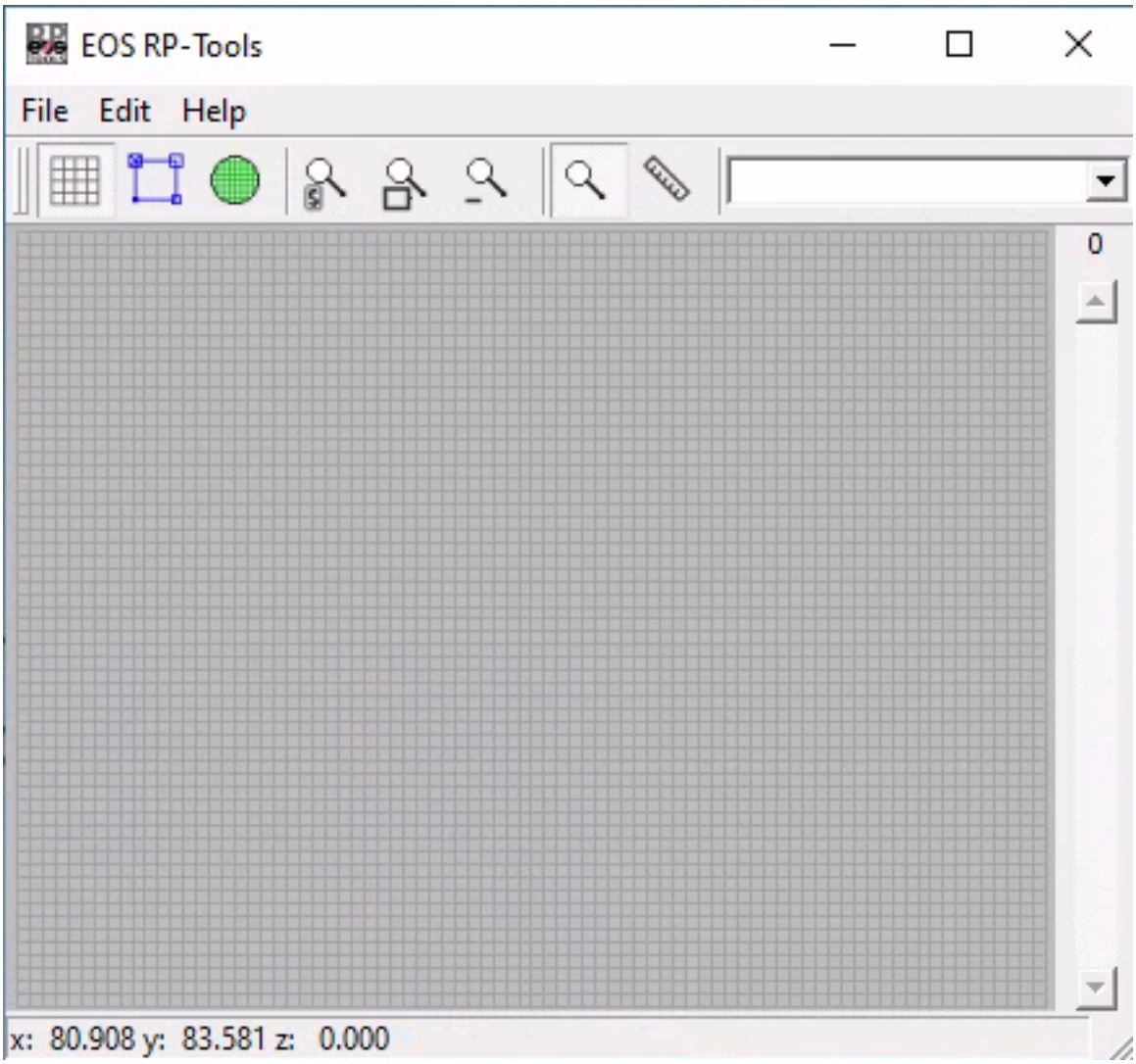

Figure B.3: Interface of RP Tools

Import part from Materialise Magics to RP Tools. It divides part into user-defined height for slices/layers

PSW

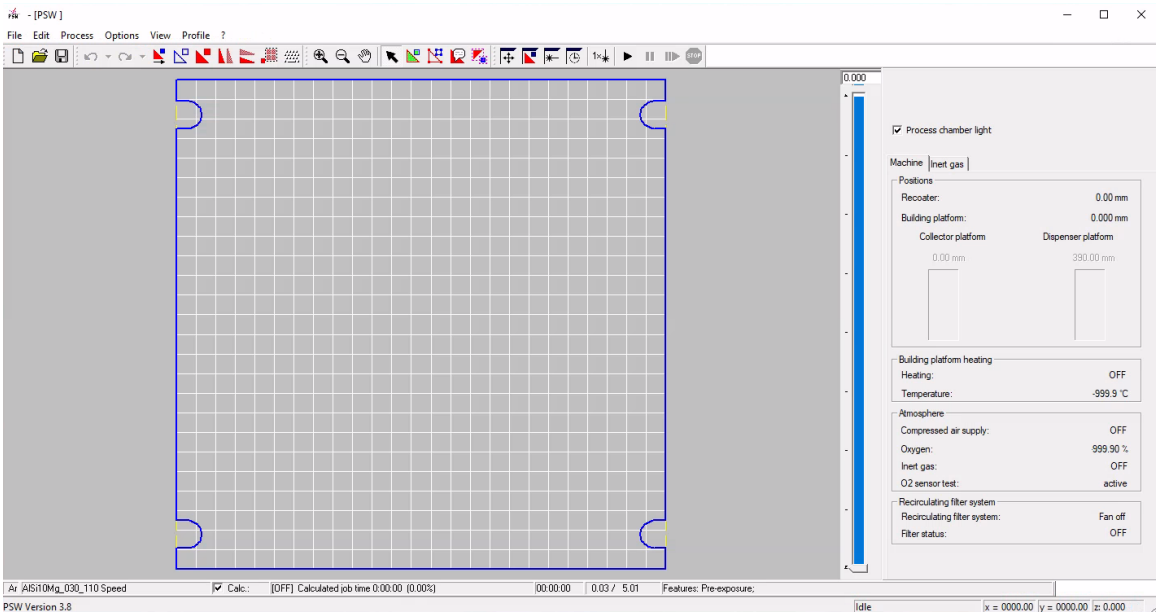

Figure B.4: Main interface of PSW Tools

- Check for light inside build chamber
- Check for circulation of inert gas inside build chamber
- Move/duplicate parts
- Check for hatch lines
- Calculate and check for printing time

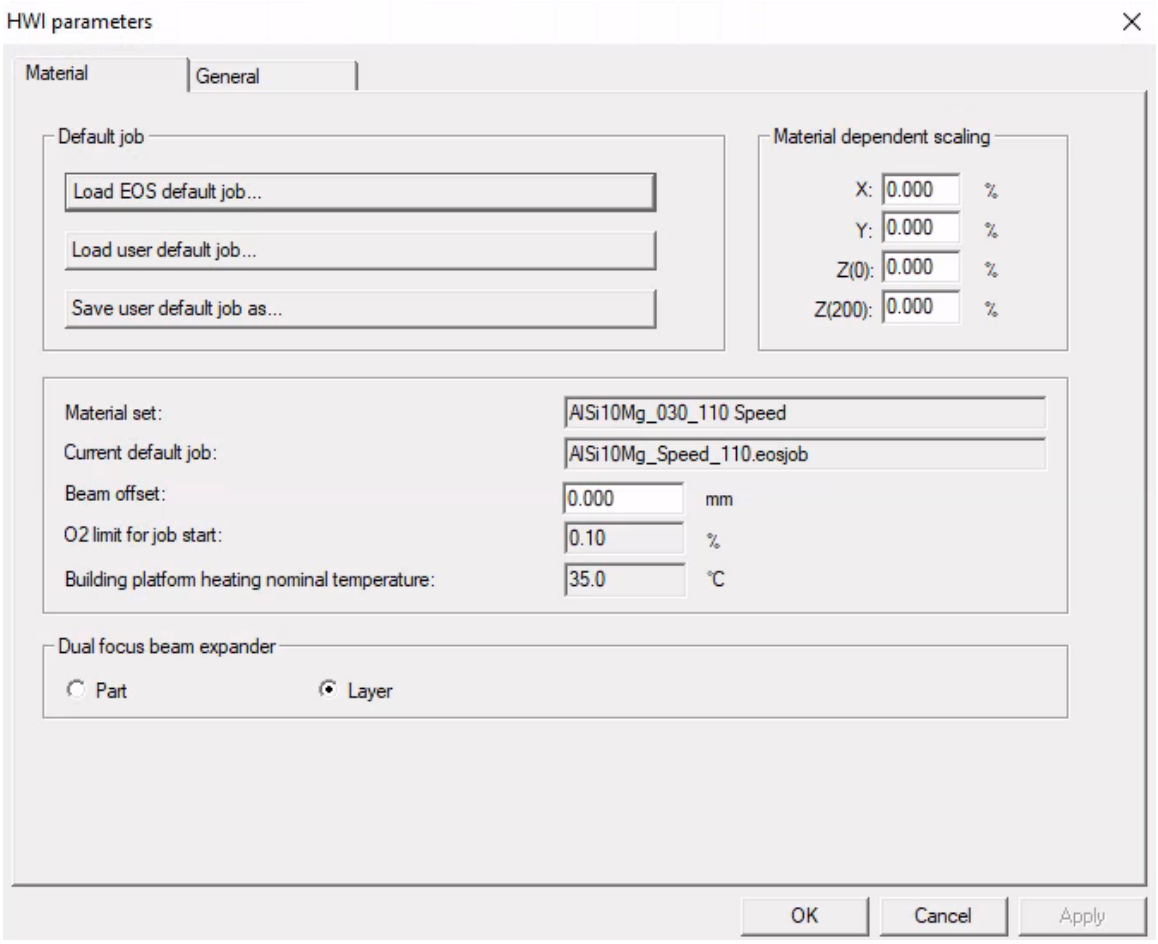

Figure B.5: PSW parameter settings

- Check material parameter set
- Calibrate laser as per X Y Z axis

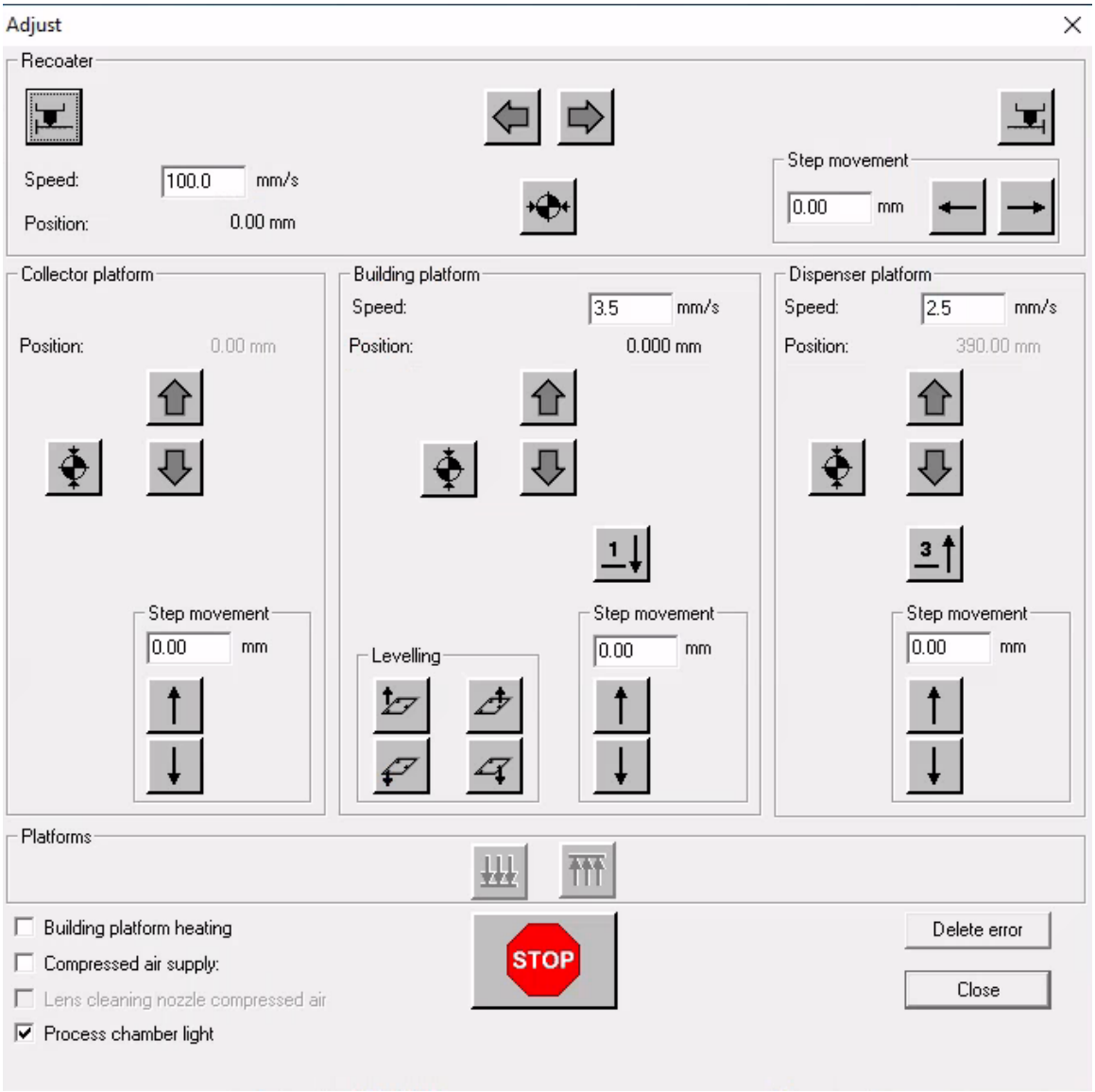

Figure B.6: PSW adjust window

- Move recoater from left to right
- Homing recoater
- Check for heating of build plate

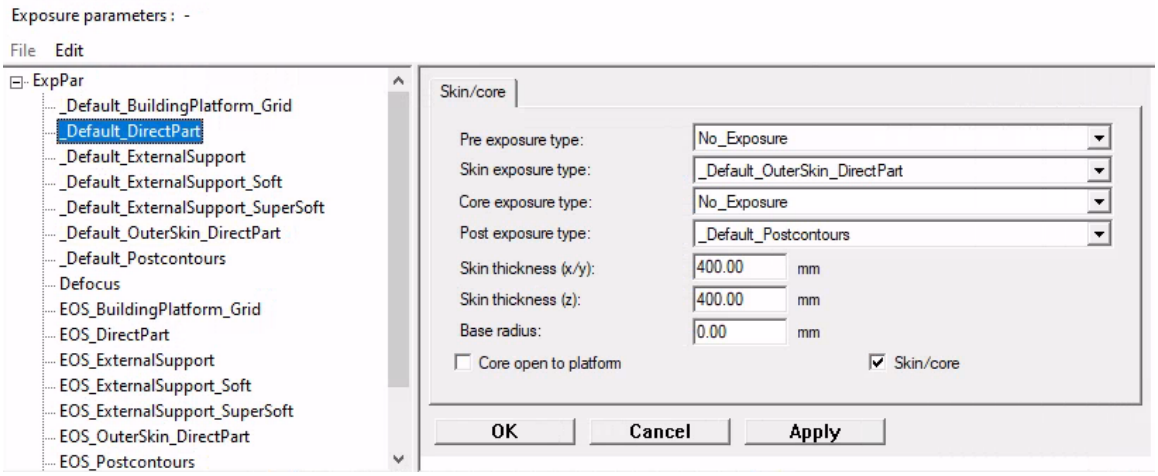

Figure B.7: PSW exposure parameter setting

- Check type of exposure parameter
- Change height of powder layer
- Change percentage of powder dosage that will be spreaded on build plate by recoater

EOS M280

Figure B.8: EOS M280

Bibliography

[1] ISO/ASTM. Additive Manufacturing - General Principles Terminology (ASTM52900). *Rapid Manufacturing Association*, pages 10–12, 2013.

[2] D. T. Pham and R. S. Gault. A comparison of rapid prototyping technologies. *International Journal of Machine Tools and Manufacture*, 38(10-11):1257–1287, 1998.

[3] Tharanath Tharanath. Investigating the design workflow for designing a component for Additive Manufacturing A case study of designing a jet engine combustion chamber component for AM. 2020.

[4] T. T. W. Gornet. History of Additive Manufacturing. pages 1–24, 2017.

[5] Charles W Hull. Apparatus for production of three-dimensional objects by stereolithography. *Patent*, (19):16, 1984.

[6] M K Thompson, G ; Moroni, T ; Vaneker, G ; Fadel, R I Campbell, I ; Gibson, A ; Bernard, J ; Schulz, P ; Graf, B Ahuja, and F Martina. Design for Additive Manufacturing: Trends, opportunities, considerations, and constraints. C I R P Annals. *CIRP Annals-Manufacturing Technology*, 65(2):737–760, 2016.

[7] J Giannatsis and V Dedoussis. Additive fabrication technologies applied to medicine and health care: a review. 2007.

[8] Charles L. Thomas, Thomas M. Gaffney, Srinivas Kaza, and Cheol H. Lee. Rapid prototyping of large scale aerospace structures. *undefined*, 4:219–229, 1996.

[9] Yuhua Song, Yongnian Yan, Renji Zhang, Da Xu, and Feng Wang. Manufacture of the die of an automobile deck part based on rapid prototyping and rapid tooling technology. 2001.

[10] Angelica Lindwall, Christo Dordlofva, Anna Öhrwall Rönnbäck, et al. Additive manufacturing and the product development process: Insights from the space industry. In *DS 87-5 Proceedings of the 21st International Conference on Engineering Design (ICED 17) Vol 5: Design for X, Design to X, Vancouver, Canada, 21-25.08. 2017*, pages 345–354, 2017.

[11] Inderjot Kaur and Prashant Singh. State-of-the-art in heat exchanger additive manufacturing. *International Journal of Heat and Mass Transfer*, 178:121600, 2021.

[12] Geoffrey Boothroyd, Peter Dewhurst, and Winston A Knight. *Product design for manufacture and assembly*. CRC press, 2010.

[13] Floriane Laverne, Frédéric Segonds, Nabil Anwer, and Marc Le Coq. Dfam in the design process: A proposal of classification to foster early design stages. 2014.

[14] Abdullah Alfaify, Mustafa Saleh, Fawaz M. Abdullah, and Abdulrahman M. Al-Ahmari. Design for additive manufacturing: A systematic review. *Sustainability (Switzerland)*, 12(19), 2020.

[15] J. N. Devi Sankar and P. S. Kishore. Thermal Analysis of Water Cooled Charge Air Cooler in Turbo Charged Diesel Engine. *International Journal of Research in Engineering and Technology*, 05(02):193–197, 2016.

[16] Ravindra D. Kapse and Dr. R. R. Arakerimath. Study and Comparison of Charge Air Cooling Techniques their Effects on Efficiency of Automobile Engine. *International Journal of Engineering Research and*, V6(07):196–201, 2017.

[17] Masaki Harada, Takashi Yasuda, Shota Terachi, Sergio Pujols, and Jason R. Spenny. Water Cooled Charge Air Cooler Development. *SAE Technical Papers*, pages 1–5, 2016.

[18] Water to Air Vs Air to Air Intercooler — intercooler air water FMIC.

[19] Olaf Diegel, Axel Nordin, and Damien Motte. *A Practical Guide to Design for Additive Manufacturing*. Springer, 2019.

[20] Ian Gibson, David W Rosen, Brent Stucker, and Mahyar Khorasani. *Additive manufacturing technologies*, volume 17. Springer, 2021.

[21] William E Frazier. Metal additive manufacturing: a review. *Journal of Materials Engineering and performance*, 23(6):1917–1928, 2014.

[22] Ben Redwood, Filemon Schöffer, and Brian Garret. *The 3D printing handbook: technologies, design and applications*. 3D Hubs, 2017.

[23] Joamin Gonzalez-Gutierrez, Santiago Cano, Stephan Schuschnigg, Christian Kukla, Janak Sapkota, and Clemens Holzer. Additive manufacturing of metallic and ceramic components by the material extrusion of highly-filled polymers: A review and future perspectives. *Materials*, 11(5):840, 2018.

[24] Brian N Turner, Robert Strong, and Scott A Gold. A review of melt extrusion additive manufacturing processes: I. process design and modeling. *Rapid Prototyping Journal*, 2014.

[25] Wenchao Du, Xiaorui Ren, Chao Ma, and Zhijian Pei. Binder jetting additive manufacturing of ceramics: A literature review. In *ASME International Mechanical Engineering Congress and Exposition*, volume 58493, page V014T07A006. American Society of Mechanical Engineers, 2017.

[26] Igor Yadroitsev, Ina Yadroitsava, and Anton Du Plessis. Basics of laser powder bed fusion. In *Fundamentals of Laser Powder Bed Fusion of Metals*, pages 15–38. Elsevier, 2021.

[27] Syed AM Tofail, Elias P Koumoulos, Amit Bandyopadhyay, Susmita Bose, Lisa O'Donoghue, and Costas Charitidis. Additive manufacturing: scientific and technological challenges, market uptake and opportunities. *Materials today*, 21(1):22–37, 2018.

[28] O. Rehme, C. Emmelmann, and Wissenschaftliche Gesellschaft fur Lasertechnik. *Reproducibility for properties of selective laser melting products*. AT-Verlag, 2005.

[29] Paul O'Regan, Paul Prickett, Rossi Setchi, Gareth Hankins, and Nick Jones. Metal based additive layer manufacturing: variations, correlations and process control. *Procedia Computer Science*, 96:216–224, 2016.

[30] Theodore L Bergman, Frank P Incropera, David P DeWitt, and Adrienne S Lavine. *Fundamentals of heat and mass transfer*. John Wiley & Sons, 2011.

[31] Cuneyt Ezgi. Basic design methods of heat exchanger. In *Heat Exchangers-Design, Experiment and Simulation*. IntechOpen, 2017.

[32] Davoud Jafari and Wessel W Wits. The utilization of selective laser melting technology on heat transfer devices for thermal energy conversion applications: A review. *Renewable and Sustainable Energy Reviews*, 91:420–442, 2018.

[33] Ercan M Dede, Shailesh N Joshi, and Feng Zhou. Topology optimization, additive layer manufacturing, and experimental testing of an air-cooled heat sink. *Journal of Mechanical Design*, 137(11), 2015.

[34] Kathryn L Kirsch and Karen A Thole. Numerical optimization, characterization, and experimental investigation of additively manufactured communicating microchannels. *Journal of Turbomachinery*, 140(11):111003, 2018.

[35] Daniel Moreno Nieto and Daniel Moreno Sánchez. Design for additive manufacturing: Tool review and a case study. *Applied Sciences*, 11(4):1571, 2021.

[36] Harry Bikas, Panagiotis Stavropoulos, and George Chryssolouris. Additive manufacturing methods and modelling approaches: a critical review. *The International Journal of Advanced Manufacturing Technology*, 83(1-4):389–405, 2016.

[37] Ole Sigmund and Kurt Maute. Topology optimization approaches. *Structural and Multidisciplinary Optimization*, 48(6):1031–1055, 2013.

[38] Jerome Kaspar and Michael Vielhaber. Sustainable lightweight design–relevance and impact on the product development & lifecycle process. *Procedia Manufacturing*, 8:409–416, 2017.

[39] Pamela Waterman. 3 approaches to lightweighting - digital engineering 24/7. https://www.digitalengineering247.com/article/3-approaches-lightweighting/, 2015.

[40] Rafaela Vannutelli. *Mechanical behavior of 3D printed lattice-structured materials*. PhD thesis, 2017.

[41] Tobias A Schaedler and William B Carter. Architected cellular materials. *Annual Review of Materials Research*, 46:187–210, 2016.

[42] John O Milewski. Additive manufacturing of metals. *Cham: Springer International Publishing*, 2017.

[43] Aamer Nazir, Kalayu Mekonen Abate, Ajeet Kumar, and Jeng-Ywan Jeng. A state-of-the-art review on types, design, optimization, and additive manufacturing of cellular structures. *The International Journal of Advanced Manufacturing Technology*, 104(9):3489–3510, 2019.

[44] BK Nagesha, V Dhinakaran, M Varsha Shree, KP Manoj Kumar, Damodar Chalawadi, and T Sathish. Review on characterization and impacts of the lattice structure in additive manufacturing. *Materials Today: Proceedings*, 21:916–919, 2020.

[45] Torsten Schnabel, Markus Oettel, Bernhard Mueller, K Hoschke, A Pfaff, C Amund-Kopp, B Klöden, M Gebauer, and T Töppel. Design for additive manufacturing. *Guidelines and Case Studies for Metal Applications*, 2017.

[46] Tobias Maconachie, Martin Leary, Bill Lozanovski, Xuezhe Zhang, Ma Qian,

Omar Faruque, and Milan Brandt. Slm lattice structures: Properties, performance, applications and challenges. *Materials & Design*, 183:108137, 2019.

[47] Wahyudin P Syam, Wu Jianwei, Bo Zhao, Ian Maskery, Waiel Elmadih, and Richard Leach. Design and analysis of strut-based lattice structures for vibration isolation. *Precision Engineering*, 52:494–506, 2018.

[48] Hao Peng, Feng Gao, and Wenjing Hu. Design, modeling and characterization of triply periodic minimal surface heat exchangers with additive manufacturing. In *30th Annual International Solid Freeform Fabrication Symposium–An Additive Manufacturing Conference*, 2019.

[49] Inderjot Kaur and Prashant Singh. Flow and thermal transport characteristics of triply-periodic minimal surface (tpms)-based gyroid and schwarz-p cellular materials. *Numerical Heat Transfer, Part A: Applications*, 79(8):553–569, 2021.

[50] Kristel Michielsen and JS Kole. Photonic band gaps in materials with triply periodic surfaces and related tubular structures. *Physical Review B*, 68(11):115107, 2003.

[51] Giorgio Strano, L Hao, RM Everson, and KE Evans. A new approach to the design and optimisation of support structures in additive manufacturing. *The International Journal of Advanced Manufacturing Technology*, 66(9-12):1247–1254, 2013.

[52] Jeffrey K Liker, Mitchell Fleischer, and David Arnsdorf. Fulfilling the promises of cad. *MIT Sloan Management Review*, 33(3):74, 1992.

[53] Miguel Cerrolaza, Sandra Shefelbine, and Diego Garzón-Alvarado. *Numerical methods and advanced simulation in biomechanics and biological processes*. Academic Press, 2017.

[54] Martti Mäntylä. *An introduction to solid modeling*. Computer Science Press, Inc., 1987.

[55] Spatial Team DS. The main benefits and disadvantages of brep modeling. `https://blog.spatial.com/the-main-benefits-and-disadvantages-of-brep-modeling`, 2019.

[56] Lagnau Leslie. Implicit modelling for complex geometry. `https://www.3dcadworld.com/implicit-modelling-for-complex-geometry/`, 2020.

[57] Andrew Reitz. Implicits and fields for beginners. `https://ntopology.com/blog/2019/05/13/implicits-and-fields-for-beginners/`, 2019.

[58] George Allen. Whitepaper: ntopology modeling technology.

[59] Nicolas Huc. Conjugate heat transfer. `https://www.comsol.com/blogs/conjugate-heat-transfer/`, 2014.

[60] Bibin John, P Senthilkumar, and Sreeja Sadasivan. Applied and theoretical aspects of conjugate heat transfer analysis: a review. *Archives of Computational Methods in Engineering*, 26(2):475–489, 2019.

[61] Weihong Li, Li Yang, Jing Ren, and Hongde Jiang. Effect of thermal boundary conditions and thermal conductivity on conjugate heat transfer performance in pin fin arrays. *International Journal of Heat and Mass Transfer*, 95:579–592, 2016.

[62] Jackson Ball. Construction basics of shell and tube heat exchangers. https://www.process-heating.com/articles/86667-construction-basics-of-shell-and-tube-heat-exchangers, 2000.

[63] Arthur P Fraas. *Heat exchanger design*. John Wiley & Sons, 1991.

[64] Seyed A Niknam, Mehdi Mortazavi, and Dongsheng Li. Additively manufactured heat exchangers: a review on opportunities and challenges. *The International Journal of Advanced Manufacturing Technology*, pages 1–18, 2020.

[65] William D Gerstler and Daniel Erno. Introduction of an additively manufactured multi-furcating heat exchanger. In *2017 16th IEEE Intersociety Conference on Thermal and Thermomechanical Phenomena in Electronic Systems (ITherm)*, pages 624–633. IEEE, 2017.

[66] John D Bernardin, Kyle Ferguson, David Sattler, and Seung-Jun Kim. The design, analysis, and fabrication of an additively manufactured twisted tube heat exchanger. In *Heat Transfer Summer Conference*, volume 57892, page V002T10A002. American Society of Mechanical Engineers, 2017.

[67] Munson Okiishi Huebsch Rothmayer. Fundamentals of fluid mechanics 7th ed. munson.

[68] Weihong Li, Guopeng Yu, and Zhibin Yu. Bioinspired heat exchangers based on triply periodic minimal surfaces for supercritical co2 cycles. *Applied Thermal Engineering*, 179:115686, 2020.

[69] Eric A Lord and Alan L Mackay. Periodic minimal surfaces of cubic symmetry. *Current Science*, pages 346–362, 2003.

[70] Joshua M Kapfer, Rori A Paloski, et al. On the threat to snakes of mesh deployed for erosion control and wildlife exclusion. *Herpetological Conservation and Biology*, 6(1):1–9, 2011.

[71] P Zeynep Çulfaz, Steffen Buetehorn, Lavinia Utiu, Markus Kueppers, Bernhard Bluemich, Thomas Melin, Matthias Wessling, and Rob GH Lammertink. Fouling behavior of microstructured hollow fiber membranes in dead-end filtrations: critical flux determination and nmr imaging of particle deposition. *Langmuir*, 27(5):1643–1652, 2011.

[72] Victor Blakemore Slaughter. Method of using minimal surfaces and minimal skeletons to make heat exchanger components, January 11 2011. US Patent 7,866,377.

[73] Gokul Chandrasekaran. *3D Printed Heat Exchangers: An Experimental Study*. PhD thesis, Arizona State University, 2018.

[74] Reza Attarzadeh, Marc Rovira, and Christophe Duwig. Design analysis of the" schwartz d" based heat exchanger: A numerical study. *International Journal of Heat and Mass Transfer*, 177:121415, 2021.

[75] S Catchpole-Smith, RRJ Sélo, AW Davis, IA Ashcroft, CJ Tuck, and A Clare. Thermal conductivity of tpms lattice structures manufactured via laser powder bed fusion. *Additive Manufacturing*, 30:100846, 2019.

[76] Oraib Al-Ketan, Dong-Wook Lee, Reza Rowshan, and Rashid K Abu Al-Rub.

Functionally graded and multi-morphology sheet tpms lattices: Design, manufacturing, and mechanical properties. *Journal of the mechanical behavior of biomedical materials*, 102:103520, 2020.

[77] Oraib Al-Ketan, Mohamed Ali, Mohamad Khalil, Reza Rowshan, Kamran A Khan, and Rashid K Abu Al-Rub. Forced convection computational fluid dynamics analysis of architected and three-dimensional printable heat sinks based on triply periodic minimal surfaces. *Journal of Thermal Science and Engineering Applications*, 13(2):021010, 2021.

[78] Bahman Zohuri. *Compact heat exchangers*. Springer, 2017.

[79] Oraib Al-Ketan, Reza Rowshan, and Rashid K Abu Al-Rub. Topology-mechanical property relationship of 3d printed strut, skeletal, and sheet based periodic metallic cellular materials. *Additive Manufacturing*, 19:167–183, 2018.

[80] nTopology. Generative design with complete control. `https://ntopology.com/generative-design-guide/`.

[81] MA Balbaa, A Ghasemi, E Fereiduni, MA Elbestawi, SD Jadhav, and J-P Kruth. Role of powder particle size on laser powder bed fusion processability of alsi10mg alloy. *Additive Manufacturing*, 37:101630, 2021.

[82] Renishaw, meander stripe and chessboard hatchings pattern. `https://resources.renishaw.com/en/details/--95492`.

[83] J Pakkanen. Designing for additive manufacturing-product and process driven design for metals and polymers. *Politecnico di Torino*, 2018.

[84] Richard RJ Sélo, Sam Catchpole-Smith, Ian Maskery, Ian Ashcroft, and Christopher Tuck. On the thermal conductivity of alsi10mg and lattice structures made by laser powder bed fusion. *Additive Manufacturing*, 34:101214, 2020.

[85] Additive manufacturing with pure copper. `https://www.amchronicle.com/insights/additive-manufacturing-with-pure-copper/`.